PEOPLE'S DEMOCRATIC REPUBLIC OF ALGERIA

وزارة التعليم العالي والبحث العلمي

MINISTRY OF HIGHER EDUCATION AND SCIENTIFIC RESEARCH

جامعة سعد دحلب البليدة1

UNIVERSITY OF SAAD DAHLEB BLIDA 1

كلية العلوم

Faculty of Sciences

دائرة الفيزياء

Department of Physics

MASTER DIPLOMA THESIS
In Physics
Option: Nanophysics

THEME

Elaboration and characterization of nanostructured copper disulfide (CuS$_2$) thin films for energy conversion

Presented by:

Ms. Nabila HALIMI

Defended on 09/07/2023 in front of the jury composed of:

Dr. A. HASSEIN-BEY	MCB	USDB-1	President
Dr. A. YOUNES	MRA	CRTI	Examiner
Dr. N. OUARAB	MRA	CRTSE	Supervisor
Dr. S. BOUACHMA	MRB	CRTSE	Co-Supervisor

Blida 1-2022/2023

Acknowledgments

I begin by expressing my heartfelt gratitude to Allah, the guiding light in my life, for His unwavering support and blessings throughout the completion of this work. I am humbled and immensely grateful for the physical and moral strength bestowed upon me, allowing me to undertake and accomplish this modest project.

*I would like to express my sincere thanks to the thesis Director, **Dr. Nouredine OUARAB**, Senior Researcher A Class at CRTSE, for the help, support, advice, guidance, for the quality of the scientific and technical training he has provided to me during these months, which I reiterate my deep gratitude.*

I would also thank my thesis co-supervisor Dr. S. BOUACHMA, Senior Researcher B Class at CRTSE, for helping me to complete my work, for her advice and encouragement.

*I hold warmly to thank **Dr. Abdelkader HASSEIN-BEY**, to have accepted to chair the jury of this thesis.*

*I hold warmly to thank **Dr. Abderrahmane YOUNES**, to have accepted to examine my work to giving him more sense and perfection.*

*I hold highly to express my deep recognition and my gratitude to our Dean, our Head of nanophysics Department, and specially **Mr. Abdelkader HASSEIN-BEY**, and all professors of the physics department at the Saad Dahlab University, for all they have given me.*

I gratefully acknowledge to my families who always encouraged me to pursue my scientific way to this distant point and supporting me spiritually throughout this thesis as well as throughout my life so far in all its manifestations.

Finally yet importantly, I would like to thanks to all my colleagues at the Saad Dahlab University of Blida-1, all my friends and all the people who encouraged me during these years.

Dedications

I dedicate this thesis to:

My loving family especially to my parents, for their love, encouragement, endless sacrifices, and for being special parents, and making me a special person.

My brothers Walid, Sid Ali and Youcef.

My friends who make my life bright for their endless hours of fun, their love, support and devotion, especially Achouak and Fifi.

Abstract

Nanostructured copper disulfide (CuS$_2$) thin films have generated significant interest in energy conversion applications due to their unique properties. This study focuses on the fabrication and characterization of CuS$_2$ thin films using chemical bath deposition (CBD) and thermal evaporation techniques. XRD analysis confirmed the formation of CuS$_2$ by detecting the presence of Cu-S bonds. SEM imaging revealed an elongated cubic morphology in the films. Additional characterization techniques were employing to obtain a comprehensive overview of the properties relevant to this study. The findings provide valuable insights into the structure and morphology of CuS$_2$ thin films. This research contributes to the advancement of nanostructured materials for energy conversion and establishes a foundation for further investigations in this domain.

Résumé

Les films minces de disulfure de cuivre nanostructurés (CuS$_2$) ont suscité un intérêt significatif dans les applications de conversion d'énergie en raison de leurs propriétés uniques. Cette étude se concentre sur la fabrication et la caractérisation des films minces de CuS$_2$ en utilisant les techniques de dépôt par bain chimique (CBD) et d'évaporation thermique. L'analyse par diffraction des rayons X (DRX) a confirmé la formation de CuS$_2$ en détectant la présence de liaisons Cu-S. L'imagerie par microscopie électronique à balayage (MEB) a révélé une morphologie cubique allongée dans les films. Des techniques de caractérisation supplémentaires ont été utilisées pour obtenir un aperçu complet des propriétés pertinentes à cette étude. Les résultats fournissent des informations précieuses sur la structure et la morphologie des films minces de CuS$_2$. Cette recherche contribue à l'avancement des matériaux nanostructurés pour la conversion d'énergie et établit une base pour de futures investigations dans ce domaine.

ملخص

أثارت الأغشية الرقيقة ذات البنية النانوية لثاني كبريتيد النحاس (CuS$_2$) اهتمامًا كبيرًا بتطبيقات تحويل الطاقة نظرًا لخصائصها الفريدة. تركز هذه الدراسة على تصنيع وتوصيف أغشية CuS$_2$ الرقيقة باستخدام ترسيب الحمام الكيميائي (CBD) وتقنيات التبخير الحراري. كشف توصيف حيود الأشعة السينية تكوين CuS$_2$ من خلال الكشف عن وجود روابط Cu-S. كشف مسح المجهر الإلكتروني عن مورفولوجيا مكعبة ممدودة في الأغشية. تم استخدام تقنيات توصيف إضافية للحصول على نظرة عامة شاملة للخصائص ذات الصلة بهذه الدراسة. توفر النتائج رؤى قيمة حول بنية وتشكل أغشية CuS$_2$ الرقيقة. يساهم هذا البحث في تطوير المواد ذات البنية النانوية لتحويل الطاقة ويضع أساسًا لمزيد من التحقيقات في هذا المجال.

Contents

g

Nomenclature

AAS	Atomic Absorption Spectrometry
ALD	Atomic layer deposition
ASC	Asymmetric Supercapacitor
AFM	Atomic force microscopy
APCVD	Atmospheric Pressure CVD
CBD	Chemical bath deposition
CVD	Chemical vapor deposition
CDW	charge density wave
CBH	Correlated Barrier Hopping
DC	Direct Current
Ev	Electron volts
EDX	Energy dispersive X-ray spectroscopy
FTIR	Fourier transformation infrared
GC	Gas chromatography
GSC	Gas Solid chromatography
GLC	Gas Liquid chromatography
HF	Hydrofluoric acid
LPCVD	Low-pressure chemical vapor deposition
MOCVD	Metal-organic chemical vapor deposition
PVD	Physical vapor deposition
PLD	Pulse Laser Deposition
PL	Photoluminescence
PVDF	Polyvinylidene Fluoride
PECVD	Plasma Enhanced Chemical Vapor Deposition
RGO	reduced graphene oxide

RF	Radio Frequency
Ra	The average roughness
Rq	Root mean square roughness
SEM	Scanning electron microscopy
SC	Spin Coating
STM	Scanning tunneling microscopy
Sccm	Standard cubic centimetre per minute
TL	Thermoluminescence
TEM	Transmission electron microscopy
UV-Vis	Ultraviolet-Visible
VOCs	Volatile Organic Compounds
VHN	The Vickers hardness
XRD	X-ray diffraction
XPS	X-ray photoelectron spectroscopy
XRF	X-ray fluorescence

List of figures

Chapter 1:

Chapter 2:

Chapter 3:

List of tables

General Introduction:

Air pollution is a major threat to public health worldwide, due to its prevalence and emissions from a variety of sources. Among these sources are industrial activities, mining, the transport sector and human activities in general. Certain other volatile organic compounds (VOCs), from farmers or poultry farming, are a major problem because of their toxicity, even at low concentrations. In addition, VOCs, as well as inorganic oxides, can been transported over long distances and produce secondary air pollutants, and may be responsible for acid rain and global warming [1, 2]. Against this backdrop, there is a strong demand for an effective, low-cost and environmentally friendly technology that can implement for air purification, even at low levels of pollutant concentration. The application of sunlight-induced photo catalysis could be one of the technologies to solve these problems [2]. Heterogeneous photo catalysis using nano semiconductors is an efficient method that facilitates air pollutant degradation, bacterial inactivation, hydrogen production and photo concentration.

For this issue, a gas separation filter, which is a screen between two adjacent thin layers acting as a selective barrier for molecules according to their size, shape and/or chemical properties? The membrane acts as a barrier that lets certain gas molecules through and blocks others, depending on their material affinity and the driving force behind the molecules mobility. The membrane market, now worth over $1.5 billion a year, began in 1979, when Permea, then a division of Monsanto, launched the very first membrane plant based on hollow polysulfide fibers to purge hydrogen in the Bosh-Haber process. This technology has extended to refining applications, such as the separation of nitrogen and light hydrocarbons, and to syngas applications for H_2/CO [3].

Membrane gas separation at high temperatures and in the presence of aggressive species such as H_2S, NH_3, SO_X and above all NO_X, is becoming increasingly important and will be a relevant area of research in the future. In this respect, the incorporation of copper sulfide nanoparticles, into the structure of certain types of ceramics, improves their properties, which is particularly useful for performance under such harsh conditions [3]. Copper sulfide, as a member of the chalcogenide nano crystallized semiconductor, is a significant element with multifunctional utilization in industry through the solar cells, optical filters, sensors, photo catalysts, and lithium ion batteries, and other devices are inexpensive due to

the high absorption coefficient (10^4 cm^{-1}) and small band gap [4]. Depending on various growth conditions such as molar concentration, temperature, capping agents, surfactants, and precursor solution composition, nanostructured copper sulfide exhibits intriguing structural and optical properties. It occurred that in the 3^d series as the known mineral or synthetic compounds MnS_2 (hauerite), $MnSe_2$, $MnTe_2$, FeS_2 (pyrite), CoS_2, $CoSe_2$, NiS_2, and $NiSe_2$. The use of high-pressure syntheses to extend this range to include the compounds CuS_2, $CuSe_2$, $CuTe_2$, $NiTe_2$, $CoTe_2$, $FeSe_2$, and $FeTe_2$ has been reported [5-6].

Recent advances in gas separation technology have been highlighted by the development of increasingly sophisticated new techniques and the availability of correlations between properties and structure. Permeability is a property of the material on which the membrane has been manufactured, so modifications to its structure always produce changes linked mainly to the size and shape of its pores, as well as to the chemical nature of the material used. Selectivity, on the other hand, is influenced by factors such as operating pressure and temperature, the composition of the feed mixture and the presence of impurities. As a result, while permeability provides good performance, it needs to be optimized by careful material selection and catalyst design. Nevertheless, permeability and selectivity are essential parameters in determining the overall efficiency of a dense filter for various industrial and environmental applications [3].

In this work, we will be elaborating thin layers based on copper sulfide and then analyzing them using structural, such as X-ray diffraction (XRD), morphological (SEM, AFM), photoluminescence, and photo-electrochemical characterization techniques, chemical composition, and spectrophotometer spectroscopy.

This thesis is dividing into three chapters with a general conclusion. The first chapter provides a general overview of all possible properties of the CuS_2 such as structural, morphology, chemical composition and optical. The second chapter focuses on the various thin layer deposition techniques employed for synthesizing the substrate, accompanied by an in-depth examination of the characterization procedures; and in the third chapter, presents the characterization results obtained and discusses the observations and findings of this material study.

Finally, a general conclusion summarizes the main results obtained and future perspectives.

Chapter 1

Bibliographic synthesis

1. **Introduction:**

In this chapter, we present the general overview of copper sulfide-based thin films, followed by a discussion of their structure, morphology and various properties.

2. **Copper sulfide CuS$_2$:**

2.1. **Introduction**

Copper sulfide is one of the chalcogenide semiconductors and is an important element with multifunctional uses in industry through solar cells, optical filters, sensors, photo catalysts, lithium ion batteries, and other devices. Nanoscale transition metal sulfides, such as PbS, HgS, CdS and CuS, exhibit remarkable chemical and physical properties compared to their bulk state [4]. While the 3d transition-metal dichalcogenides MX$_2$, those with M = Fe, Co, Ni, Cu, and Zn, and X = S and Se, are known to crystallize in the so-called pyrite structure. It is contains interpenetrating face-centered-cubic arrays of metal cations and anion dimers, as in the rock salt structure, see Fig.1.1. Each cation is in the center of an anion octahedron, and each anion atom has a tetrahedral coordination consisting of one anion atom and three cations. Because of the strong p-p hybridization within the chalcogen anion dimer, each anion dimer can accommodate two electrons in its bonding pσ orbital but not in the antibonding pσ* orbital, serving as divalent X_2^{2-} in a native ionic picture. Transition-metal cations, therefore, are formally divalent, M^{2+}, and take a low spin electronic configuration tg_2^6 , eg_2^4 [5].
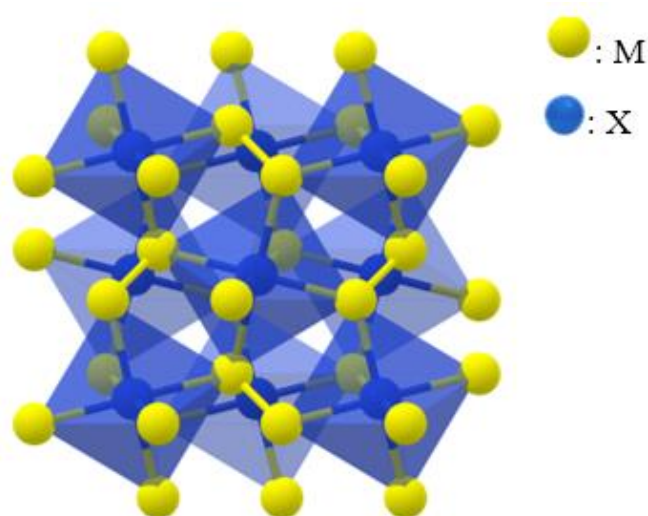
Fig.1.1. Crystal structure of pyrite MX$_2$ (M: transition-metal elements; X: chalcogen elements). [5]

Depending on that question, the electronic and magnetic properties of transition metal pyrite dichalcogenides have been attracting considerable interest for many decades. CuS_2, which was supposed to have three eg electrons, was reported to be a p-type semi-conductor [5-6]. It consisting of copper cation Cu^{2+} and disulfide anion S^{2-}, which can be obtained by reacting copper sulfide CuS with elemental sulfur following the equation [7]:

$$CuS + S \rightarrow CuS_2 \hspace{6cm} 1.1$$

Thus, copper sulfide has been discovered since 1920, when the study of copper deposits at the Providencia mine in the municipality of Carmenes, León (Spain) [8]. Although its crystalline structure has only elucidated in the 20th century, it has a black color, and it is a water-insoluble solid used in a variety of industrial applications. However, it does not exist in nature, but it can be synthesized at high extreme conditions [9].

2.2. Structure of copper sulfide

CuS_2 has a cubic crystal structure that is of interest for two reasons. Firstly, its crystal chemistry has uniquely determined by X-ray diffraction. Secondly, optical evidence of non-cubic symmetry has been reported, but has not been explained in terms of crystal structure. However, ab-initio calculations of CuS_2's pyrite structure have considered it to belong to the non-symmorphic group. The crystal structure can be described by the space group of 205 $Pa\overline{3}$ and is designated by the notation Strukturbericht C2 with lattice parameters a=b=c= 5.7891Å [10].

Within a unit cell, the Cu^{2+} cations occupy the face centers of the cubic cell, while the S_2 dimers are centering near the anion positions, as shown in upper left panel of Fig.1.2. For the closest-packed (111) plane and as shown in right panel of Fig.1.2, the surface exhibits a hexagonal structure with an in-plane lattice constant of 8.19 Å for which each primitive unit cell (shown as a green rhombus) consists of four Cu^{2+} cations and four S_2^{2-} dimers. As schematically illustrated in bottom panel of Figure.1.2, along the (111) direction, three of the four S_2^{2-} dimers are tilted with respect to the (111) orientation, while the remaining S_2^{2-} dimer is along the (111) direction. Therefore, the eight S atoms, separated into four different planes, are sandwiched between the two adjacent Cu layers with a distance of 3.34 Å. That is, the pyrite CuS_2 forms a quasi-layered structure along the (111) direction. For

convenience, we hereafter introduce a reduced unit cell (including one Cu atom) marked by the red rhombus in upper right panel of the Figure.1.2 [09, 10].
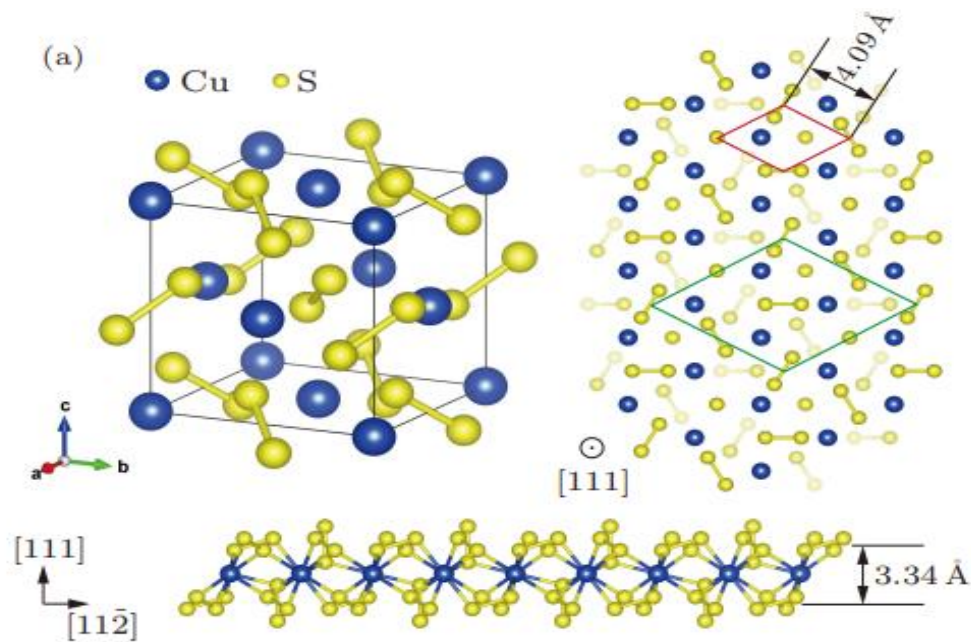
Fig.1.2. Crystal structure of pyrite CuS₂ [10]

In CuS_2, two types of coordination polyhedra are illustrating in Fig.1.3. Six sulfur atoms are forming a trigonally distorted octahedron, whereas one other sulfur atom and three copper atoms form distorted tetrahedron coordinate sulfur, encircle copper atom. The corner sharing of CuS octahedra is responsible for the linkage. Additionally, the sulfur-sulfur distance in pyrite structures is similar to that in sulfur dimer [09].
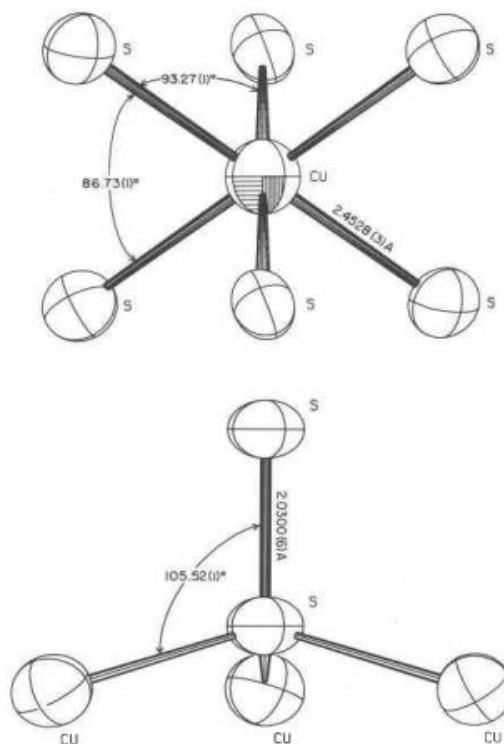
Fig.1.3. First coordination polyhedral for Cu and S in CuS$_2$ with the interatomic distances and angles calculated from the final model. [09]

Table 1 and Figure.1.4 illustrate some significant interatomic distances and angles for the pyrite structures of first-row transition elements. The CuS$_2$ parameters follow the trends established by the pyrite structures found in nature, indicating that copper has the same oxidation state (2+) as the other metals in this group. Consequently, the discussions regarding bonding in these materials (Bither et al., 1968[6]; Brostigen and Kjekshus, 1970[15]; Goodenough, 1972[16]) are also applicable to CuS$_2$. These models purpose that the increase in metal-sulfur bond length, as shown in Fig.1.4, is due to an increase in the number of antibonding electrons, three of them share to copper in CuS$_2$. (Additionally, Kjekshus and Nicholson, 1971[17]) suggest that these electrons cause a redistribution of electron density, leading to a decrease in the sulfur-sulfur bond length (as shown in Figure.1.4) [09].

Table 1. Selected interatomic distances, interatomic angles, and quadratic elongations for several transition element disulfides in the pyrite structure are presented [09].

	MnS	FeS_2^b	CoS_2^a	NiS_2^c	CuS_2^d
M-S, A	2.590	2.259(5)	2.315	2.401(4)	2.4528(1)
S-S, A	2.086	2.153(6)	2.124	2.059(32)	2.0300(6)
S-S-M, deg	106.1	102.4(2)	103.3	104.8(4)	105.52(2)
S-M-S, deg	86.9	85.66(9)	86.0	86.5(1)	86.73(1)
MS_6 Quadratic Elongation	1.0030	1.0061	1.0052	1.0039	1.003

[a]Elliott(1960). [13]
[b]Finklea et al. (1976). [13_1]
One standard deviation in parentheses. [09]

[c]Putuseth and kjekshus(1969). [14]
[d]Husnnt ,King and Prewit.(1979) [09]
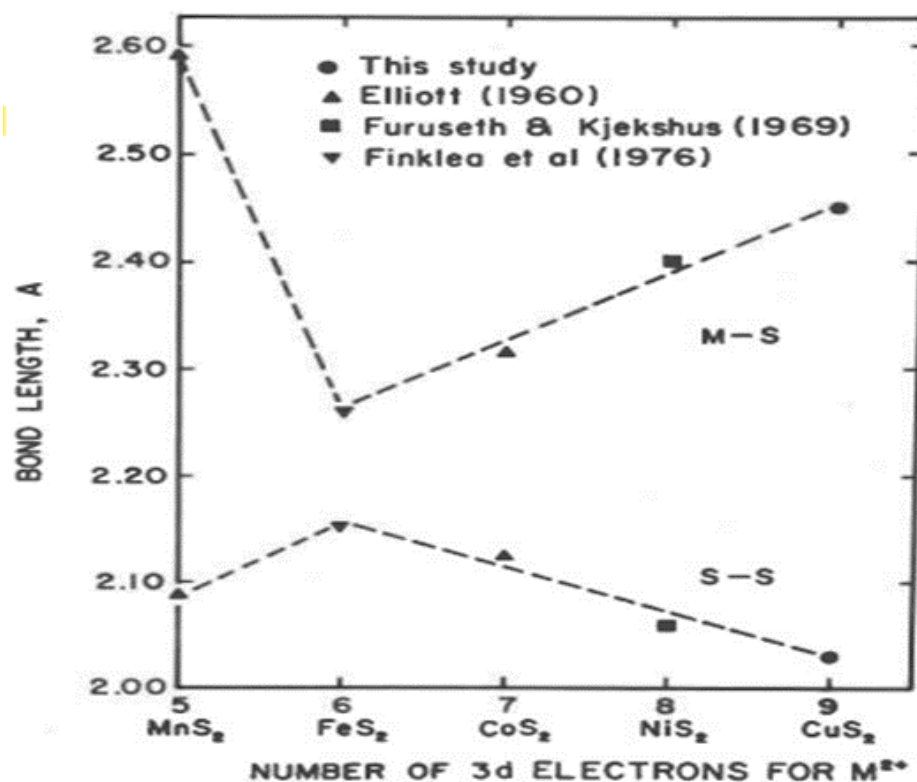
Fig.1.4. Bond Jength variation for fint-row transition-element disulfide pyrite structures including the CuS_2 results. [09]

2.3. Morphology

Based on morphology, nanostructured materials can be classified into different types according to their dimensions. There are zero-dimensional (0D), one-dimensional (1D), two-dimensional (2D) and three-dimensional (3D) nanomaterials. Zero-dimensional materials consist of isolated nanoparticles, while one-dimensional materials are nanofibers or nanotubes. Two-dimensional materials are thin films or coatings in the nanometer range. In these materials, the structural elements can be dispersed in a matrix or applied to a substrate. Three-dimensional nanomaterials include powders, fibrous structures, multilayers and polycrystalline materials. They made up of tightly packed structural elements forming interfaces. Compact or consolidated (bulk) polycrystals with nanometric grains represent an important type of three-dimensional nanostructured materials. In these materials, the entire volume is filled with nano-sized grains, and the surface area of individual grains is negligible. This distinguishes them from agglomerated nanocrystalline powders, in which particles of the same size make up the material. There are some illustrations shown in Figure 1.5[18-20].

| Clusters | Nanotubes, fibers and rods | Films and coats | Polycrystals |
| 0D | 1D | 2D | 3D |
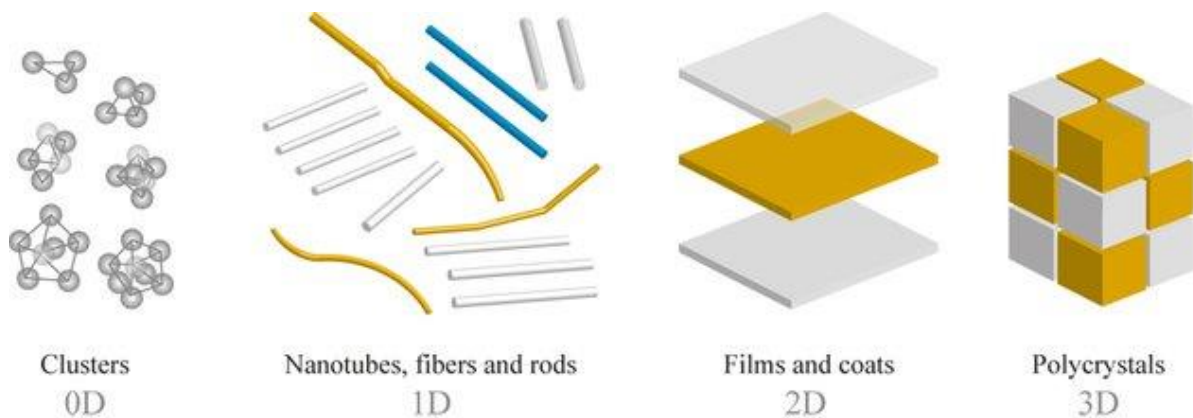
Fig.1.5.Types of nanocrystalline materials by size of their structural elements: 0D (zero-dimensional) clusters; 1D (one-dimensional) nanotubes, fibers and rods; 2D (two-dimensional) films and coats; 3D (three-dimensional) polycrystals.

Therefore, we can say that the morphology of CuS_2 can depend on the method of synthesis, temperature, pressure, and other factors. Generally, CuS_2 can exist in different forms including crystals, powders, and thin films.

Taking TEM images of CuS_2 nanoparticles synthesized at 220°C and 180°C as an example, the particles are ranging in size from 31.28 to 43.98 nm, as shown in

Fig.1.6. Nanoparticles are semi-spherical in shape and increase in size with temperature [21].
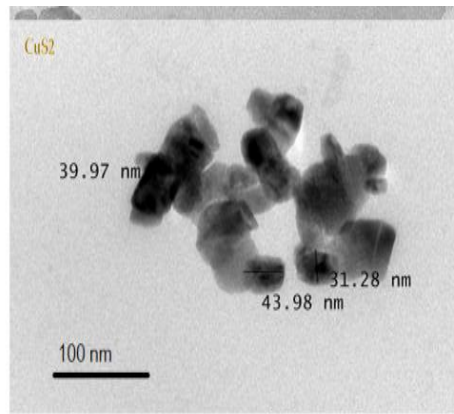
Fig.1.6.TEM images of CuS$_2$ nanoparticles. [21]

Figure.1.7. shows the SEM micrographs and EDX chemical analysis of copper sulfides nanoparticles. They displayed different morphologies at different temperatures. The EDX spectra confirmed the presence of copper and sulfur in the particles. Carbon and oxygen peaks are present in analyzed spectra due to the capping agent used for nanoparticles preparation [21]. Series of typical topographic STM images of CuS$_2$ at different coverages are showing in Fig.1.8, however, the topographic image of 1 ML of CuS$_2$ after annealing at 200°C is shown in Fig.1.9. Thus, to further modulate and explore the properties of CuS$_2$ films at the 2D limit, in-situ post-annealing is performing of the as-grown 1 ML CuS$_2$ films, as shown in figures1.7-9 [10].
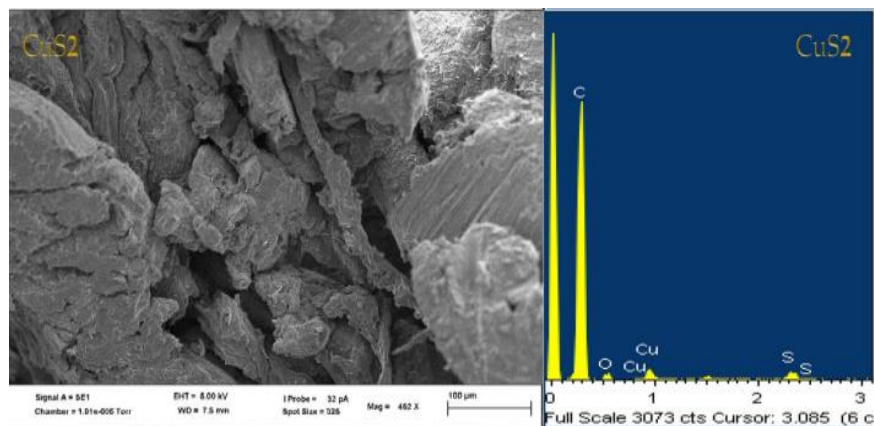
Fig.1.7.SEM micrographs and EDX spectra of CuS$_2$ nanoparticles. [16]
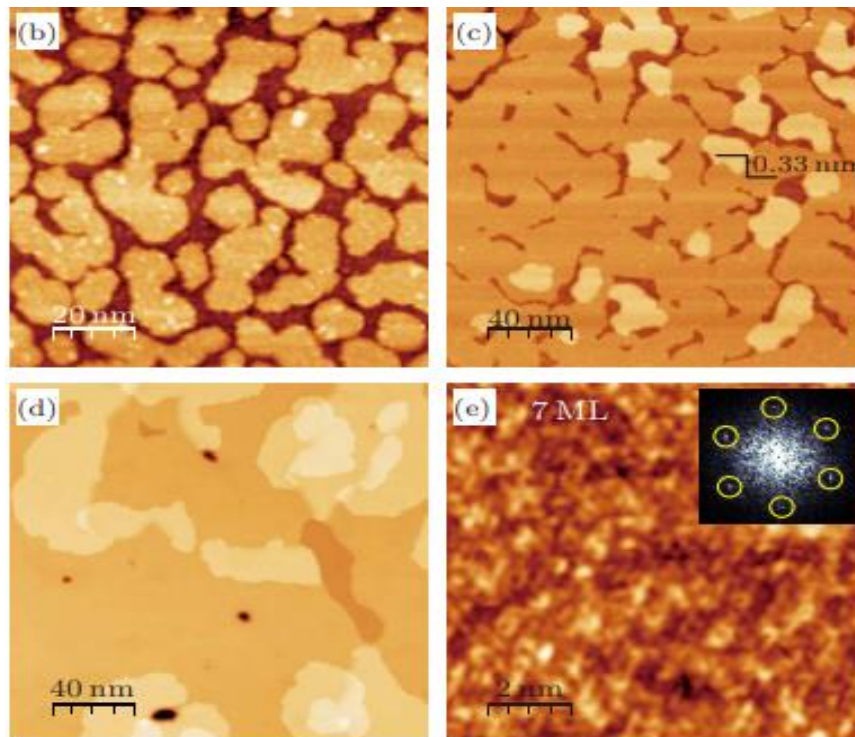
Fig.1.8. (b)–(e) STM topographic images of CuS$_2$ at various nominal coverages: (b) 0.7 ML (Vs = 5 V, I = 50 pA), (c) 1 ML (Vs = 4.5 V, I = 40 pA), and (d)–(e) 7 ML ((d) Vs = 6 V, I = 50 pA and (e) Vs = 0.4 V, I = 100 pA). The inset in (e) is the corresponding FFT images with the yellow circles marking the 1×1 Bragg points. [10]
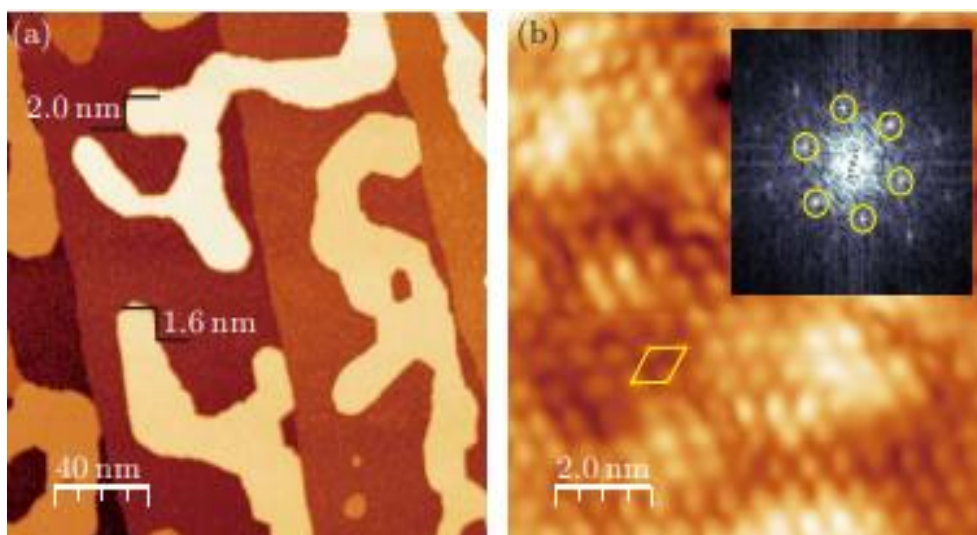
Fig.1.9. (a)– (b) Topographic image of 1 ML CuS$_2$ after being annealed at 200∘C ((a) Vs = 2.5 V, I = 50 pA; (b) Vs = 1.3 V, I = 200 pA). In (b), the yellow rhombus labels the unit cell. The inset is the corresponding FFT images showing reconstruction, as labelled by the yellow circles. [10]

2.4. Physical Copper disulfide properties

2.4.1. Introduction

Copper disulfide CuS_2 is a semiconductor material with intriguing physical properties. Its cleavage described as pseudocubic, meaning that it breaks into two new cells. The cleavage refers to how a crystal breaks when subjected to stress. In contrast, the crystal breaks irregularly and non-uniformly when not subjected to stress. Its hardness measured at 4.5 on the VHN scale, with a range of 535-710 for spherical aggregates and 440-520 for euhedral crystals under a 20g load. The measured density is 4.4-4.5, while the calculated density ranges from 4.41 to 4.61[22].

2.4.2. Electronic properties

Extensive experimental and theoretical studies carried out on the fundamental electronic structure of pyrite. It establishes that pyrite layers contain various elements in varying concentrations, which can potentially influence the electronic properties of the films [23]. Among them, CuS_2 can be synthesized at very high pressures [24], having a direct band gap [25], a high absorption coefficient ($10^5 cm^{-1}$) within a superconducting performances [6, 26].

All electronic properties of CuS_2, in cubic phases at equilibrium lattice parameters such as density of states and energy bands, have been calculated. Therefore, Figure.1.10 shows the electronic band structure of the CuS_2 along the high-symmetry points of the Brillouin zone [27].
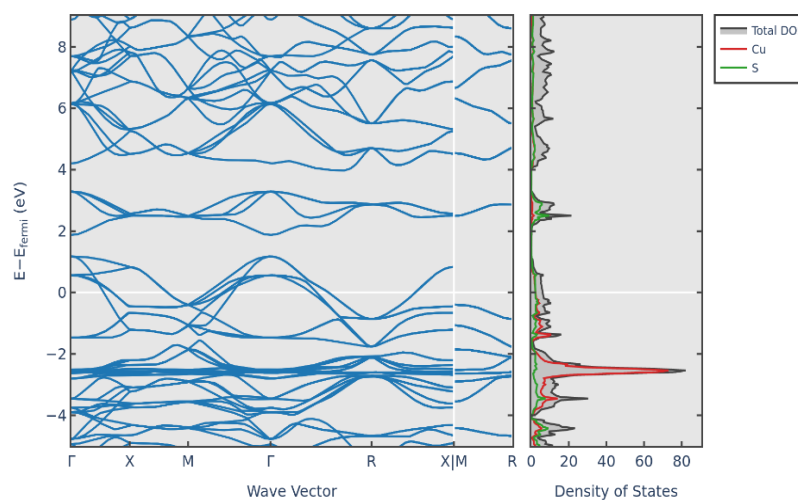
Fig.1.10. Band structure of CuS_2 along symmetry direction in Cubic phase. [28]

Many studies reveal that the energy levels of 3d metal orbitals have an effect on the electronic properties of different metal disulfides.This effect is significant in

CuS_2. Specifically, the energy of the 3d metal orbitals is lower than that of the π^* orbital. As a result, the filled bonding band (e.g. π^*) is now predominantly composed of metal bands, while the partially filled non-bonding band has a predominant anionic character. This implies that Cu currently has a d^{10} configuration, while the Fermi level is in an anionic band. The asymmetry of the S_{2p} signal confirms this, and the XPS Cu_{2p} signals show only a rudimentary satellite and slight asymmetry, indicating that the anti-bonding band (π^*, eg) still exhibits 3d metal character, but not much. As a result, the oxidation state of Cu in CuS_2 is +1, while the oxidation state of the S2 anion is -1. [29]

We can take the figure 1.13 as an example of the electronic band because of the common electronic properties between CuS_2 and FeS_2 arise from their similarities in crystal structures and overall chemical composition. Both compounds contain sulfur (S) and share some fundamental electronic characteristics. The electronic band characteristics depend on the interactions of sulfur and copper and the formation of chemical bonds within the crystal structure. [30]
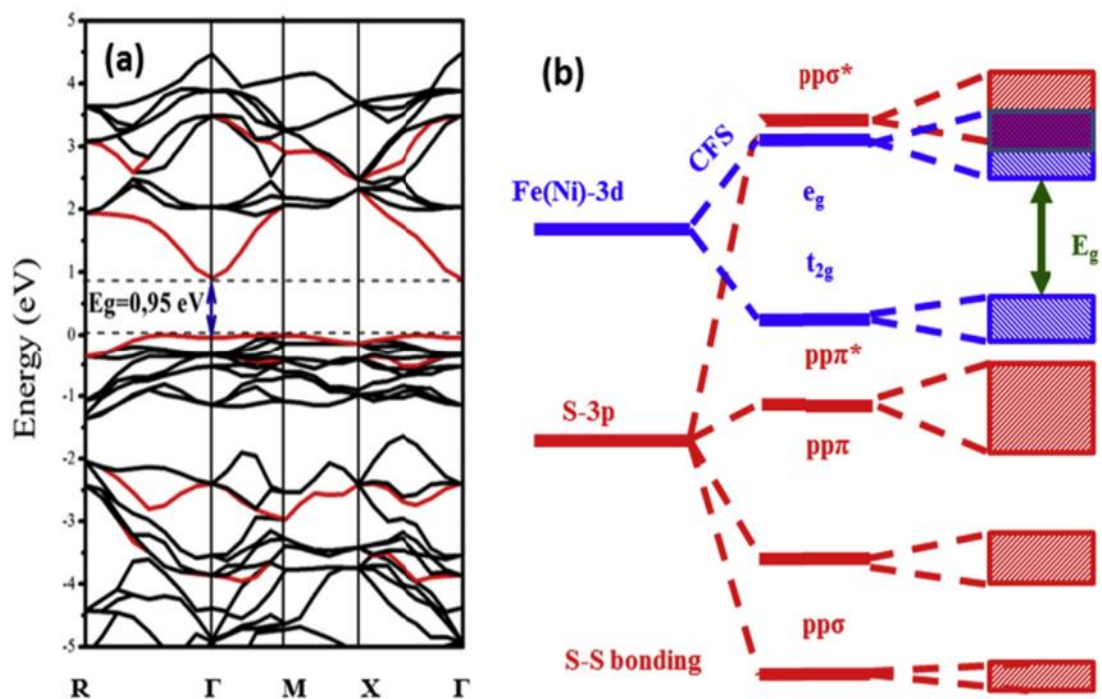
Fig.1.13. Band structure of FeS_2 pyrite obtained [30].

2.4.3. <u>Magnetic properties</u>

CuS_2 is a metal compound, has been reported to have a wide range of magnetic properties. Recent studies have shown that it exhibits periodic modulation of the charge density wave (CDW) structure, manifested by distortion of the lattice parameter. The electron-phonon coupling induces CDW structure, with changes in electron temperature activating phonon modes that promote lattice distortion. The transition between high- and low-symmetry structures in CuS_2 and the absence of CDW in its monolayer form make it an ideal system, which let to study the interplay between CDW and superconductivity. Further researches are needed to explore the dynamic stability of CuS_2 and to better understand its properties with potential applications [31-33].

According to the studies, the bulk susceptibility of CuS_2 gradually decreases below $T_Q = 160K$, as shown in Fig.1.14. Consequently, the Cu^{63} spectra linewidth significantly increases below T_Q (figure 1.14), and the copper quadrupolar spectrum is no longer distinguished, see Fig.1.15. Additionally, the curve of lattice parameter against temperature (figure.1.16) demonstrates a change in $\Delta a/\Delta T$ near T_Q. Other measurements of electrical resistivity are also sensitive to this second-order transition and agree with the previous study conducted by Bither et al. (1968) [6], indicating a change in $\Delta\rho/\Delta T$ for $T \sim T_Q$. Moreover, a first-order transition occurs close to $T_R = 47K$, characterized by a sharp jump of the lattice parameter (figure1.16) with Δa ($T= T_R$) = 0.0012Å and a peak in the magnetic susceptibility, see Fig.1.16 [31].
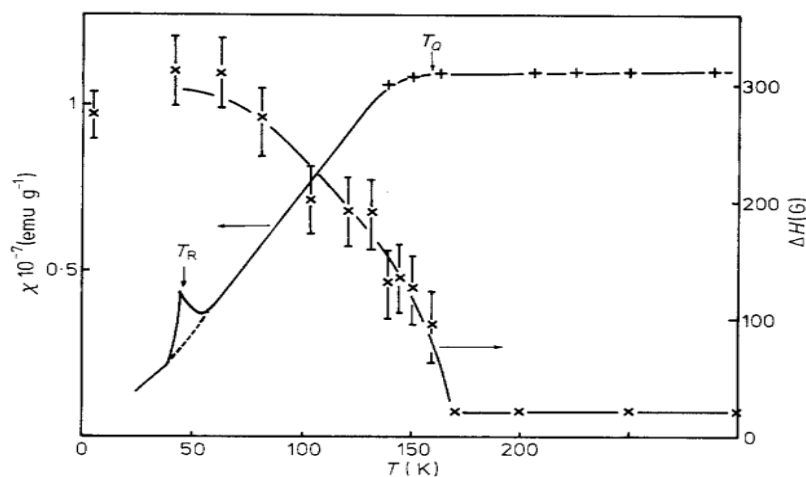
Fig.1.14. Temperature dependence of the bulk susceptibility (+) and ^{63}Cu NMR linewidth (x) in CuS_2. [31]
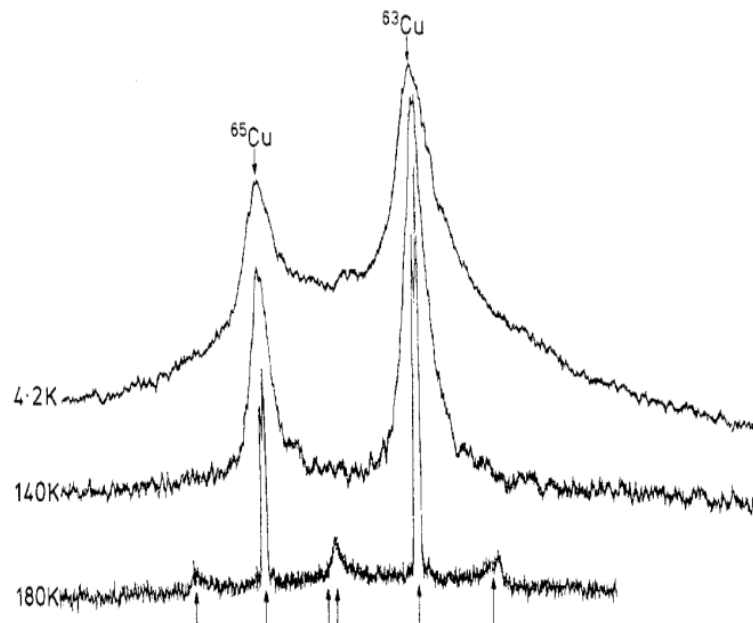
Fig.1.15. NMR spectra for copper in CuS$_2$, at various temperatures.
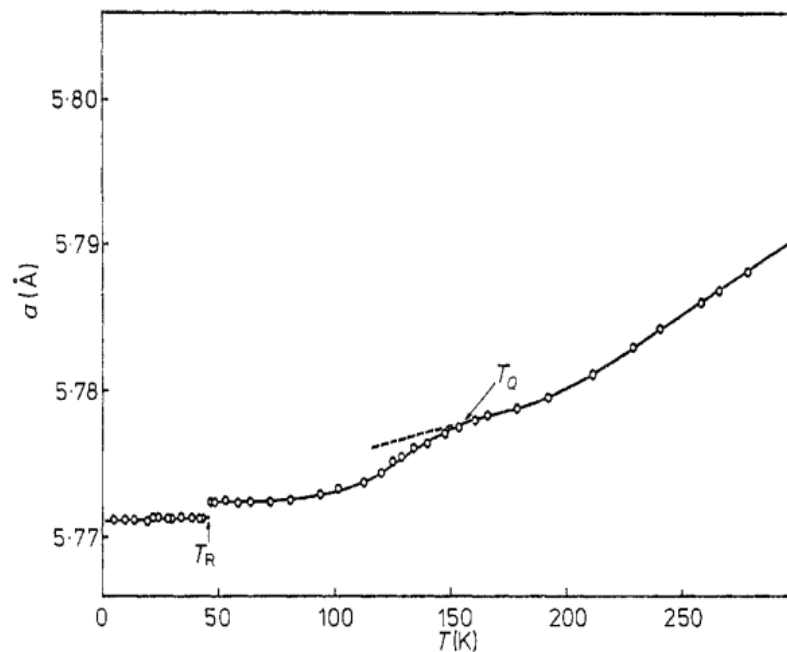
Fig.1.16. Temperature dependence of the lattice parameter in CuS$_2$, Δa (T= T$_R$) = 0.0012A. [31]

2.4.4. <u>Optical properties:</u>

The synthesis and study of the optical properties of nanomaterials, in particular metal chalcogenides, have received considerable attention in recent

15

decades due to the quantum confinement effects associated with their small crystallite size, which confer new properties and make them useful in light-emitting diodes [34]. CuS_2 has unique optical properties characterized by its opaque, iron-black color, with a pale blue-gray to violet-gray in reflected light. Its appearance is sooty black with a dull metallic sheen. CuS_2 has a relatively high reflectance, with R-values ranging from 30.1 at 400 nm to 30.1 at 700 nm. At shorter wavelengths, reflectance decreases, reaching a minimum of 25.9 at 580 nm, before increasing again towards longer wavelengths [23].

2.4.5. <u>Electrical properties:</u>

The electrical properties of CuS_2 films are demonstrating by an electroless deposition method and subsequent iodination to form highly transparent and conductive CuI films. The electrical conductivity of CuS_2 is enhanced by the introduction of iodine atoms, which act as donors, and by promoting carrier concentration. The electrical properties of the films were characterized by current-voltage measurements I(V), which showed a linear relationship between current and voltage, indicating ohmic behavior. The resistivity of the films is estimated to be at around 2×10^5 Ω cm, which corresponds to the range of semiconductor materials. The films also exhibit high optical transmittance in the visible range, making them suitable for transparent conductive applications such as touch screens, solar cells and displays. Overall, the iodination process, which gives a highly conductive and transparent CuI films, is suitable for practical applications [35] and has improved the electrical properties of CuS_2 films.

Furthermore, the conductance of CuS_2 follows Jonscher's universal power law, which describes the frequency-dependent conductivity of disordered systems. The exponent "s" in this power law decreases with increases of the temperature, indicating that the conduction phenomena in CuS_2 are linked to Correlated Barrier Hopping (CBH), as shown in Fig.1.17 [35].
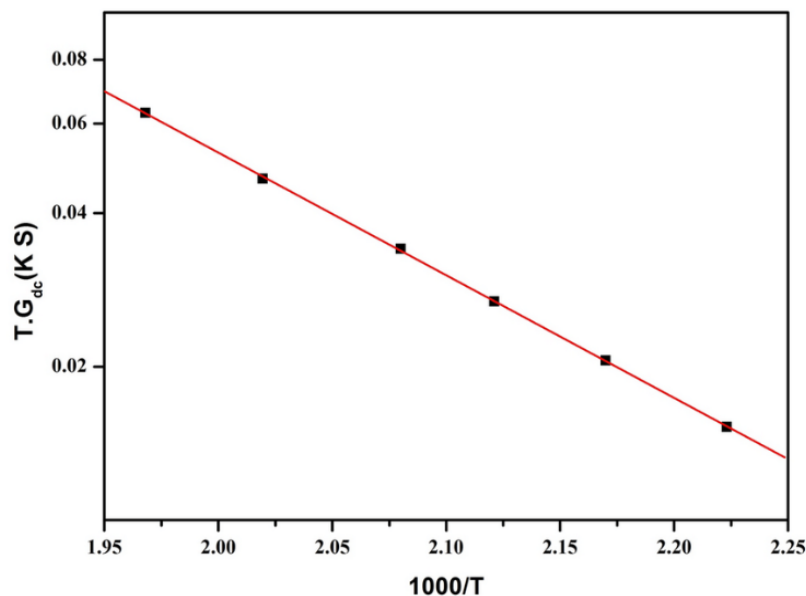
Fig.1.17.Plot of exponent's' versus temperature of CuS$_2$ film. [35]

2.4.6. photoconductive properties

Photoconductivity refers to the ability of a material to conduct an electric current when exposed to light. In the case of CuS$_2$, photoconductivity studies have shown that photocurrent as a function of light intensity follows a power law, while polarization follows a linear trend. This suggests that the material is capable of generating photocurrent in response to incident light, and that the direction of the current depends on the polarization of the light [36].

Furthermore, the prepared CuS$_2$ film exhibits excellent stability and its alternating current conductivity (Gac) reveals semiconductor behavior with estimated activation energy of 0.5 eV. It shown that the conduction phenomenon in CuS$_2$ is related to Correlated Barrier Hopping (CBH), which is a hopping mechanism of electrons movement in correlation in the material. The high absorbance of CuS$_2$ in the UV range, as shown by UV absorbance and reflectance spectra, with a gap energy of 1.87 eV estimated by the Tauc model, makes it a promising material for optoelectronic applications such as solar cells and photodetectors. Overall, the photoconductive properties of CuS$_2$ make it a promising candidate for optoelectronic devices [36].

The photoconductive properties of the films depend on the intensity of the incident light, and the films show a good response to visible light. AS shown in

17

Fig.1.18, the photocurrent increases linearly with increasing light intensity, indicating a linear relationship between photocurrent and light intensity.
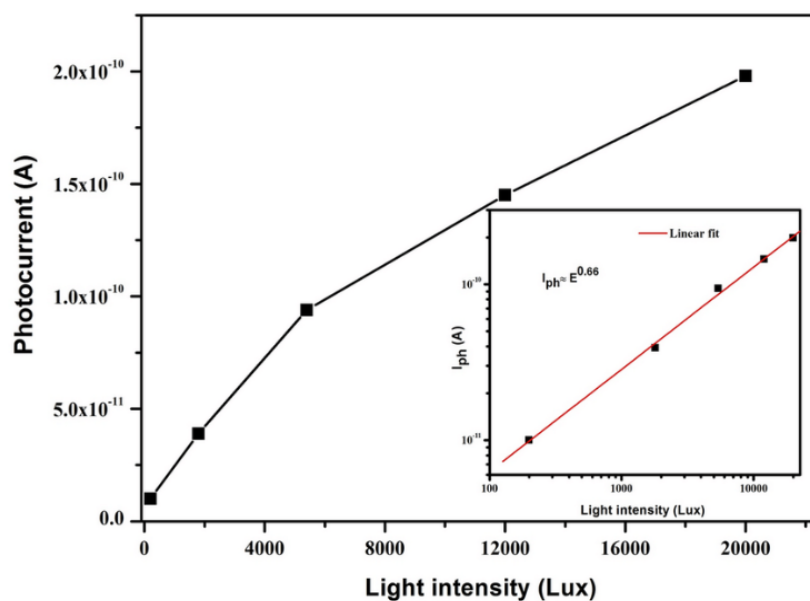
Fig.1.18.Variation of photocurrent versus light intensity. [36]

2.4.7. Electrochemical properties

For over fifty years, electrochemical mechanisms have been employed to explain certain phenomena observed in flotation processes. It has been determined that the absorption of collectors onto sulfide minerals takes place through an electrochemical mechanism [37].

The electrochemical properties of CuS_2 were studied using galvanostat and XPS (X-ray photoelectron spectroscopy) techniques. The dissolution/passivation products formed during electrochemical oxidation of chalcopyrite in 1 mol/L perchloric acid were identified as Fe^{2+} and metastable CuS_2 at lower potentials (~0.74 V) and elemental sulfur at higher potentials (> 1.24 V) [07].

CuS_2 has been observed to have a monovalent (d^{10}) oxidation state of copper, which is different from its expected divalent (d^9) oxidation state. The formation of a passive film according to the anodic reaction:

$$(Cu^+)(Fe^{3+})(S_2^{2-}) = CuS_2 + Fe^{2+} + 2e^- \tag{1.2}$$

Can be considered, with a possible change in oxidation states (Cu^+) (S^{2-}) proposed by Yin et al. (1995) [39]. Another possibility for the formation of CuS_2 is through redox or precipitation reactions to produce CuS_2 on the surface from ions in solution.

$$Cu^{2+} + S_2^{2-} = Cu^+ + S^{2-} \tag{1.3}$$

Where the disulfide S_2^{2-} can be formed by the oxidation of H_2S formed by non-oxidative dissolution.

$$2H_2S = 4H^+ + S_2^{2-} + 2e^- \tag{1.4}$$

Overall, we can say that the electrochemical properties of CuS_2 are related to its oxidation states and its ability to form passive films or undergo redox/precipitation reactions under certain conditions [07].

In other hand, the electrochemical properties of Ni_3S_4/CuS_2 were studied in a 2M KOH solution using a CHI660D (Chenhua, shanghai, China) which is a electrochemical reactor. The working electrode was made of Ni foam coated with a mixture of active materials, acetylene black and Polyvinylidene Fluoride (PVDF). The specific capacitance of the electrode is calculating by the Eq.1.5 [40].

$$C = \frac{I \times \Delta t}{m \times \Delta V} \tag{1.5}$$

Where I is the charge and discharge current, Δt is the discharge time, m is the mass of the active electrode material, and ΔV is the potential window. The Ni_3S_4/CuS_2 material is used as the positive electrode in an asymmetric supercapacitor (ASC), while reduced graphene oxide (RGO) is used as the negative electrode. The specific capacitance of the RGO is 48.8 Fg^{-1} at 1 Ag^{-1} according to equation (1) in the three-electrode system.

The optimal weight ratio of the two electrodes was determined using the Eq.1.6

$$\frac{m^+}{m^-} = \frac{C^- \times \Delta V^-}{C^+ \times \Delta V^+} \tag{1.6}$$

Where m^+ is the mass, ΔV^+ presents the potential window, and C^+ presents the specific capacity of the positive electrode, respectively; and m^-, ΔV^-, and C^- are the corresponding negative one, respectively.

The energy density (E, Whkg^{-1}) and power density (P, Wkg^{-1}) of the ASC are calculating by the Eq.1.7-8.

$$E = \frac{Ct \times \Delta V^2}{7.2} \tag{1.7}$$

$$P = \frac{3600 \times E}{\Delta t} \tag{1.8}$$

Where Ct (fg^{-1}) is the specific capacitance of the ASC, ΔV (V) is the voltage window, and Δt(s) is the discharge time [40].

The study showed that the obtained nanocomposite exhibits excellent electrochemical performance, with a specific capacitance of 888 Fg^{-1} at 1 Ag^{-1} and high cycling stability of 83.33% retention after 2000 cycles in a three-electrode system, as shown in Fig.1.19-20.
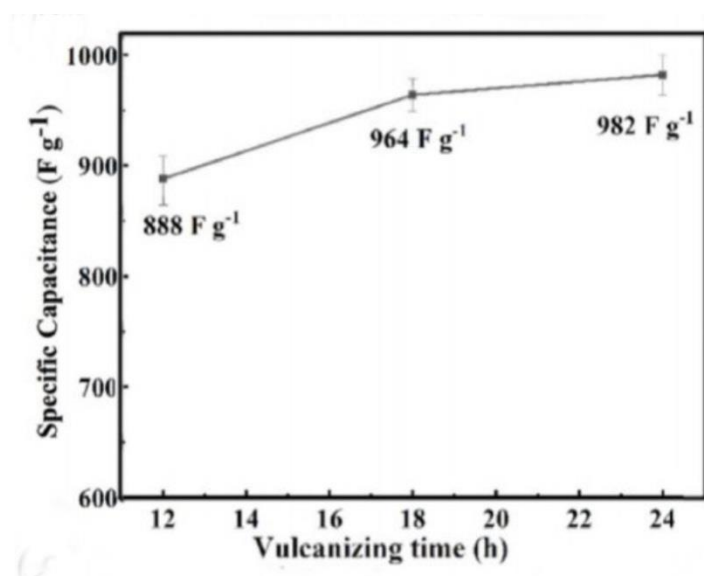
Fig.1.19. Electrochemical performance of the Ni$_3$S$_4$/CuS$_2$ at Specific capacitances changing with vulcanization time. [40]
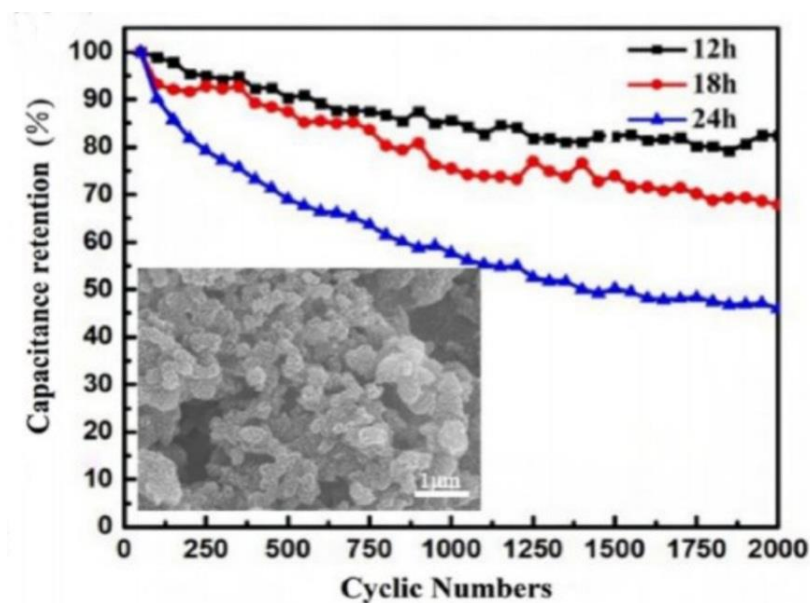
Fig.1.20. Electrochemical performance of the Ni$_3$S$_4$/CuS$_2$ at cycling performance. Inset: SEM image of Ni$_3$S$_4$/CuS$_2$ (12 h) after 2000 cycles. [40]

Moreover, the asymmetric supercapacitor (ASC) based on Ni$_3$S$_4$/CuS$_2$ demonstrated to have a high energy density of 49.68 Wh kg^{-1} at a power density of 400 W kg^{-1}, which stabilize at 25.67 Wh kg^{-1} when the power density increases to 3200 W kg^{-1}. Additionally, the ASC device displayed excellent cycling stability of 95.83% retention after 2000 cycles, as shown in Fig.1.21-22 [41].
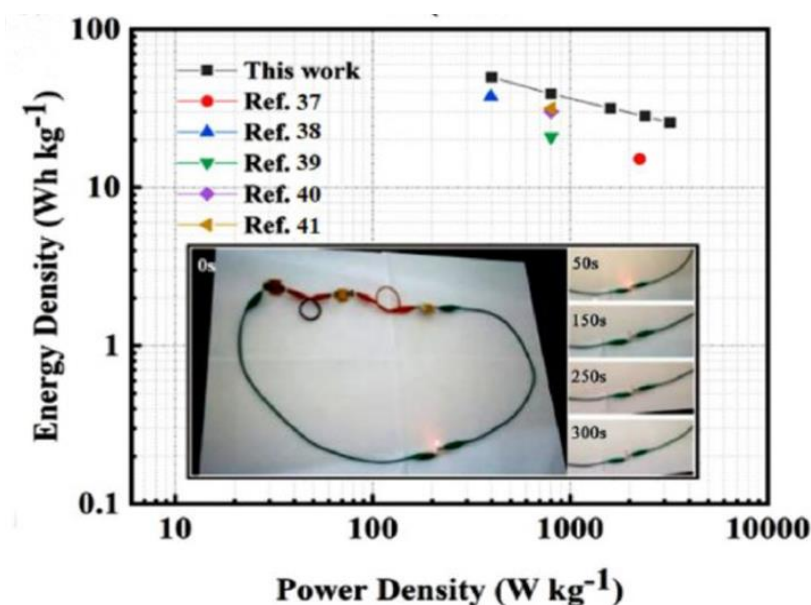
Fig.1.21.The electrochemical performance of the Ni$_3$S$_4$/CuS$_2$ (12 h)//RGO: cycling performance. [40]
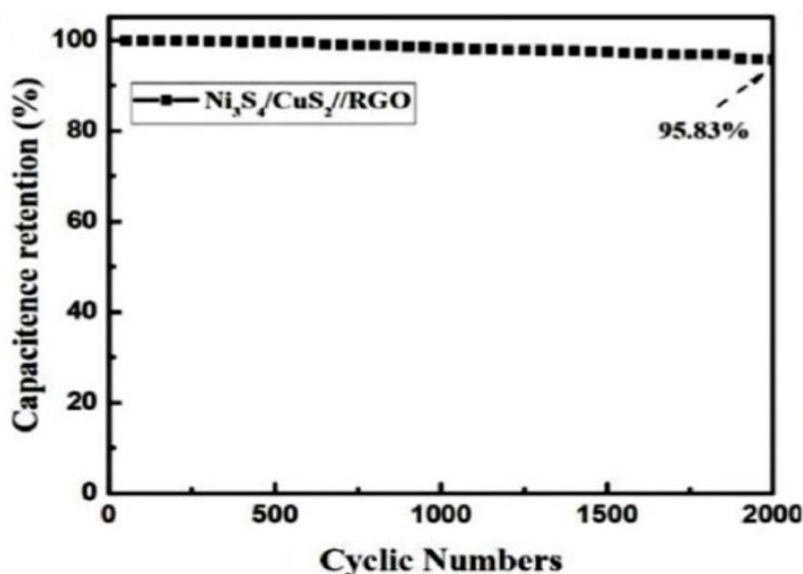
Fig.1.22.The electrochemical performance of the Ni$_3$S$_4$/CuS$_2$ (12 h)//RGO: Ragone plot.

2.4.8. Superconducting properties

CuS$_2$ is a material that exhibits superconductivity performance at low temperatures when it synthesized under high pressures. These properties are studying through specific heat, magnetization, and nuclear magnetic resonance measurements. The first measurements of specific heat for CuS$_2$ showed a superconducting transition temperature of $T_s = 1.5$ °K, which is relatively low compared to other superconductors. The broad nuclear magnetic resonance spectra observed in CuS$_2$, at low temperatures, can be explained by assuming an incommensurate charge-density wave transition occurs at 150 K. Based on these results, it can be said that CuS$_2$ is a promising candidate for further research in the field of low-temperature superconductivity. [32]

In addition, the Haas-van Alphen effect has first observed in the superconducting copper dichalcogenides CuS$_2$, CuSe$_2$ and CuTe$_2$, which have a pyrite-type crystal structure. The metallic properties of these compounds are attributed to the 3d electrons of eg symmetry associated with the copper atom, which partially fills the conduction band. The study used crude crystals synthesized at a

pressure of 65 kbar in a tetrahedral anvil apparatus, the crystals measuring approximately 1 mm square. The characteristics of these crystals are detailed in Table 1[41].

Tabel.2. Physical characteristics of measured compounds, cubic cell dimension, α(Å), room temperature resistivity, ρ (rm); resistivity ratio of sample measured, ρ(rm)/ρ(4.2°K), superconducting transition temperature, Tc (°K). [41]

	α(Å)	ρ (rm) (ohm-cm)	ρ (rm) (4.2°K)	Tc (°k)
CuS_2	5.790	1.5×10^{-4}	650	1.48 - 1.53
$CuSe_2$	6.117	7.5×10^{-5}	110	2.30 -2.43
$CuTe_2$	6.605	1.2×10^{-4}	130	1.25 - 1.3

Chapter 2

Techniques and Characterization

1. Introduction:

Climate change and all its consequences on the planet are essentially linking to the issue of energy, since the problem stems from the use of fossil fuels; these generate greenhouse gases, the most polluting gases, and carbon dioxide (CO_2) emissions. Sunlight is recognized as a clean and abundant source of energy that can meet our planet's energy demands and avoid the environmental problems associated with fossil fuels. Today, nanoscience and nanotechnology aim to study, create or apply materials, devices and systems that can control matter on a nanometric or even atomic scale. One of the interesting features of nanotechnology research is that, at the nanoscale, certain materials can have unique properties that differ from those of solid crystalline materials. These properties could make these materials very interesting for many technological applications such as optoelectronics, optical communications, solar control devices and solar cell manufacturing. Copper sulfide-based semiconductor thin films hold great promise for a wide range of applications. In addition to their abundance and low cost, they also exhibit optical and electrical properties dependent on Cu_xS_y stoichiometry [42].

2. Thin film deposition techniques

2.1. Chemical vapor deposition (CVD) process

CVD is a thin-film deposition process that involves the deposition of a solid material from a vapor through a chemical reaction occurring on or near the surface of a substrate. These processes vary in how the chemical reactions are initiated. During CVD, there can be volatile by-products and unused precursor species, some of which are highly hazardous, like H_2, Cl_2, HCl, HF, or water vapor. Therefore, proper safety measures are crucial, including vent flushing, removing by-products, and unreacted compounds. CVD can be classified based on the energy source used for the chemical reaction, such as photons, lasers, or heat (temperature) [38, 43]. There are several CVD processes, including metal-organic CVD, low-pressure CVD, atmospheric pressure CVD and plasma-enhanced CVD, which can vary in their implementation.

a. Metal organic CVD

Metal Organic Chemical Vapor Deposition (MOCVD) is a chemical vapor deposition technique using organometallic precursors [44]. MOCVD basically follows

the same process as CVD, but volatile organometallic compounds are used as precursors instead of inorganic compounds. This technique enables the deposition of a wide range of materials with amorphous, polycrystalline and epitaxial microstructures. Metal-organic compounds are decomposed by low-temperature pyrolysis reactions, enabling film deposition to be carried out at lower temperatures than in the case of thermal CVD [45]. Block diagram of typical metal organic chemical vapor deposition system is shown in Fig.2.1, which consists of following sub-units [47].
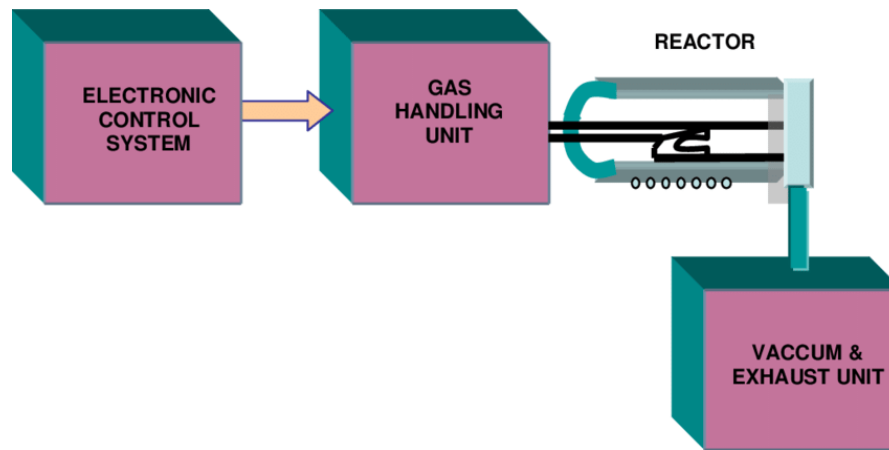
Fig.2.1. Metal organic chemical vapor deposition system. [47]

b. **Low pressure CVD**

LPCVD deposition systems are used to deposit thin films at low pressure in a high vacuum environment [47]. The systems typically operate at pressures ranging from 0.1 to 10 Torr, which considering a medium vacuum application. LPCVD reactors come in different configurations, including resistance heated tubular hot-wall reactors, vertical flow batch reactors, and single-wafer reactors. Throughout the latter part of the 20th century, horizontal hot-wall tube reactors were widely used for LPCVD processing. These reactors use precursor solution adsorption and subsequent surface reactions to deposit thin films. A schematic of a horizontal hot-wall tube reactor is shown in Fig.2.2 [48].
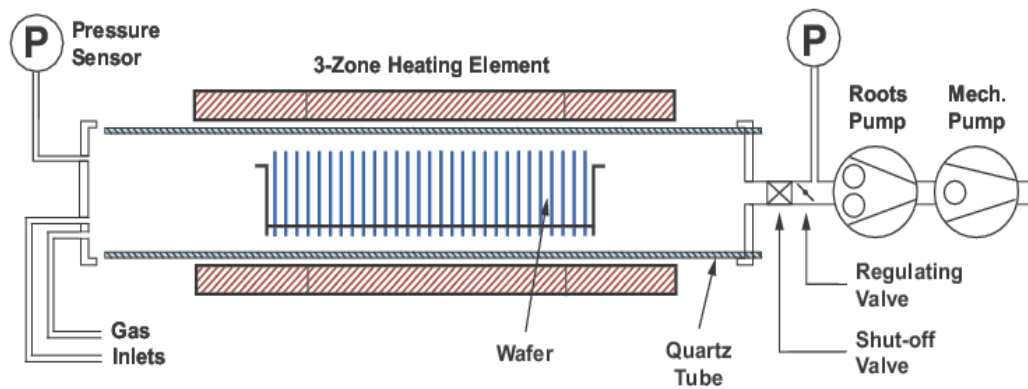
Fig.2.2 A horizontal hot-wall LPCVD reactor. [48]

c. Atmospheric pressure CVD

Atmospheric Pressure Chemical Vapor Deposition (APCVD) is a chemical vapor deposition reactor that operates at atmospheric pressure with a simple design and high deposition rates. It is the first of chemical vapor deposition used in the semiconductor industry; there are two-different types of continuous-processing APCVD system, the Gas-injection type and Plenum type [49].

APCVD is characterized by its low cost, scalability, high productivity, and mostly it is fine-tuning from monolayers to bilayers and low diffusivity coefficient [50].

d. Plasma enhanced CVD

Plasma enhanced chemical vapor deposition uses plasma to provide the energy required to facilitate the chemical reaction that drives the deposition. Electrical energy is used to create this neutral gas plasma. PECVD is performed at 2 – 10 Torr and relatively low temperatures from 200 – 400°C [51]. PECVD is a widely used technique to obtain device quality thin films at low substrate temperatures [52].

2.2. Physical vapor deposition PVD process

Physical vapor deposition (PVD) is a process used to create thin films or coatings on a substrate using vapors of the material to be deposited. This technique is widely used to deposit a range of materials, including alloys, refractory compounds, and polymers, onto a various range of substrates, as it illustrated in the bellow diagram.
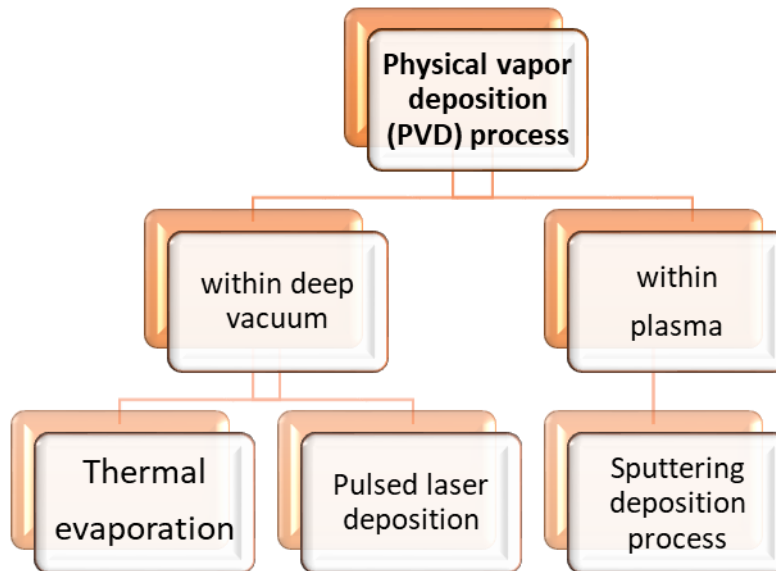
Fig.2.3 Physical vapor deposition process.

a. Pulsed laser deposition:

Pulsed-laser deposition (PLD) is a relatively new physical vapor deposition technique that has been widely employed for depositing a wide range of materials. This method utilizes a laser as a source to vaporize the desired material, making it a type of physical vapor deposition (PVD) [53]. In this method, a high-power density laser with a narrow frequency bandwidth is used to evaporate the target material, resulting in the ablation of atoms that are subsequently collected on the substrate. PLD is a popular technique used for the deposition of thin films in many fields such as electronics, optics, and material science. The advantage of PLD is that it allows for stoichiometric removal of the target material due to the fast, transient nature of the ablation process and the high laser fluence. PLD is used for the deposition of complex ceramic films that are difficult or impossible to deposit with other methods. However, stoichiometric removal does not always imply stoichiometric deposition. PLD also allows the user to tune the energy of the species arriving at the substrate by introducing an inert gas atmosphere such as argon, and it can be used to create nanoparticle deposition [54]. Figure2.4 shows a schematic diagram of a typical PLD process [55].
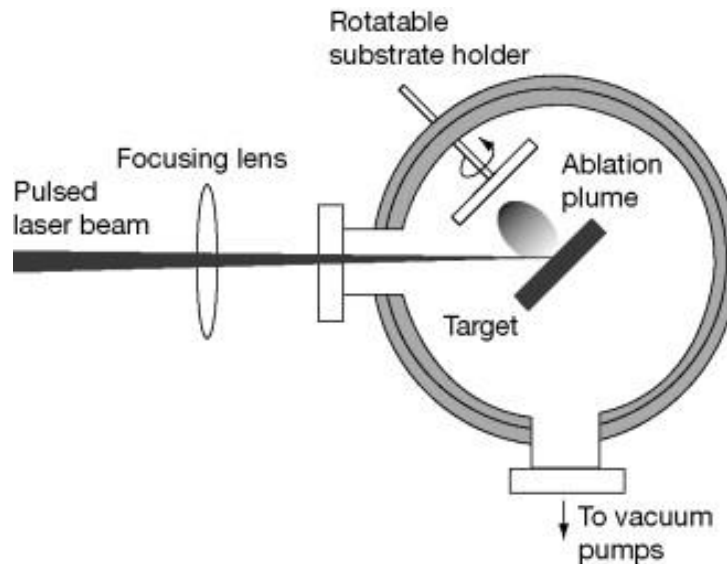
Fig.2.4 Schematic diagram of PLD process. [55]

b. Thermal evaporation:

Thermal evaporation involves heating a solid material inside a high-vacuum chamber, taking it to a temperature that produces some vapor cloud inside the vacuum, see Fig.2.5. This evaporated material constitutes a vapor stream, which traverses the chamber and hits the substrate, sticking to it as a coating or film. Thermal evaporation deposition has the advantages of being able to deposit thin film with low contamination at a controlled deposition rate. Moreover, larger charges (source materials) can be loaded per deposition run. However, it requires large and costly RF power supplies, step coverage is poor and control of film composition is more difficult than with sputtering [56].
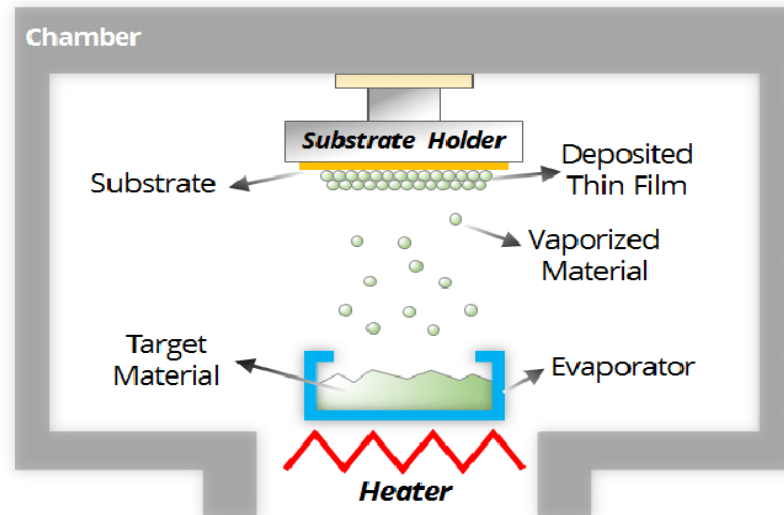
Fig.2.5 Scheme of thermal evaporation deposition. [56]

c. Sputtering deposition process:

The process of sputtering is a commonly used physical vapor deposition (PVD) technique that involves bombarding a target material with energetic particles, causing the ejection of atoms from the surface of the target. This vaporization process is achieving through ion bombardment, which results in a vapor that can then be deposited as a thin film onto a substrate. Thus, sputter deposition is a popular technique used to deposit thin films on substrates. By using ion bombardment, sputtering enables the physical vaporization of atoms from the surface of the target material, making it one of the most important PVD techniques available [57-58].

The sputtering process can be performed in either a DC (direct current) or RF (radio frequency) mode. In the DC mode, a high voltage is applied between the target and the substrate, while in the RF mode, a radio frequency is used to generate a plasma between the target and the substrate.AS shown in Figure2.6-7 [45].
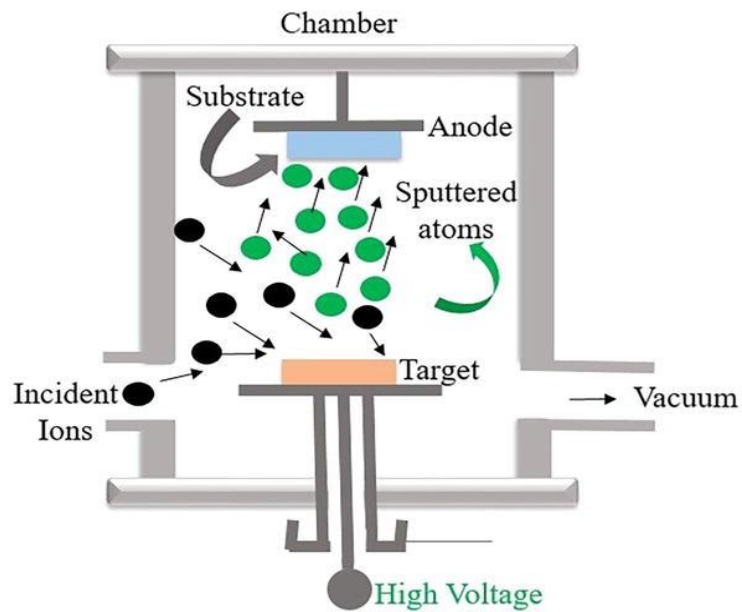
Fig.2.6 DC sputter deposition. [45]
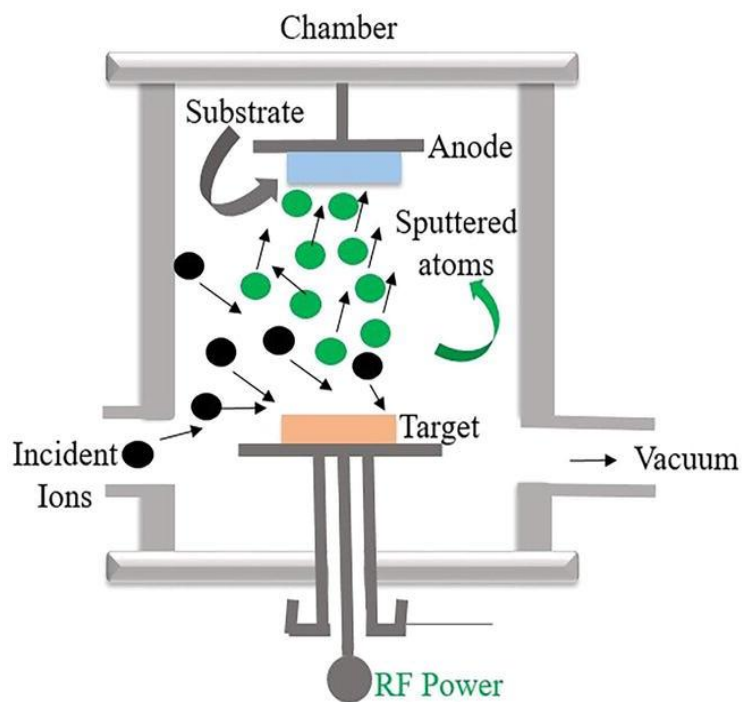
Fig.2.7 RF sputter deposition. [45]

2.3. Solution based chemistry (SBC) process

a. Chemical Bath Deposition Technique

Chemical Bath Deposition (CBD) is a simple and inexpensive technique, as it does not require elaborate conditions. All you need is a beaker containing the

reaction bath, into which glass slides are immersed, onto which the layer will be deposited. It should be noted that deposition generally takes place at atmospheric pressure and relatively low temperature, and has therefore been known since 1835, when Liebeg reported the first mirror by silver deposition in a chemical bath [59]. Since nearly 140 years ago, chemical bath deposition (CBD) has been used to deposit thin films of metal sulfides, selenides and oxides, as well as a number of different compounds. Although it is a well-known technology in some specific areas (notably photoconductive lead-salt detectors, photoelectrodes, and more recently thin-film solar cells), it is generally underappreciated technology. The development of CBD has been fuelled by recent interest in all things "nano", as it is a low-temperature aqueous solution technology where crystal size is often very small. This is demonstrated by the quantification of common magnitude in semiconductor thin films produced by CBD [60].
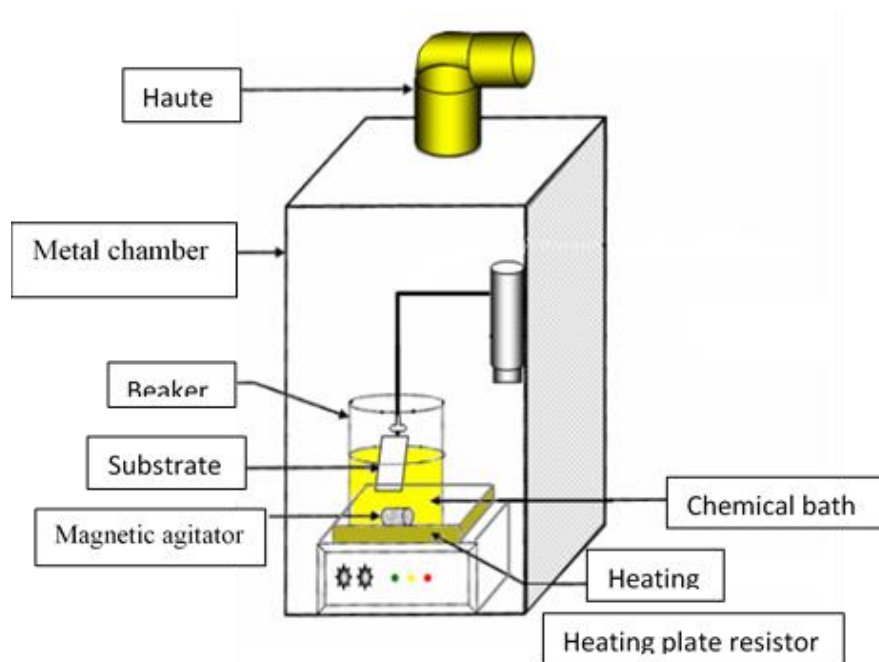
Fig.2.8 Diagram of the assembly of the deposition of Cu_xS_y by chemical bath. [61]

b. Sol-gel (solution-gelling)

The sol-gel method is a traditional method used for a wide range of materials, including inorganic membranes, monolithic glasses and ceramics, thin films, and ultra-fine powders. Today, it is even used to synthesize 1D nanomaterial. The advantage of this method, which has made it very popular, is the possibility of doing it at room temperature and the possibility of easy chemical doping **[62]**.

The process of sol-gel, as shown in Figure 2.9, involves chemical solution deposition in a sequential manner that includes hydrolysis and condensation, gel formation, aging, removal of solvents via evaporation or calcination, and, finally, crystallization. However, because of its effectiveness, this precursor approach can be expensive, result in lower production, and pose risks to the safety of the process [63].
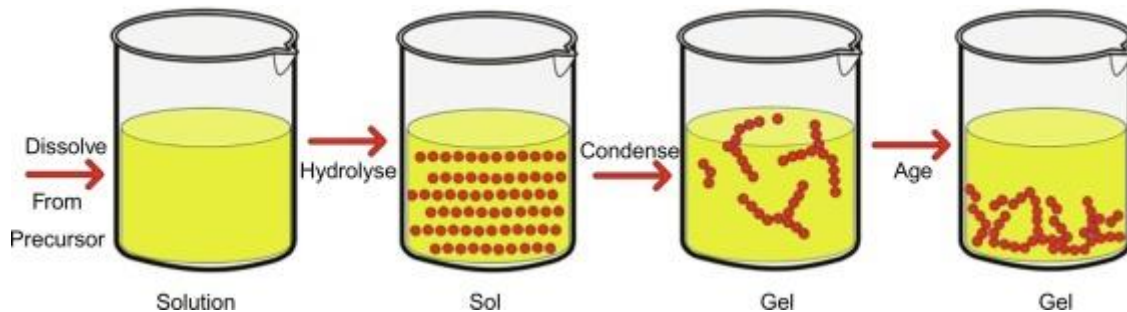
Fig.2.9 the basic process of the sol-gel method. [63]

c. Spin coating

Spin-coating (SC) is a solution-based process developed for low-cost deposition of thin films of materials ranging from polymers (as organic photoresists) to functional inorganic films including amorphous (Chern and Lauks, 1982) [64] and crystalline chalcogenides [53].

Spin coating is performed in four steps, deposition, spin up, spin off, and evaporation, as shown in Figure 2.10. In the first stage the material is deposited on the turntable, then spin up, and spin off occur in sequence while the evaporation stage occurs throughout the process. The applied solution on the turntable is distributed via centrifugal force. High spinning speed results in thinning of the layer. This stage is followed by drying of the applied layer. Uniform evaporation of the solvent is possible because of rapid rotation. High volatile components are removed from the substrate because of the evaporation or simply drying and the low volatile components of the solution remain on the surface of the substrate. The viscosity of the coating solution and the speed of rotation control the thickness of the deposited layer [65].
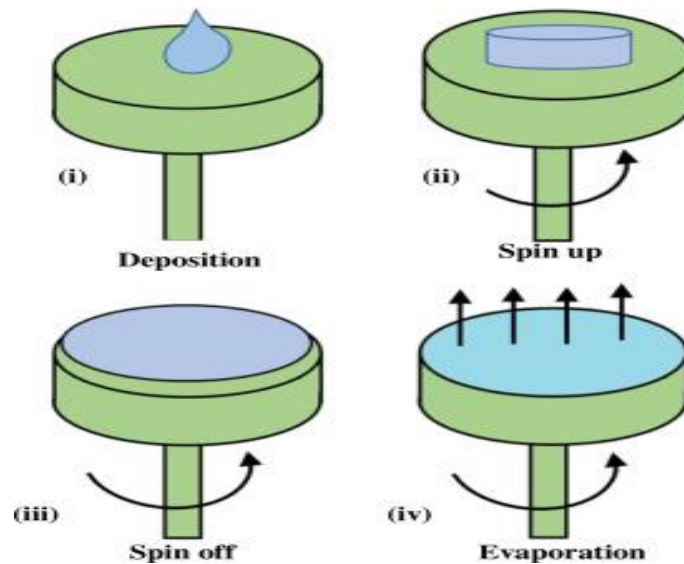
Fig.2.10 Stages of spin coating on substrate. [65]

d. Dip coating

Dip coating, also known as impregnation or saturation, is a commonly used method for applying a thin, uniform layer of coating to flat or cylindrical substrates [66]. The immersion coating technique for producing thin and thick films comprises several consecutive steps. First, the substrate is immersed in a solution containing the coating material at a constant speed. After a certain time, the substrate coated with a thin layer of material is removed from the solution at a constant speed. Excess liquid is evacuated from the substrate and the solvent in the coating material evaporates, forming the thin film. The properties and thickness of the film obtained depend on various factors, such as immersion time, withdrawal speed, number of dipping cycles, solution composition, concentration and temperature, environmental humidity, and others [67].
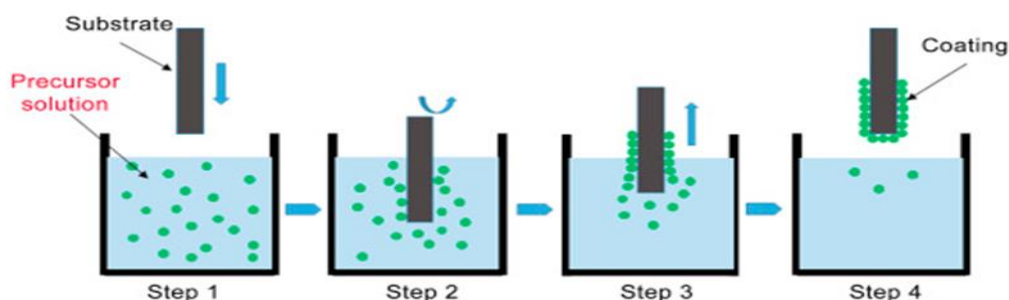
Fig.2.11. Representation of dip-coating technique. [68]

e. Spray pyrolysis

Spray pyrolysis is a process in which a precursor solution is atomized in a droplet generating apparatus, is evaporated in a heated reactor, and then is decomposed into particles and films [69].

Spray pyrolysis is very efficient, cost effective, and utilizes simple equipment. The thin films produced have large surface area of substrate coverage and potential and homogeneity of mass synthesis. However, spray pyrolysis seems not useful due to poor quality of thin film, thermal decomposition, and vapor convection. The vapors are generated due to temperature difference, which restricts the source from binding with the substrate. The spray pyrolysis process is shown in Fig. 2.12 [70].
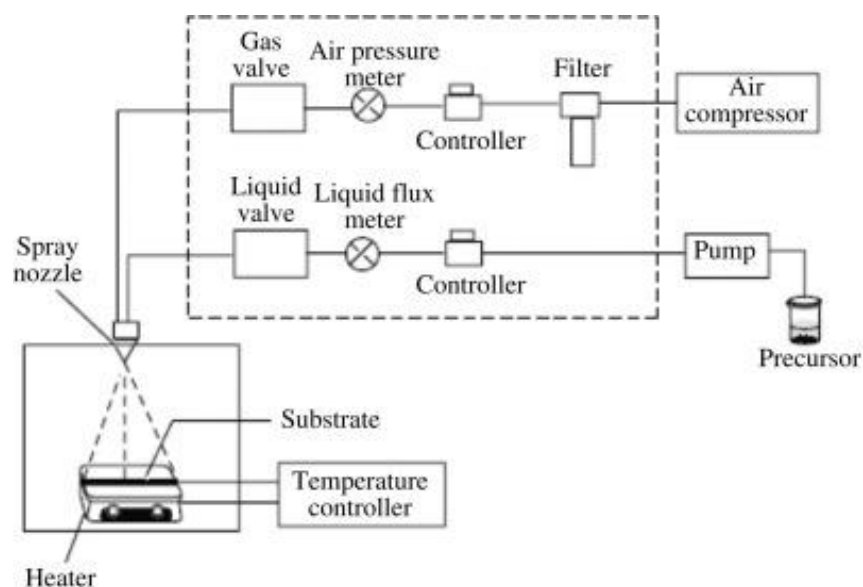
Fig.2.12. Mechanism of spray pyrolysis. [70]

f. The method of electrochemical deposition (electrodeposition)

Electro-deposition is a non-vacuum electrochemical technique highly preferable for thin film deposition owing to its ability to deposit multicomponent alloys at low temperature. In this method deposition of thin metallic films is done onto the substrate by the reduction of cations without any unwanted reactions [71]. The process of electro-deposition involves the electrolytic reduction of a metal (M) that deposits onto a metallic substrate: $M^+ + e \rightarrow M$. Both electrodes are immersed in a solution called an "electrolyte" containing one or more dissolved metal salts whose ions allow the circulation of electricity. At the cathode, the metal ions are reduced and

deposited as a thin layer. The ions in the electrolyte bath are constantly replenished by the anode, which is oxidized by the power supply providing a continuous current. Electroplating is therefore an effective method of depositing thin metal layers on a substrate without undesirable reactions, and it enables low-temperature deposition of multicomponent alloys, see Fig.2.13 [72].
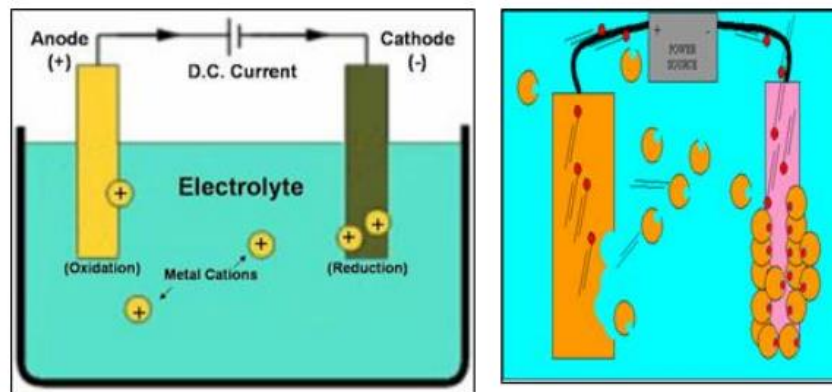
Fig.2.13. Experimental setup of electrodeposition. [72]

3. Characterization techniques

Characterization techniques are a set of experimental methods and tools used to study and analyze the properties and characteristics of materials or systems. These techniques are essential to scientific research and engineering to understand the behavior and properties of materials, and how they interact with their environment.

Functional characterization techniques focus on the performance and behavior of a material or system under specific conditions. These techniques provide information on physical, chemical, mechanical, electrical, and other properties of the material. Examples of functional characterization techniques include thermal analysis, rheology, tensile testing, corrosion testing, and surface analysis.

Overall, characterization techniques play a critical role in advancing scientific knowledge and technological development, allowing researchers to gain a deeper understanding of materials and their properties and enabling the design and optimization of new materials and systems for various applications [73].

a. AFM atomic force microscope

Atomic force microscopy (AFM) is a powerful and versatile observation method that uses the atomic force between the probe and the sample surface. This technique can image a wide range of surfaces, including polymers, ceramics, composites, glasses and biological samples. In addition to imaging capabilities, AFM is used to accurately measure and locate various forces, such as adhesion strength, magnetic forces and mechanical properties. The AFM configuration comprises a sharp tip, typically 10 to 20 nm in diameter, which firmly attached to a cantilever, enabling precise scanning and analysis of the sample surface [74,75].

With AFM, the sample is prepared by immobilizing it on a substrate and ensuring that the surface is clean. A pointed probe with a nanometric tip is selected to interact with the sample surface. The probe gently contacts the surface using different imaging modes such as contact, tap or non-contact. The probe systematically scans the surface, controlled by piezoelectric elements. The interaction between the probe and the sample generates a signal, which is converted into a three-dimensional image or topographical map of the surface. The acquired data is then analyzed using specialized software to extract information on surface morphology, height variations and other properties [76].

Figure 2.14 illustrates the principle of atomic force microscopy; the cantilever is mounted on a piezoelectric scanner, which allows either movement in the horizontal (x, y) or vertical (z) dimension. The tip is brought close and scanned across the sample surface while moving vertically [77].
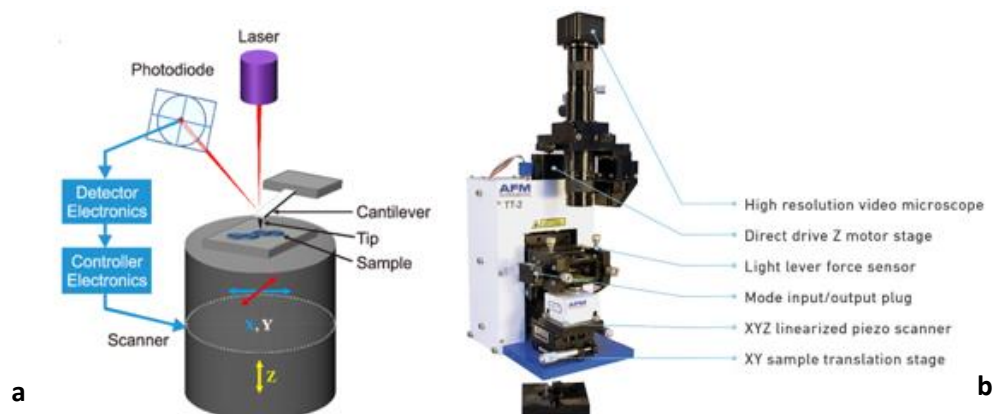
Fig.2.14. Schematics of atomic force microscopy principle. [77]
(b) Atomic force microscopy. [77_1]

36

b. X-Ray diffraction (XRD)

Wilhelm Röntgen discovered X-rays in 1895. X-ray diffraction (XRD) is used in many applications, including medical imaging and crystal characterization, which is a non-destructive structural analysis technique for identifying the crystalline phases present in a sample, as well as determining lattice parameters and average crystallite size [78,79].

Bragg's law governs x-ray diffraction. Therefore, x-rays are producing by the braking of high-speed electrons near the anode in X-ray tubes. When these electrons strike the anode, they undergo rapid deceleration, resulting in the emission of X-ray photons. The energy of these photons is of the order of KeV characteristic of the nature of the anode material [80].

Once X-rays are generated, they can be applied to crystal lattices, where Bragg's law comes into play. According to Bragg's law, when X-rays interact with a crystal lattice, they undergo constructive interference if the difference in trajectory between the rays scattered by successive atomic planes satisfies a specific condition as follows:

$$n\lambda = 2\text{d}\sin\theta \tag{2.1}$$

Where: n is an integer (1, 2, 3...n), λ is the X-ray wavelength, d is the distance between the atomic planes, and θ is the angle of incidence of the X-ray beams. An X-ray beam takes a longer (but parallel) path because if 'reflects' off an adjacent atomic plane. This path length difference must equal an integer value of the 1 of the incident X-ray beams for the constructive interference to occur such that a reinforced diffracted beam is produced. By satisfying Bragg's law, X-ray diffraction patterns are observed, providing valuable information about crystal structures, interatomic distances, and lattice parameters. Therefore, the generation of X-rays and the application of Bragg's law are interconnected, playing essential roles in X-ray diffraction analysis and its wide-ranging applications in various scientific fields. Figure.2.15 illustrates the principle of Bragg's law [80,81].

$$n(\lambda) = 2d \sin(\theta)$$

$AB = d \sin(\theta) = BC \quad \therefore \quad ABC = 2d \sin(\theta)$

$A'B' = 2d \sin(\theta) = B'C' \quad \therefore \quad A'B'C' = 2ABC = 4d \sin(\theta)$
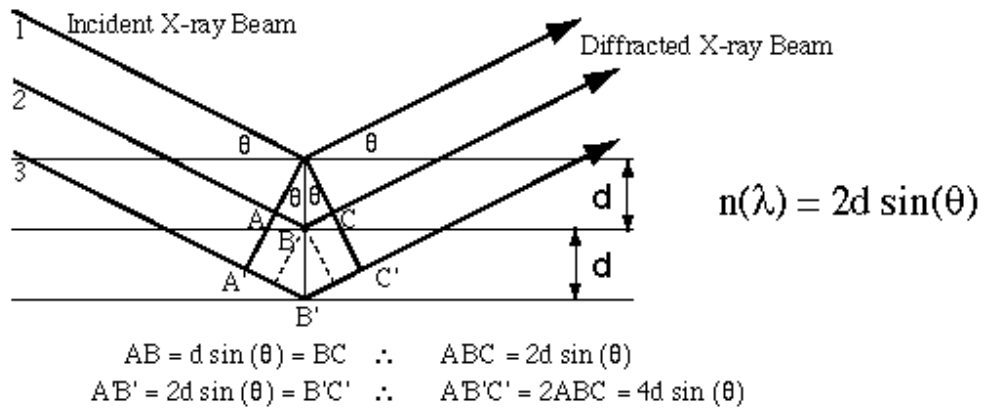
Fig.2.15.Schematic representation of X-ray diffraction by a crystal (Bragg's law). [81]

The diffractogram is a recording of the diffracted intensity as a function of the 2θ angle formed with the direct beam Figure2.16. The study of the diffractogram provides a wealth of information about the structural characteristics of the sample. The angular positions of the diffraction peaks are indicative of the parameters of the crystal lattice. By analyzing the positions of the diffraction peaks, it is possible to determine the crystal lattice of each crystalline phase present in the sample. Once the lattice is determined, the angular positions of the peaks can be used to calculate the interplanar distances of the diffracting atomic planes and access the parameters of the unit cell. [82]
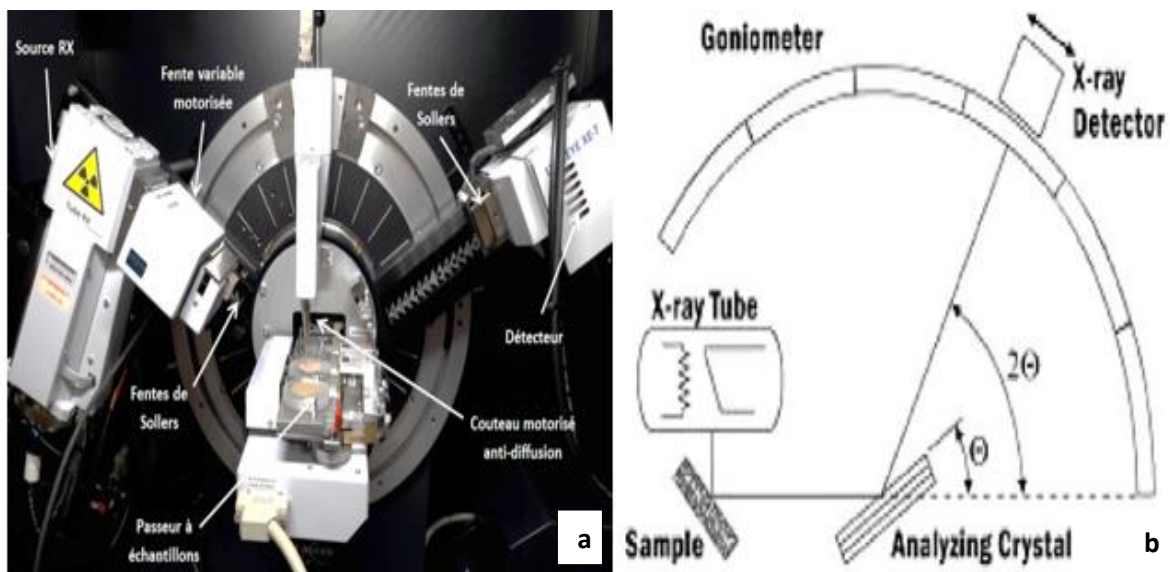
Fig.2.16.(a) *Appareil en configuration DRX - theta/theta Bragg Brentano.* [80_1]
(b).Schematic diagram of a diffractometer system. [80]

c. Gas chromatography (GC)

James and Martin have traditionally introduced the Gas Chromatography for the first time in 1952 [81]. Analytical gas chromatography (GC), as depicted in Fig.2.17, is a technique of separation of components of mixtures (samples) with the purpose of obtaining information about their molecular composition. The information obtained from a chromatographic analysis can include a chromatogram (a graphical image of a detector output), information regarding the heights and the areas of resolved (adequately separated) peaks in a chromatogram, their molecular identity, etc.… [84].
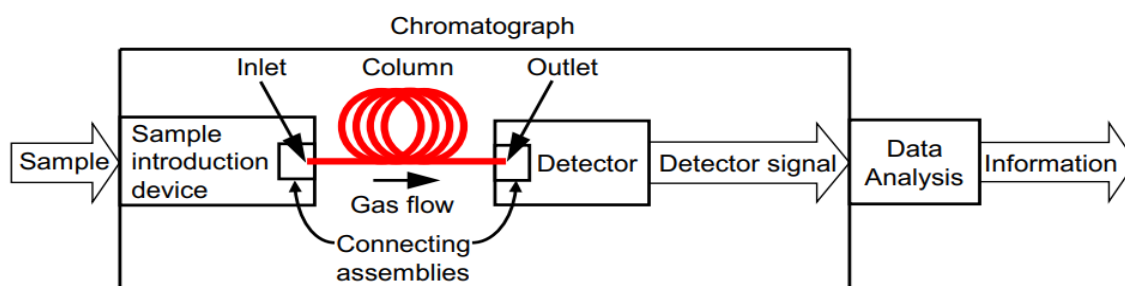
Fig.2.17.Block diagram of a chromatographic system. [84]

Gas chromatography comprises two main types: gas-liquid chromatography (GLC) and gas-solid chromatography (GSC). In gas-liquid chromatography, a sample of a volatile compound is mixed with a gaseous mobile phase and passed through a stationary phase consisting of a non-volatile liquid. In contrast, gas-solid chromatography uses a solid stationary phase, and separation of compounds is by adsorption, resulting in significantly longer retention times than gas chromatography. Gas chromatography, also known as gas-liquid chromatography (GLC), is a specific chromatographic method that uses an inert gas mobile phase and a liquid stationary phase. Although advances have been made in instrumentation, the fundamental principles of gas chromatography - the instruments used to perform GC - have remained relatively simple and constant over time [85].

This technique has many applications, both quantitative and qualitative. These include:

a. Environmental analysis: pesticides' analysis in water/vegetables, vehicle emissions

b. Clinical medicine: blood alcohol, drugs (nicotine, opioids)

c. Forensic medicine: explosives

d. Consumer goods quality control

e. Food analysis: fatty acid composition, flavor components of edible products

f. Petrochemicals, petrol composition, solvent purity, gas refineries [86].

d. Scanning Electron Microscopy (SEM)

Scanning Electron Microscopy (SEM) is a powerful imaging technique that uses a focused beam of electrons to examine the surface of solid materials. It provides high-resolution, three-dimensional images of the sample's surface morphology at the micro and nanoscale. SEM allows for the visualization of surface features, such as texture, shape, and composition, and offers versatile capabilities beyond traditional topographic imaging in the magnification range 10–10,000×. With its broad applications in various scientific fields, SEM plays a crucial role in materials science, nanotechnology, biology, geology, and other disciplines for detailed surface characterization and analysis [87].

The SEM captures images by utilizing a focused electron beam that scans a rectangular area of the specimen in a raster pattern. The electron beam originates from a filament, typically made of various materials, with tungsten being the most common choice as the cathode. When the metallic filament is heated, it generates a beam of electrons at the top of the microscope. This electron beam passes through the microscope's column, guided by electromagnetic lenses that focus and direct it onto the sample.

As the electrons in the beam interact with the atoms of the sample material, they are scattered back, resulting in the formation of either backscattered electrons or secondary electrons. These scattered electrons are collected by a detector, which converts them into a signal that is transmitted to a viewing screen, similar to a television screen. This process generates an image (Figure.2.17) that contains detailed information about the surface topography, composition, and other properties of the sample, such as electrical conductivity.

Vacuum is an essential requisite for SEM. If the sample is in a gas filled environment, the beam is unstable as gases could react with the electron source, causing it to burn out or result in ionization of beam. Alternatively, other molecules, which come from the sample or the microscope itself, may form compounds,

condense on the sample, and thereby reduce contrast and obscure details in the image. [88]
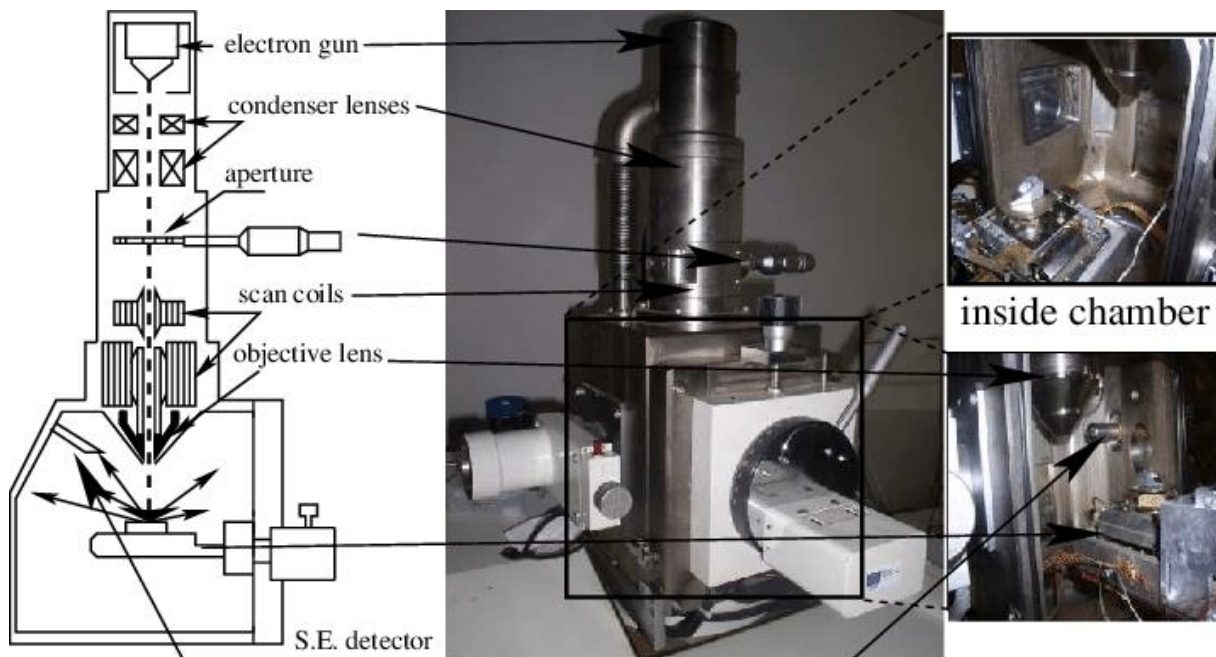
Fig.2.18.Schematic flow diagram of a Scanning Electron Microscope. [88_1]

e. Raman spectroscopy

Raman spectroscopy, which emerged from the discovery of the Raman Effect in 1928 by Indian physicist C. V. Raman, is experiencing a renaissance that has opened up a series of advanced techniques. Exciting developments in the optical, quantum mechanical and spectroscopic fields during the past few decades have provided new insights into research on nanomaterials. This analytical technique uses scattered light to measure the vibrational energy modes of a sample, providing both chemical and structural information. By detecting Raman scattering from the sample, Raman spectroscopy can identify substances through their characteristic Raman 'fingerprint', extracting valuable information about the sample's composition and structure. [89] Figure.2.19 shows the process involved in collection of Raman spectra. When the sample is illuminated by an incident monochromatic light, the majority of the scattered light is of the same wavelength elastically scattered (green arrow). A notch filter is therefore used to block the elastically scattered light, which would otherwise overwhelm the weak signal of the Raman, or inelastically scattered light (orange arrow). Scattered Raman light disperses on wavelength-dependently across

a grating and detected by a charge-coupled device (CCD) detector. A Raman spectrum is finally displayed during software analysis [90].
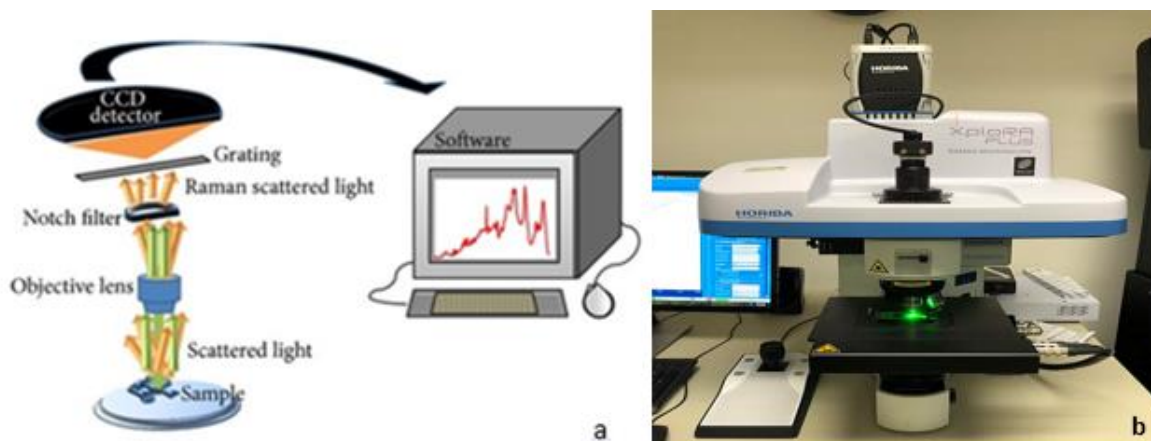
Fig.2.19. (a) Schematic showing the process involved in Raman spectra collection. [90] (b) Raman spectrometer from S & N lab. [90_1]

f. Fourier transforms infrared spectroscopy (FTIR)

The origins of infrared spectroscopy date back to 1800, when William Herschel discovered the infrared region of the electromagnetic spectrum. In the 1930s and 1940s, advances in electronics led to the introduction of infrared thermocouples. The appearance of the first Fourier transform infrared (FTIR) spectrometers in the early 1970s transformed infrared spectroscopy from a research tool into a dominant analytical technique, giving rise to modern infrared spectroscopy.

Infrared spectroscopy is a powerful and widely used analytical technique based on the absorption of infrared radiation by a material. It can be used to characterize the chemical functionalities of organic and inorganic substances, whether crystalline or amorphous, by comparing their infrared absorption spectra with those of reference substances. It also provides information on the nature of chemical bonds. This technique is particularly sensitive to the vibrations of chemical bonds with a dipole moment. Modern infrared spectroscopy is used in many fields, including polymers, agriculture and food science, geological samples, the pharmaceutical industry and biological and medical analysis [91].

• Principal of FTIR

The IR spectrum is dividing into three wave-number regions: the far-IR spectrum (<400 cm^{-1}), the mid-IR spectrum (400-4000 cm^{-1}) and the near-IR spectrum (4000-13000 cm^{-1}). The infrared region between 4000 and 400 cm^{-1}

corresponds to the range of all molecular vibrations. The infrared spectrum of a sample is obtained by introducing infrared light beam through the sample. When the wavelength of the emitted beam is close to the vibration energy of the molecule, the molecule absorbs the radiation, resulting in a decrease in the intensity reflected or transmitted. As a result, the energy of the IR radiation is reduced after the interaction. This technique detects the characteristic vibrations of chemical bonds between two atoms, enabling chemical composition analysis and direct access to the molecular structure of the materials analyzed [92].

- **The equipment of FTIR**

Modern spectrometers use source that emits the entire infrared (IR) wavenumber range in a single beam, see Fig.2.20. The splitter separates the emitted beam into two; however, a mirror reflects each part, in which one of the mirrors is fixed, while the second is movable. This combination of mirrors and beam splitters forms the interferometer.

By changing the position of the moving mirror, a step difference is created between the two separated beams, resulting in the formation of interferograms. These interferograms are then converted, using the Fourier transform, into what corresponds to a point in the IR spectrum. The complete spectrum is obtained by changing the position of the moving mirror to scan the desired range [93].
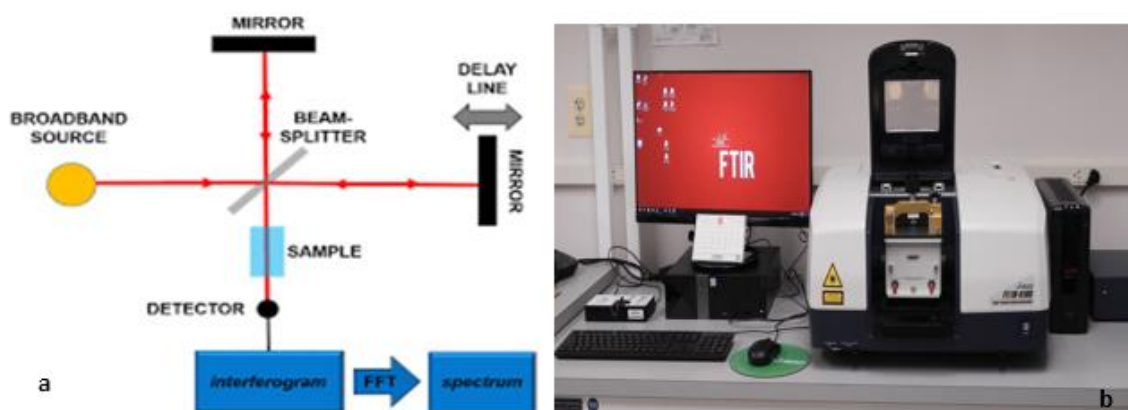
Fig.2.20. (a) Principles of the Fourier-Transform Infrared Spectroscopy (FTIR) [93]. **(b) FTIR Analysis – Infrared Spectroscopy.**

g. Ultraviolet–visible–Infrared spectrophotometer:

UV and visible absorption spectroscopy is a widely used characterization method in laboratories, which is a preferred technique for both qualitative and, more importantly, quantitative analysis of numerous species (thin films and powders). This

technique provides information about the optical properties of the sample being analyzed, such as light transmission and absorption.

An atom can react with incoming light. It can either scatter the light or absorb it. During scattering, light may be redirected or alter the direction. In case of absorption, the atom makes a quantum jump to one of its higher energy level after absorbing light. Absorption coefficient α is the property of material which gives the amount of light absorbed by it. The inverse of absorption coefficient is the average distance travelled by a photon before it gets absorbed. The absorbance is given by:

$$A = \alpha.C.L \tag{2.2}$$

Where, α: Absorption coefficient, c: concentration, L: path length .The ratio of intensity of transmitted light and intensity of incident light (I/I_0) are called the transmittance (T). Relation between absorbance (A) and transmittance (T) is:

$$A = log_{10}\left(\frac{I_0}{I}\right) = log\left(\frac{1}{T}\right) \tag{2.3}$$

Absorbance and absorbance coefficient are calculated by using Spectrophotometer. If E is the energy of the incident light and Eg is the band gap energy of the semiconductor, then we have Tauc's formula:

$$\alpha h\nu = A(h\nu - E_g)^n \tag{2.4}$$

Where "n" depends on nature of transition and can have values 1/2(allowed) and 3/2(forbidden) for direct transition; 2(allowed) and 3(forbidden) for indirect transition. The principle of this characterization technique is shown in Fig.2.21. It involves a double-beam configuration, where a UV-visible light beam is directed towards a monochromator composed of a prism or grating. With using mirrors, the beam is then directed towards a beam splitter, which simultaneously sends a reference beam and a beam that passes through the sample. The two beams are subsequently collected and converge towards the detector. [94]
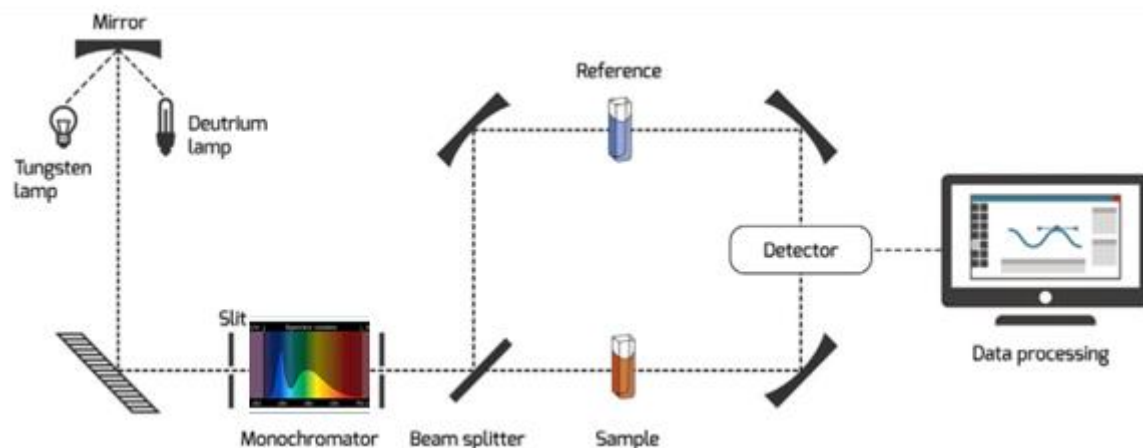
Fig.2.21. Schematic representation of UV-Vis-IR spectroscopy. [94]

h. Thermoluminescence Spectroscopy (TL)

Thermally stimulated luminescence (TSL) involves generating light when a solid is heated. Light becomes visible after the solid has been exposed to radiation, with heat triggering this effect. TSL is primarily employed for measuring radiation doses, as it exhibits a proportional relationship between emitted light and the absorbed radiation dose in certain materials. However, in the 1950s, it was recognized that TSL could be used not only for dosimetry and dating, but also for other purposes such as measuring the efficiency of surface catalysts and measuring impurities in rocks. Thermoluminescence is also very sensitive to defects in the material under investigation and can also be used to investigate these defects. [95].

Over the last two decades, computerized deconvolution of thermoluminescence glow curves has become the method of choice for TL glow-curve analysis. This method is used to evaluate TL kinetics parameters for a given peak in the glow-curve, but it is also applied nowadays in routine radiation dosimeters. Several models, approximations and minimisation procedures have been investigated and a number of computer programs have been developed for TL glow-curve analysis. [96]

As shown in Figure.2.22, the light emission occurs when the sample is heated above 200°C. Initially, a blue range of light is observed, but as the temperature increases, the emitted light shifts to a red glow. However, during a second heating, only the red glow is observed, and the blue light emission is absent. The origin of thermoluminescence lies in the release of energy stored within the crystal lattice structure of the material. This energy accumulation happens over time due to exposure to nuclear radiation from natural sources, both internal and external.
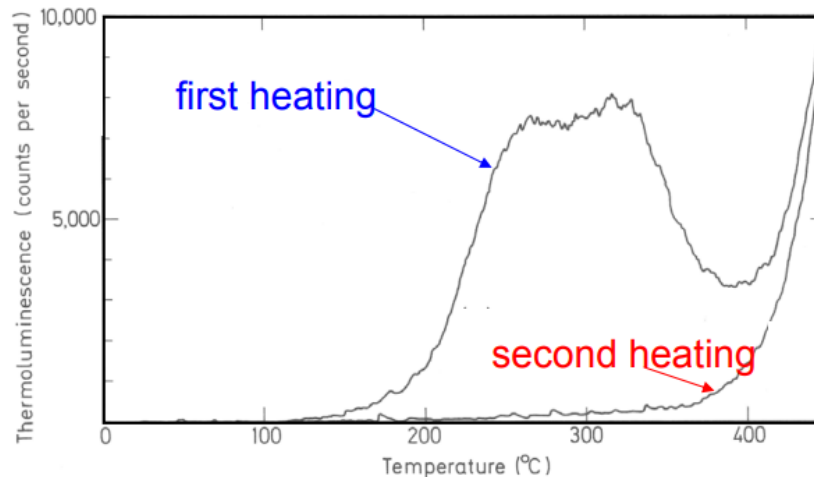
Fig.2.22.Thermoluminescence as the function of temperature. [97]

The amount of thermoluminescence accumulated in a material is directly proportional to its radiation exposure. Upon heating, this accumulated energy is released, resulting in light emission. In the context of dating, the clock starts ticking at the initial firing of the material, when the previously accumulated thermoluminescence is driven out. [97]

In summary, thermoluminescence is a characteristic property displayed by certain materials. The heating of these materials causes the release of stored energy, resulting in light emission. This energy accumulation and release have implications in various fields, including dating techniques based on thermoluminescent properties.

i. X-Ray Fluorescence Spectroscopy (XRF)

X-ray fluorescence spectrometry (XRF) is an analytical technique widely used for elemental determination in industrial and R&D laboratories. It belongs to the family of atomic spectrometry techniques, but offers certain analytical advantages over competing techniques such as atomic absorption spectrometry (AAS) and inductively coupled plasma atomic emission spectrometry (ICP-AES). XRF spectrometry is capable of determining almost all elements of the periodic table, conventionally between sodium and uranium (including electronegative elements such as chlorine, phosphorus, sulfur, bromine and iodine) at detection limits, often of the order of 1 to 10 mg kg-l. Determinations can be extended to uranium. Determinations can be extended to boron, albeit with reduced sensitivity and significant limitations in terms of the very low critical penetration depth of the corresponding fluorescence X-rays [98].Figure2-23 shows An XRF spectrometer, with

the sample port on top, and a set of samples in silver metallic holders in the sample changer in front.

Fig.2-23.X-ray spectrometer. [98_1]

XRF is used in some laboratories in forensic investigations of concrete to determine the elemental composition of samples. The electromagnetic radiation of wavelengths of x-rays ranges between 0.1 Å and 20 Å. The necessary wavelengths are produced by an x-ray tube in which the electrons are accelerated from an emitting source toward the target material. Under radiation from an x-ray source, a sample will emit characteristic X-ray intensities depending on characteristics of the beam, sample elemental concentration, powder particle size distribution, degree of compaction, and the compounds in the matrix. A detector that collects and reports the intensities of the emitted x-rays, which in turn can be used in a calibrated system to determine the relative proportions of elements in the sample, is shown in Figure 2.23 [99].
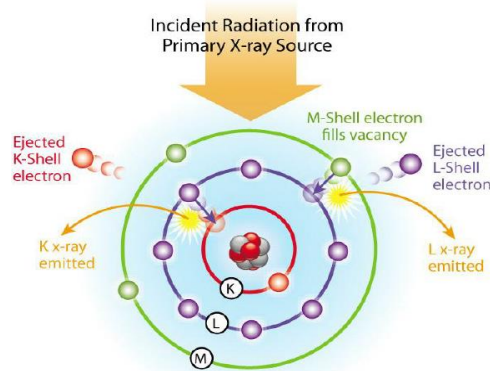
Fig.2-24.X-ray fluorescence principale. [99]

Chapter 3

Results and discussion

1. Introduction:

Gas separation plays a crucial role in various industries [100], such as petrochemicals, natural gas processing, and air purification. Efficient and selective separation of different gases is essential for optimizing industrial processes and reducing environmental impacts [101]. A gas separation filter is a screen between two adjacent thin layers acting as a selective barrier. It uses membranes to selectively separate gas molecules according to their size, shape and/or chemical properties, making it a potential alternative to conventional gas separation processes [1-3]. Membrane separation processes offer several advantages over conventional gas separation techniques. They require no additional chemicals or solvents, and eliminate the need for energy-intensive phase transformation processes [100].

In recent years, researchers have been exploring novel materials with superior gas separation properties, and one such material that has gained significant attention is a copper sulfide (CuS_2). The compound is a composed of copper and sulfur atoms, and its unique properties make it a promising candidate for gas separation applications [11-13]. CuS_2 exhibits excellent thermal and chemical stability, which is vital for withstanding harsh operating conditions. Additionally, its low cost and abundance make it an attractive alternative to expensive and scarce materials currently used in gas separation processes [11-13].

The purpose of this chapter is to present the experimental part and the results obtained in this work regarding the elaboration and characterization of copper disulfide (CuS_2) thin films. The first part of the chapter discusses the elaboration method used for the deposition of thin films based on CuS_2, while the second part focuses on the characterization techniques employed to determine the different properties of these thin films. Detailed discussion and interpretation of the obtained results will be providing.

2. Experimental part:

2.1. Preparation of substrate and the deposit solution

First, all substrates are immersed in a concentrated 4:1 H_2SO_4/H_2O_2 solution at 80°C, followed by immersion in a 1:1 HCl/H_2O_2 solution at room temperature. Finally, the substrates are immersed in a 10% HF solution at room temperature for 1 minute. All chemical processes are completed by rinsing with demineralized and

deionized water, followed by drying with pure nitrogen gas (N_2). Next, in the first part, electroless bath deposition is carried out to deposit CuS_2 films with the aid of a bias current. First, the aqueous medium is $Cu(SO_4)_5H_2O$ copper sulfate pentahydrate as a cation source. Next, sodium thiosulfate Na_2SO_4 was used as a source of anions. Next, citric acid ($C_6H_8O_7$) was used as a complexing agent, and thioacetamide, an organo-sulfur compound of formula C_2H_5NS, was also included. All precursors were prepared, with fixed molarities, using standard techniques. A quantity of powdered copper sulfide clusters was added to ensure compliance with chemical compound requirements. The pH of the solution was adjusted to 3 by adding citric acid ($C_6H_8O_7$) and a few drops of hydrochloric acid. The bath was maintained with a potential generator set at 5V, and the solution vigorously stirred. The temperature was set at 35°C. We then prepared four series of samples, varying the deposition time to 30, 60, 120 and 180 minutes.

In the second part, we proceeded to deposit the copper sulfide powder generated by the crystallization through the preparation of the deposition solution. By using a vacuum evaporation technique, we elaborate three samples (Annealing of Cu_xS_y was performed at temperatures of 450°C, 500°C, and 550°C). We then elaborate an addition sample of a thin film based on pure Cu, as reference.

3. Results part
3.1. <u>X-ray Diffraction (XRD) spectra:</u>

In this study, X-ray diffraction (XRD) was employed to analyze the structural properties of both powdered samples and thin films. XRD is a powerful technique that provides valuable information about the crystal structure, phase composition, and preferred orientation of materials. The obtained diffraction patterns, we analyze results using the High score Plus software.

Fig.3.1 (A-B) presents the X-ray diffraction Pattern of CuS powder and CuS_2 powder in an angle range $15<2\theta<50°$, respectively.

In the first one, the result reveals the formation of two phases: Cu_2S (black asterisk) and CuS (red diamond), with CuS being the majority phase. We observe the presence of CuS main peaks (JCPDS, Ref code: 01-078-0877) located at 2θ angles of around 22.5°, 24°, 27.5°, 28°, 29.5°, 32.5°, 34.5° and 48.5°. In addition, a series of

peaks, other than those of the target phase, attributed to the hexagonal structure of Cu_2S, are of lower intensity but sufficiently visible to be taken into account. These peaks are located at 2θ angles of around 26.5°, 33°, 37°, 38°, 41.5°, 46° and 48.5°, determined by comparison with JCPDS, Ref Code: 01-073-1138.
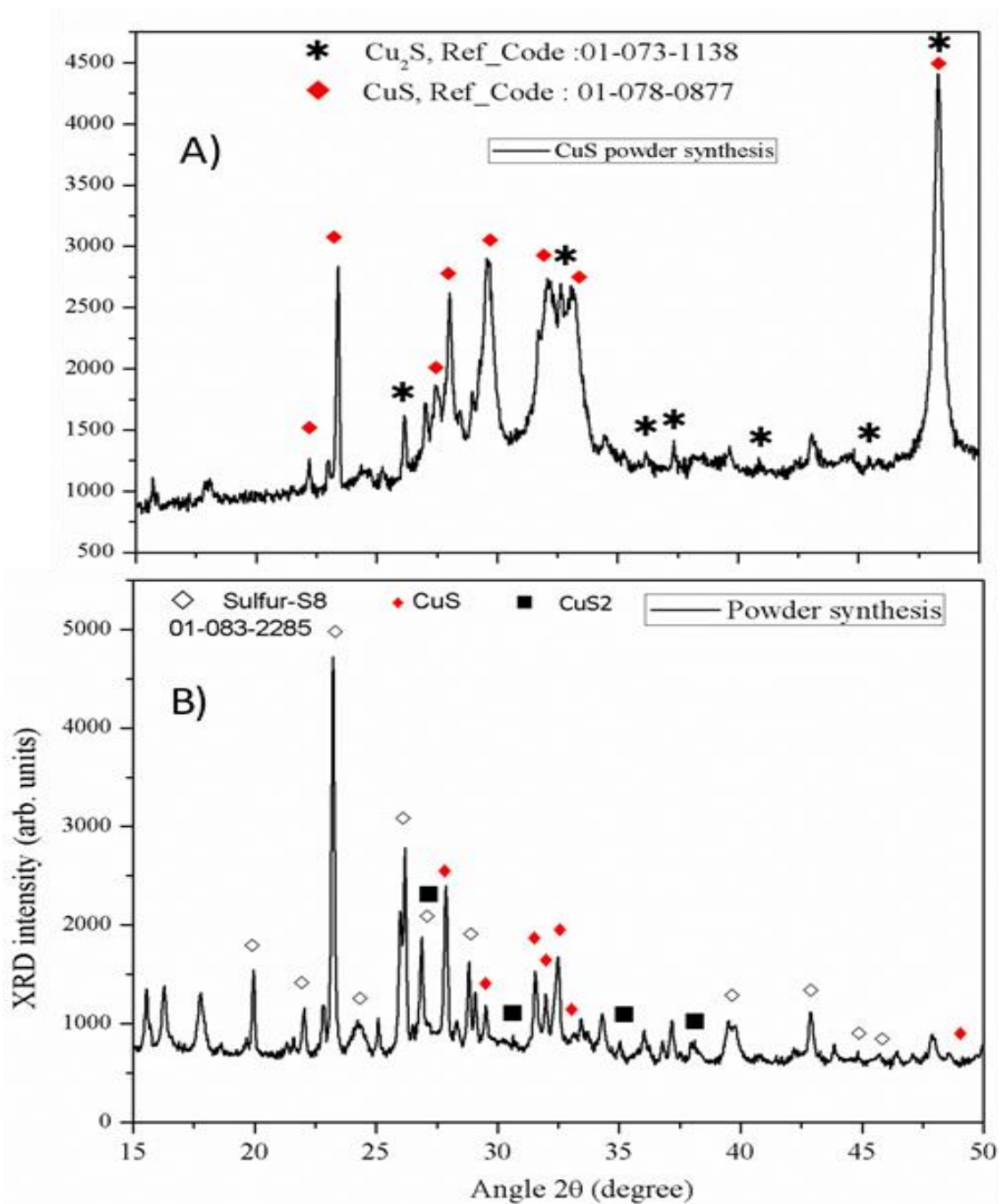
Figure3.1 XRD Pattern of A) CuS powder, B) CuS$_2$ powder.

The observed diffraction angles in our sample's diffractogramme are close to those reported in the literature [21, 40]. This confirms the presence of compounds with

the chemical formula Cu_xS, where (x=1, 2) each has a corresponding crystallographic phase. Chemical synthesis of this powder reveals the formation of clusters based on unsaturated Cu-S bonds, meaning that the degree of copper ionization is stopped at +1 following the $3d^9$ electronic configuration [29].

On the contrary, the X-ray diffractogramme pattern of CuS_2 shown in Figure 3.1 (B) exhibits diffraction peaks at $2\theta = 27.5°$, $31°$, $35°$, and $37°$. These peaks have been indexed and attributed to the presence of CuS_2, according to the reference code (01-083-1619) provided in the datasheet. Moreover, there are additional peaks indicating the presence of two other phases. The peaks corresponding to CuS are located at 2θ angles of approximately $27.5°$, $29°$, $32°$, $32.5°$, $34.5°$, and $49°$. These results are consistent with the hexagonal covellite copper sulfide (JCPDS card no. 01-078-0877) and are in good agreement with previous studies [100]. Additionally, the third phase observed is sulfur-S8,which constitutes the major phase, as determined by comparison with the JCPDS reference file (01-083-2285).

Let's turn to Figure 3.2, which shows the XRD pattern of a CuS_2 in the angle range $30° < 2\theta < 75°$. The thin film is heated to an annealing temperature of 500°C. Analyzing the obtained spectrum, we observe the presence of several well-defined peaks, indicating the crystalline nature of the sample. The most intense peak at $2\theta = 43°$ is attributed to the cubic phase of CuS_2. This phase belongs to the 3Pā space group, as determined by comparison with the JCPDS reference file (01-083-1619). However, relying solely on the indexing of a single peak is not sufficient to identify the corresponding phase. We therefore extended the indexing to other peaks in the diffraction pattern. Five further peaks were found to correspond to the cubic phase of CuS_2, in agreement with the aforementioned PDF file.

Furthermore, we observed the presence of secondary diffraction peaks in this sample. The main peaks of CuS_2 (JCPDS card no. 01-078-0877) were detected at approximate 2θ angles of $30.5°$, $45°$, $47°$, $65°$, and $70.5°$. Additionally, peaks located at $2\theta = 31°$, $36°$, $37°$, $39.5°$, and $61°$ correspond to Cu_2S. Furthermore, two peaks indicating CuS were observed at approximately 2θ angles of $37°$ and $74.5°$. Moreover, we noticed a peak at $2\theta = 50°$, which corresponds to diffraction on the (200) reticular planes. This peak is attributed to the cubic phase of copper wich is one of the phases present in our sample because of evaporative deposition.

In conclusion, the XRD of this analysis confirms the presence of four different phases in our sample.
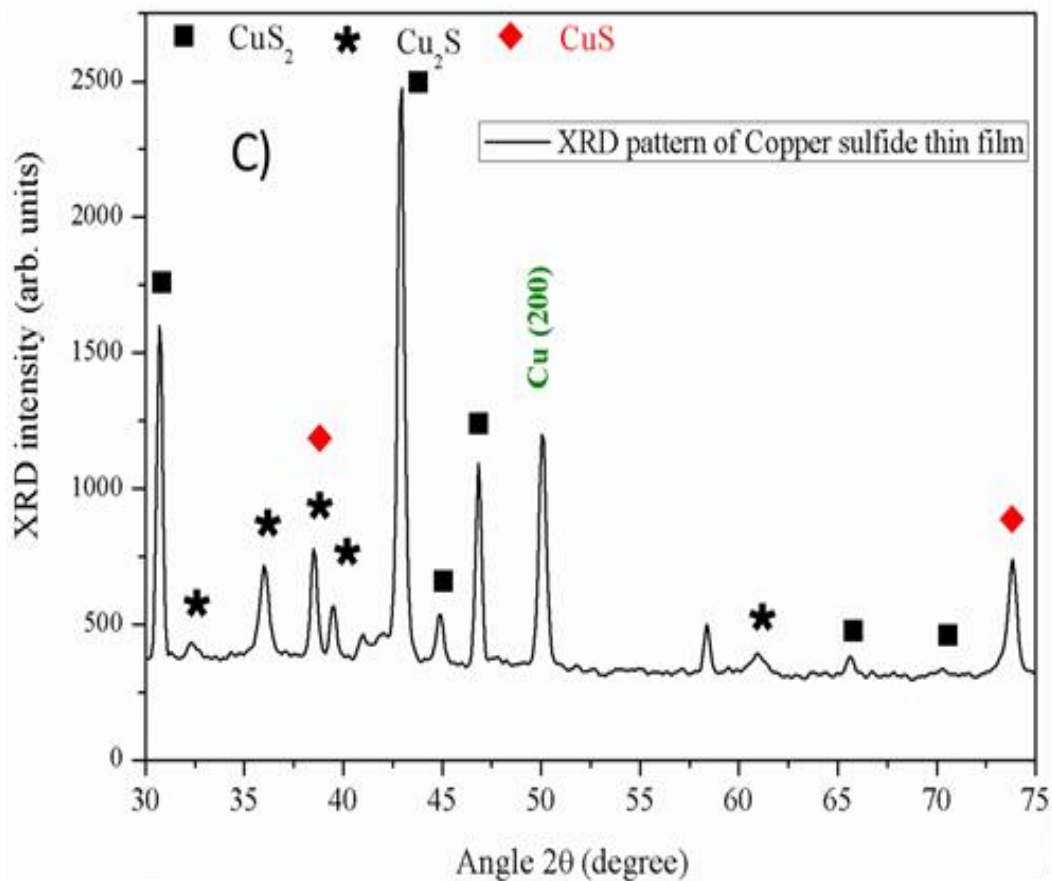
Figure3.2 XRD Pattern of C) Copper sulfide /500°C.

As an important note, we can say that the X-ray Diffraction (XRD) characterization of the chemically prepared sample did not provide conclusive results due to the very thin layer, which does not exhibit a distinct substrate profile on the silicon substrate. However, in the case of the evaporation method, where the layer thickness is significantly greater, XRD analysis becomes more relevant and enables obtaining more accurate structural information.

3.2. Scanning Electron Microscopy (SEM) Micrographs:

Scanning Electron Microscopy (SEM) is a powerful imaging technique that provides us detailed information about the topography, morphology, and elemental composition of samples.

Figure3.3 shows the SEM images of our CuS_2 layers for different annealing temperatures: 450°C, 500°C, and 550°C, respectively. Indicating that the annealing

temperature affects the morphology of the layers. Based on the SEM image obtained at a temperature of 450°C, the CuS_2 layer exhibits a homogeneous and regular shape. The particles appear to be uniformly distributed on the substrate, indicating a consistent nucleation and growth process. However, in terms of size, there is some irregularity observed. The particle sizes vary, with some particles appearing larger or smaller than others. This size variation may be attributed to different factors, such as variations in the deposition process or the presence of impurities.

At a temperature of 500°C, the SEM image of the CuS_2 layer reveals the presence of nanorods with a regular shape and size. The nanorods exhibit a square cross-sectional morphology, indicating a well-defined crystallographic orientation. The nanorods are not densely connected to each other, suggesting that they are not forming a continuous structure. This observation implies that the CuS_2 nanorods may have a cubic crystal structure, as opposed to individual nanocrystals. The formation of nanorods instead of isolated nanocrystals could be attributed to specific growth conditions or the preferential crystallographic orientation of the CuS_2 material at this temperature.

At 550°C, the SEM image of the CuS_2 layer shows that the nanoparticles have agglomerated, forming larger clusters. The individual nanoparticles appear to be smaller and more densely packed compared to the image obtained at 500°C. The increased temperature may have induced higher diffusion rates, leading to the agglomeration of the CuS_2 nanoparticles. This aggregation can result in a smaller average particle size and a more condensed arrangement. The observed changes in particle size and aggregation behavior at 550°C indicate the temperature-dependent evolution of the CuS_2 structure during the deposition process.

Based on the three images, it appears that the second image taken at 500°C shows the most desirable characteristics for the CuS_2 layer. The nanoparticles in this image exhibit a regular shape and size, and they are arranged in a well-connected manner. This indicates that the deposition process at 500°C resulted in the formation of CuS_2 nanoparticles with a more uniform and controlled morphology. Therefore, 500°C can be considered as the preferable temperature for the synthesis of CuS_2, as it yields nanoparticles with the desired properties for potential applications.
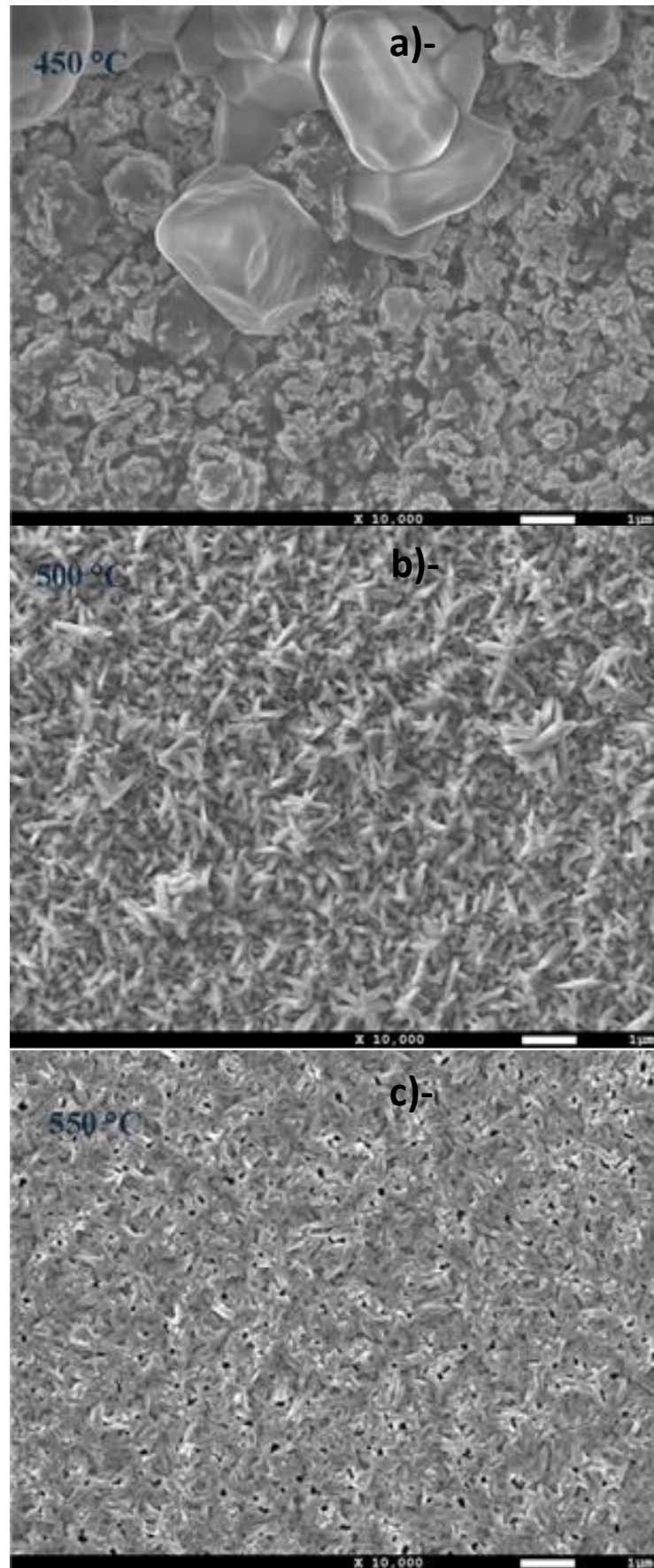
Fig. 3.3 SEM image of CuS$_2$ thin film at different deposition temperature (a) 450° (b) 500° (c) 550°.

In contrast, the as-prepared copper sulfide in the other study showed large grains and smaller particles with a spherical morphology at lower temperatures. However, at higher temperatures (500°C and 750°C), the morphology of the copper sulfide underwent drastic changes, with the formation of nanoparticles exhibiting higher anisotropy. Additionally, the grain size increased with temperature in the samples. Overall, the studies highlight the significant impact of temperature on the morphology and characteristics of copper sulfide nanoparticles [103].

3.3. Atomic force microscope (AFM) characterization

Atomic force microscopy (AFM) was utilized to analyze the surface morphology and roughness of the nanocrystals. The application of AFM techniques enabled the observation of microscopic features and the determination of topographical information regarding the surface relief of the nanocrystals [104].

Figure 3.4 shows the AFM images of four samples (pure Cu, Cu_xS_y at 450°C, Cu_xS_y at 500°C and Cu_xS_y at 550°C). The AFM images of the pure Cu sample show a surface with visible roughness and variations in morphology. The surface appears textured, with irregularities and variations in height observed. The roughness parameters, such as Ra and Rq, indicate the average roughness of the surface were found to be 101nm, 128nm respectively. Overall, the AFM images suggest that the pure Cu sample has a rough and textured surface with distinct irregularities.

For the Cu_xS_y sample at 450°C, the AFM image reveals a surface with lower levels of roughness compared to other sample. Minor variations in surface characteristics can be observed, along with the presence of large surface irregularities. The image depicts the typical height of surface features and provides insights into the spacing between these features.

The AFM analysis of the Cu_xS_y sample synthesized at 500°C reveals an increase in surface roughness, as indicated by the Ra and Rq values of 120 nm and 158 nm, respectively. This higher level of roughness is accompanied by noticeable variations in surface characteristics, as evidenced by the calculated surface area difference of 1.51%. The presence of significant surface irregularities further confirms the relatively rough surface texture observed in the AFM images. Additionally, the typical height of the surface features provides insights into the magnitude of surface

variations across the sample. The line density of 0.083/um suggests the spacing between surface structures, highlighting the overall surface morphology of the sample.
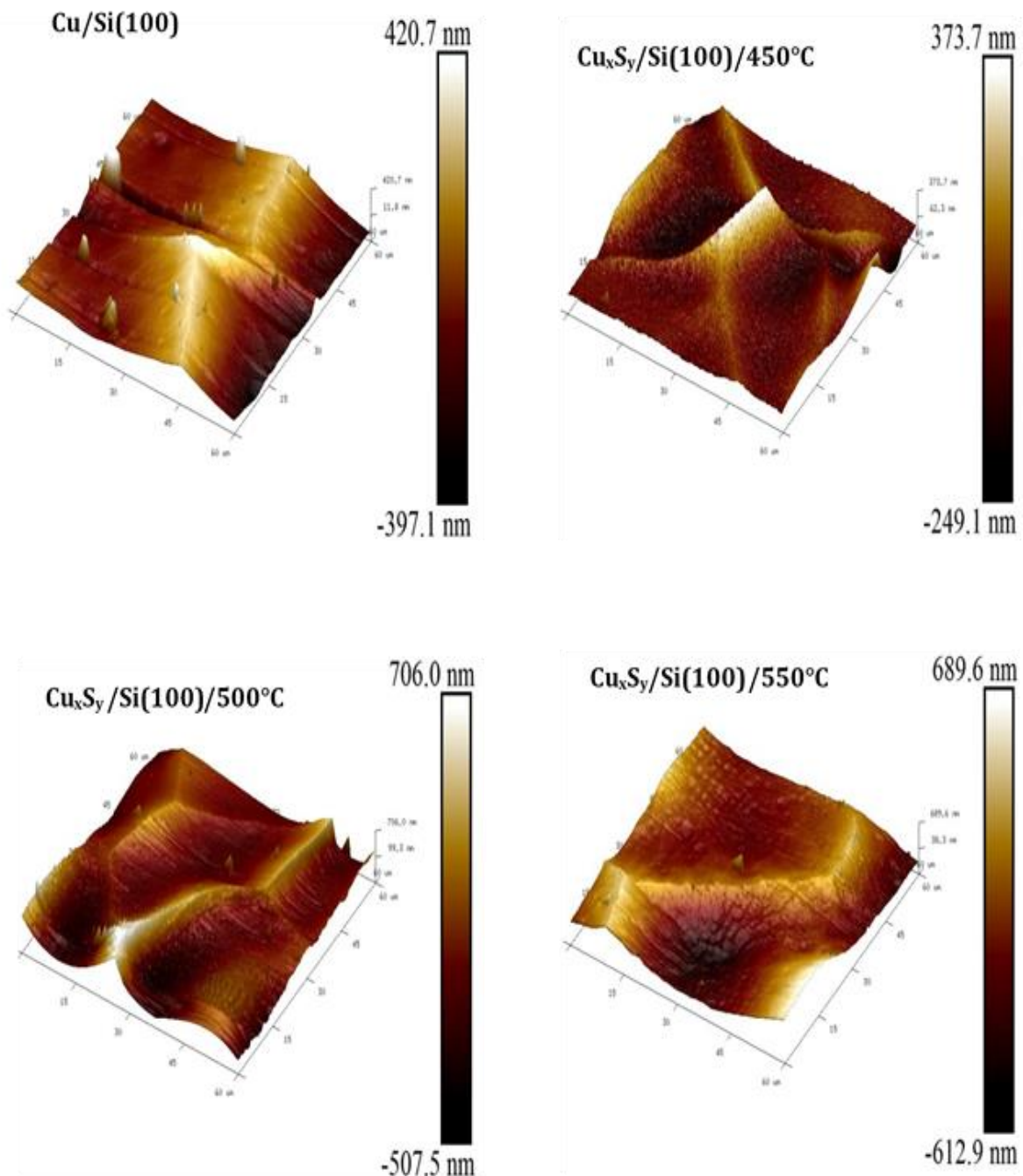
Fig.3.4 AFM image of samples.

Lastly, for the Cu_xS_y sample synthesized at 550°C, the AFM analysis reveals a relatively higher level of surface roughness. The room mean square roughness (Rq) and the average roughness (Ra) were found to be 141 nm and 180 nm, respectively,

indicating a significant roughness. The surface area difference is calculated to be 0.22%, suggesting minor variations in surface characteristics. The AFM images clearly depict the presence of larger surface irregularities, contributing to the overall roughness observed. Furthermore, the images provide insights into the typical height of the surface features, highlighting the magnitude of surface variations across the sample.

3.4. ATR-FTIR Spectrometer:

Figure 3.5 presents the ATR-FTIR spectra analysis results of three samples synthesized at different deposition temperatures (a) 450°C, (b) 500°C, and (c) 550°C. The FTIR measurements reveal distinct peaks corresponding to specific molecular vibrations in each sample.
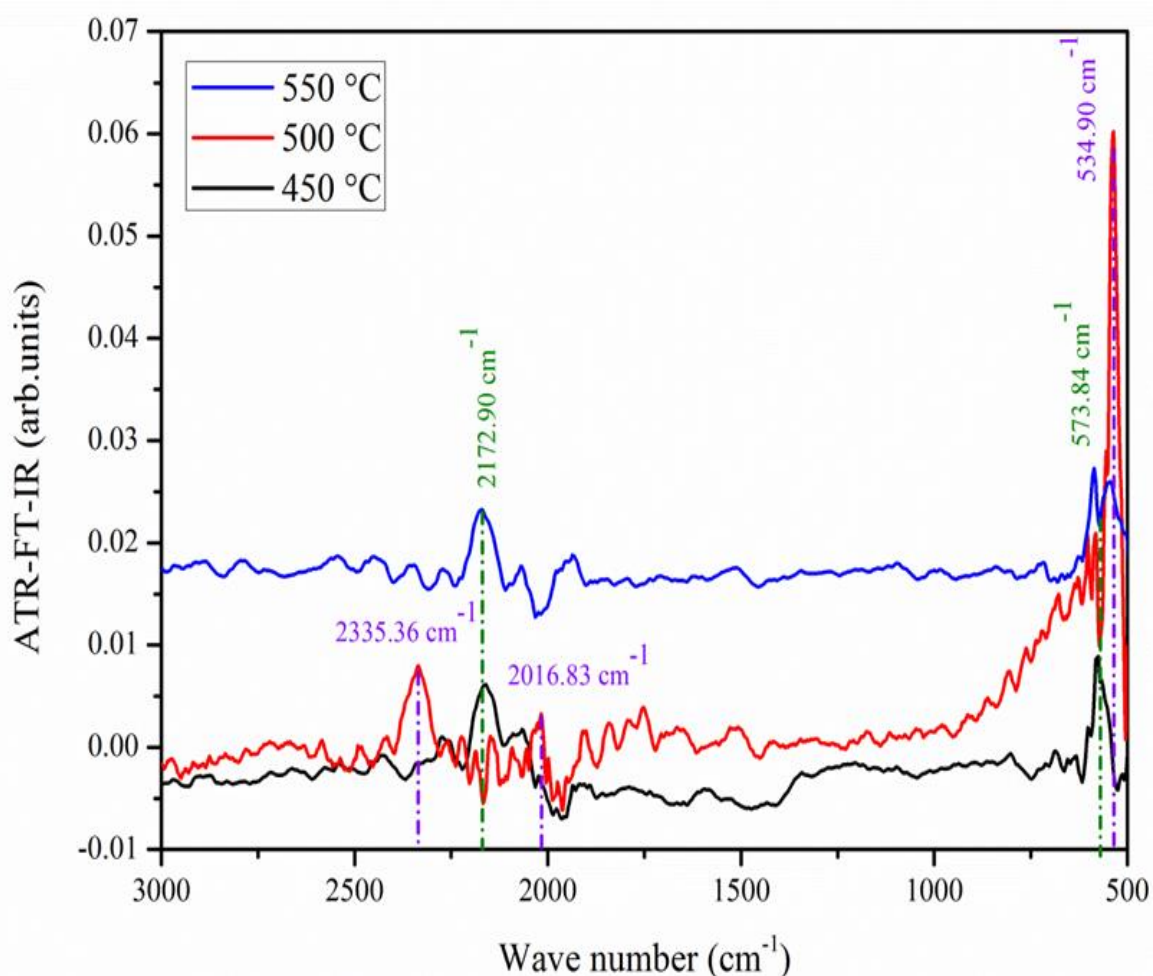
Fig. 3.5 ATR-FTIR spcetra of samples.

In the case of the sample N° 2, three distinct peaks were observed. The peak at 534.90 cm^{-1} corresponds to the symmetrical stretching vibration of Cu-S bonds [105]. On the other hand, we can mention another bond, which is the metal-sulfur bond that is present in the compound and is evident in the peak at 475 cm^{-1} due to the antisymmetric stretching of the S-Cu-S bonds [105]. The peak at 2016.83 cm^{-1} is attributed to the N=C=S vibrational mode, indicating the presence of isothiocyanate functional groups [106]. In addition, the peak at 2335.36 cm^{-1} represents the vibrational mode of O=C=O, suggesting the presence of carbon dioxide [107]. For samples deposited at 450°C and 550°C, two peaks were observed. The peak at 573.84 cm^{-1} is associated with a vibration mode involving the copper (Cu) center in the material [107]. The peak at 2172.90 cm^{-1} corresponds to the vibrational mode of S-C≡N, indicating the presence of thiocyanate groups [108]. These interpretations of the FTIR spectra highlight the characteristic vibrations and molecular signatures of Cu-S bonds, isothiocyanate groups, carbon dioxide and thiocyanate functional groups present in the respective samples at different deposition temperatures.
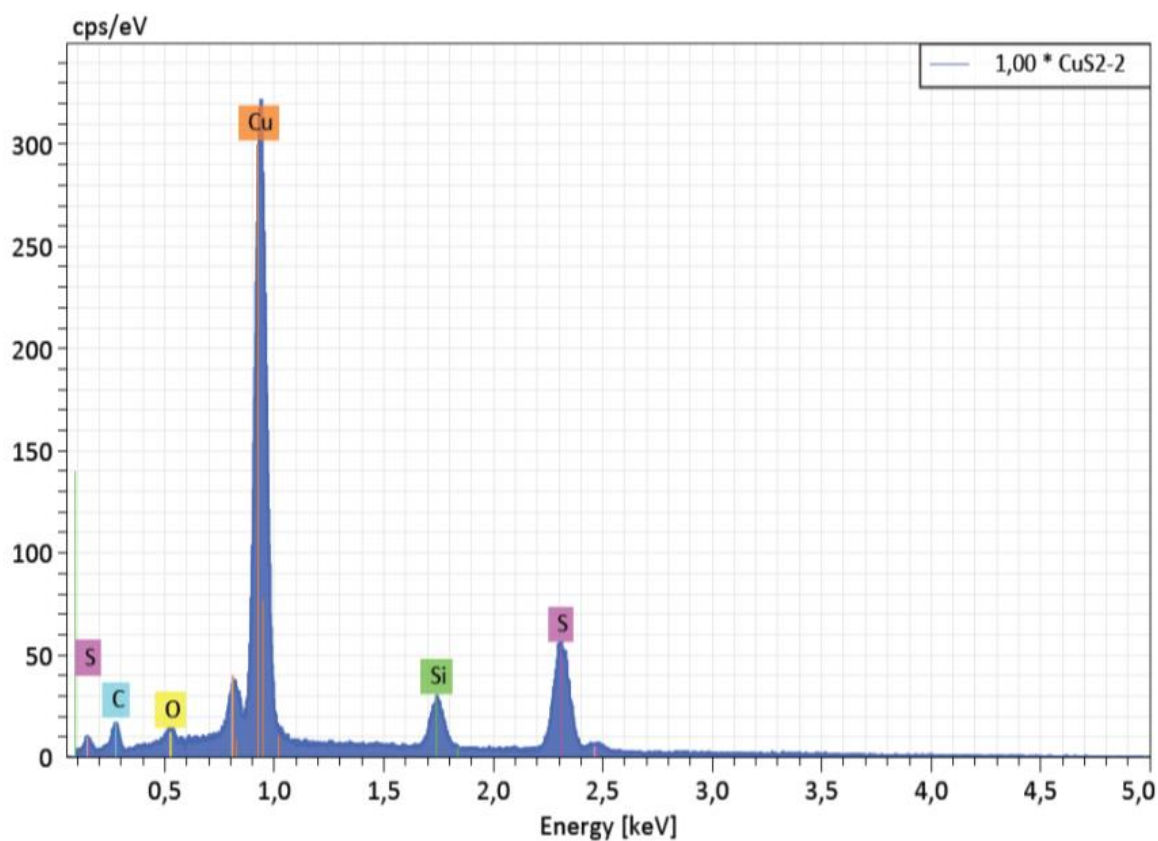
Fig. 3.6 EDXS Analysis Sample elaborated at 500 °C.

In order to conduct a more comprehensive verification of the composition and purity of the synthesized deposits, an EDS analysis was performed on the sample elaborated at 500°C.

The table below illustrates the atomic percentage proportions of Copper (Cu) and Sulfur (S), confirming the values of x and y in the Cu_xS_y formulation.

Table3.1The atomic ratio of Cu/S

CuS2-2

ÉlémentA	Raie	Net	Mass. [%]	Mass. norm. [%]	Atom. [%]	erreur abs. [%] (1 sigma)	erreur abs. [%] (2 sigma)	erreur abs. [%] (3 sigma)	erreur rel (1 sigma)
cuivre	29L-Serie	112299	83,48	70,28	50,88	9,37	18,74	28,11	11,22
soufre	16K-Serie	24634	22,87	19,25	27,62	1,15	2,31	3,46	5,05
silicium	14K-Serie	9790	9,79	8,24	13,50	0,50	1,00	1,50	5,12
carbone	6 K-Serie	2246	1,97	1,65	6,34	0,39	0,77	1,16	19,71
oxygène	8 K-Serie	1277	0,68	0,57	1,65	0,17	0,34	0,51	24,86
		Total :	118,79	100,00	100,00				

The EDX analysis of the Sample elaborated at 500 °C'is represented in Figure 3.6 and Table 3.1. The EDX spectrum of CuS_2 in Figure 3.6 shows the presence of copper (Cu) and sulfur (S), as well as other elements such as silicon (Si) from the substrate and nitrogen (N) and oxygen (O) corresponding to the reactants used in the CBD solution preparation. According to Table 3.1, the atomic percentages of Cu and S are approximately 50.88% and 27.62%, respectively.

In conclusion, the combined analysis of FTIR and EDX provided valuable insights into the composition and structural characteristics of the CuS_2 sample synthesized at 500°C. The FTIR analysis revealed specific vibrational modes and functional groups present in the sample, confirming the presence of Cu-S, S-Cu-S, N=C=S, and O=C=O bonds. EDX analysis confirmed the presence of copper (Cu) and sulfur (S) as the main elements, with atomic percentages compatible with the existence of CuS_2 stoichiometry. This indicates that the synthesized CuS_2 sample is chemically pure and has the expected composition. The complementary nature of

FTIR and EDX analyses enhances our understanding of the sample's chemical and structural properties, contributing to a comprehensive characterization of the CuS_2 material.

Optical properties

3.4.1. **Photoluminescence spectroscopy**

The observed photoluminescence (PL) spectrum of the three samples at different temperatures (550°C, 500°C, and 450°C), as shown in Figure 3.7, indicates the existence of two distinct peaks at 442 nm and 533 nm. These peaks indicate the recombination of electrons and holes within the material, resulting in the emission of light at specific wavelengths. PL peak is observed when electrons and holes recombine within a material. Electrons are negatively charged particles, while holes represent the absence of electrons in the valence band of the material. When an electron recombines with a hole, it releases energy in the form of light, resulting in a peak in the photoluminescence spectrum. The energy and intensity of the PL peak can provide insights into the recombination efficiency and properties of the material [109].

Notably, the PL peak at 500°C exhibits a higher intensity compared to the peaks observed at 550°C and 450°C. This suggests a more efficient recombination process and a higher rate of electron-hole recombination at 500°C. On the other hand, the lower intensity of the PL peak at 550°C indicates a relatively weaker recombination process at this temperature.

Overall, the PL spectrum provides valuable information about the optical properties and efficiency of electron-hole recombination in the studied samples. The observed differences in peak intensity at different temperatures offer insights into the variations in luminescent behavior and the impact of deposition temperature on the recombination processes within the material.
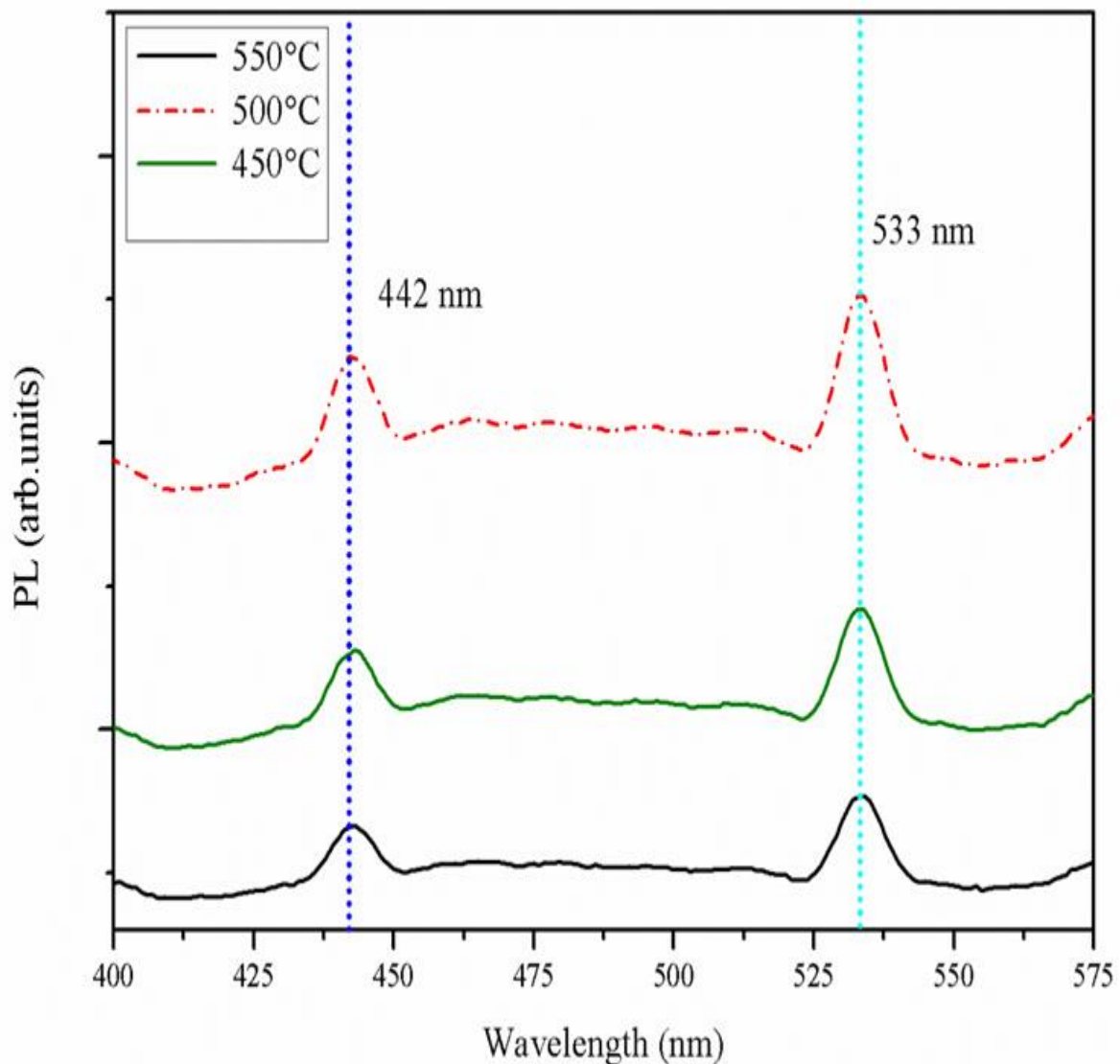
Fig. 3.7 Photoluminescence spectroscopy of samples.

3.4.2. <u>Gas analysis under area and under CO$_X$ environment :</u>

Gas treatment was employed in our study to investigate the response of CuS$_2$ under different concentrations of COx gas. The concentrations used were denoted as C1, C2, and C3, corresponding to flow rates of 50sccm, 100sccm, and 150sccm, respectively. The primary objective was to assess the sensitivity of the samples to specific gas concentrations. To determine the sensitivity, we calculated it using the formula:

$$S = \left| \frac{R_0 - R}{R_0} \right| \qquad\qquad (3.1)$$

$$R = \frac{V}{I} \qquad\qquad (3.2)$$

Where R_0 represents the initial resistance and R is the resistance calculated from the measured voltage (V) and current (I) values (Equation 3.2). By quantifying the sensitivity, we aimed to identify which sample displayed the highest sensitivity to the specified gas concentration. This approach allowed us to gain insights into the reactivity and responsiveness of the samples under different gas conditions.

The figure3.8 show The I(V) characteristic of the three samples, measured within the voltage range of [0-2V], reveals their electrical behavior under biased current conditions. The intensity of the current in all three samples increases with an increase in voltage, indicating a positive correlation between voltage and current. The I(V) curves for the samples exhibit a linear relationship, with a straight line connecting the data points. This suggests that the samples follow Ohm's law, where the current is directly proportional to the applied voltage. To calculate the resistance, a specific point on the line corresponding to a voltage of 1.6V was chosen. By reading the coordinates of this point, the current values for each sample were obtained: 0.0271 for sample 1, 0.0411 for sample 2, and 0.0157 for sample 3. These current values can be used to calculate the resistance using Ohm's law, Equation (3.2):

The resistance calculated for sample 1 R_1= 59.04 Ω, sample 2 R_2= 101.91 Ω and for the sample3 R_3=38.92Ω. The obtained resistance values provide information about the conductivity and electrical properties of the samples.

It can conclude that all three samples exhibit a linear electrical behavior and follow Ohm's law. The increase in current intensity with voltage indicates a positive correlation between the two variables. The calculated resistance values for each sample provide insights into their conductivity and electrical properties. The higher resistance values for sample 2 compared to sample 1 and sample 3, suggest that sample 2 has a lower conductivity. These findings contribute to our understanding of the electrical characteristics of the samples under biased current conditions.
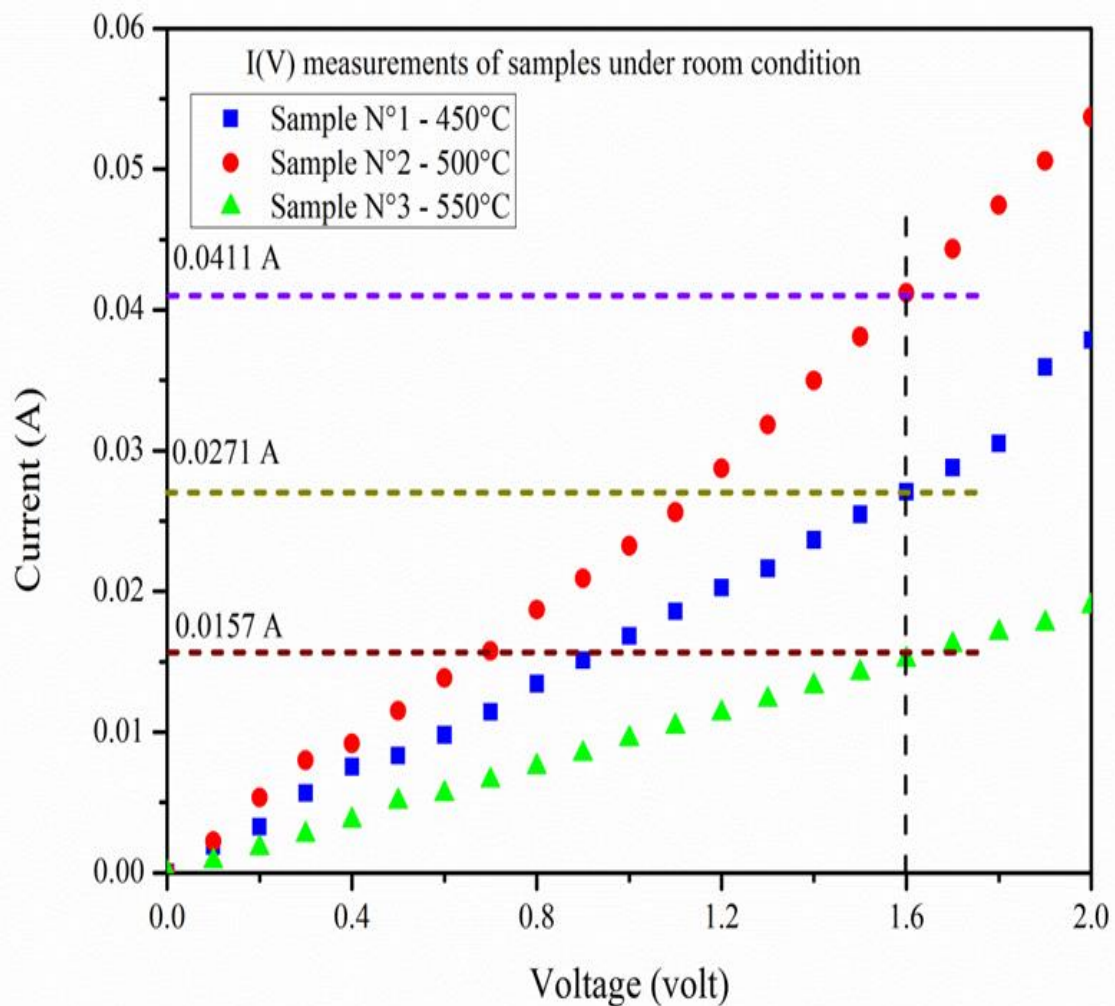
Fig. 3.8 I(V) samples under normal conditions and under COx gas.

a) **I(V) measure with CO_2**

The presented graphs illustrates in the figures 3.9,3.10 and 3.11 the relationship between current and voltage for the three samplesin the CO_2 environment within a voltage range of 0-2 volts. Notably, graphs exhibit a nearly linear trend, indicating a proportional relationship between voltage and current. As the voltage increases, the current also increases, reaching its maximum value for all three concentrations. This observation implies that changes in voltage directly influence the corresponding changes in current, suggesting a consistent and proportional behavior between these two variables.

I-V measurements offer valuable insights into the contact type and formation of particle-to-particle and electrode-particle interactions. To assess the CO_2 sensing capability of CuS_2 nanostructured films, samples annealed at 450 °C were subjected

to testing within a homemade gas chamber. The characteristic I-V curves of the sample were measured at room temperature in both air and CO_2 environments with a concentration range of [0-150] sccm, as shown in Figure 3.9. Notably, the figure depicts a consistent linear Ohmic behavior across all films. When transitioning from a CO_2 to an air environment, there was an observable increase in the current tracking rate at the same voltage. This effect can be attributed to the oxidizing nature of CO_2 gas, resulting in an increase in material resistance. Conversely, the gas composition of air led to a decrease in Ohmic resistance.
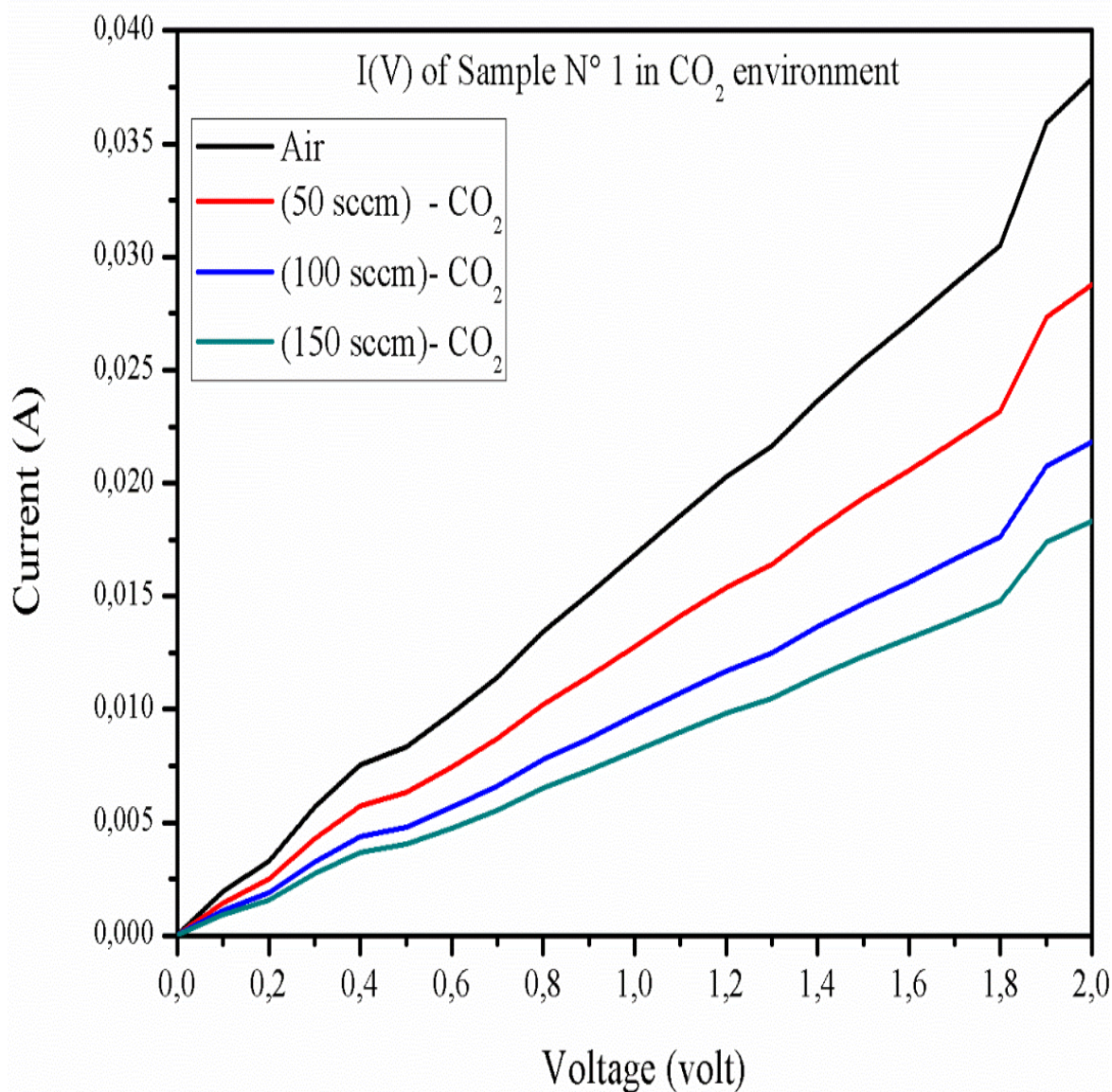
Fig. 3.9 I(V) of sample N∘1 in CO₂ environment.

While the table 3.2 presents the resistance values of the samples, indicating a consistent increase that demonstrates an Ohmic behavior.

Table 3.2 calculation of resistance and sensitivity for sample 1

V = 1.4 v			
I_0 (A)	I_1 (A)	I_2 (A)	I_3 (A)
0.024×10^{-3}	0.017×10^{-3}	0.013×10^{-3}	0.010×10^{-3}
R_0 (Ω)	R_1 (Ω)	R_2 (Ω)	R_3 (Ω)
58.33×10^3	82.4×10^3	107×10^3	140×10^3
S_0	S_1	S_2	S_3
0	0.15	0.7	0.75

The figure 3.10 represent the I(V) analysis of sample 2 under different concentrations of CO_2 gas reveals interesting trends. The concentrations used were labeled as C1, C2, and C3, corresponding to flow rates of 50sccm, 100sccm, and 150sccm, respectively. Notably, the curve obtained at 50sccm exhibits the highest current intensity within the voltage range of 0 to 2 volts. As the concentration increases to 100sccm, the curve shows a slightly lower current intensity compared to the first curve. Lastly, at 150sccm, the curve demonstrates the lowest current intensity among the three concentrations.

It is worth noting that the current values obtained for all three curves reached relatively large magnitudes, ranging from 0 to 0.06A. Additionally, the I(V) curves for all concentrations display a straight-line behavior, indicating a linear relationship between the applied voltage and resulting current. This linear behavior suggests a consistent and predictable response of sample 2 to the varying CO_2 gas concentrations within the specified voltage range.
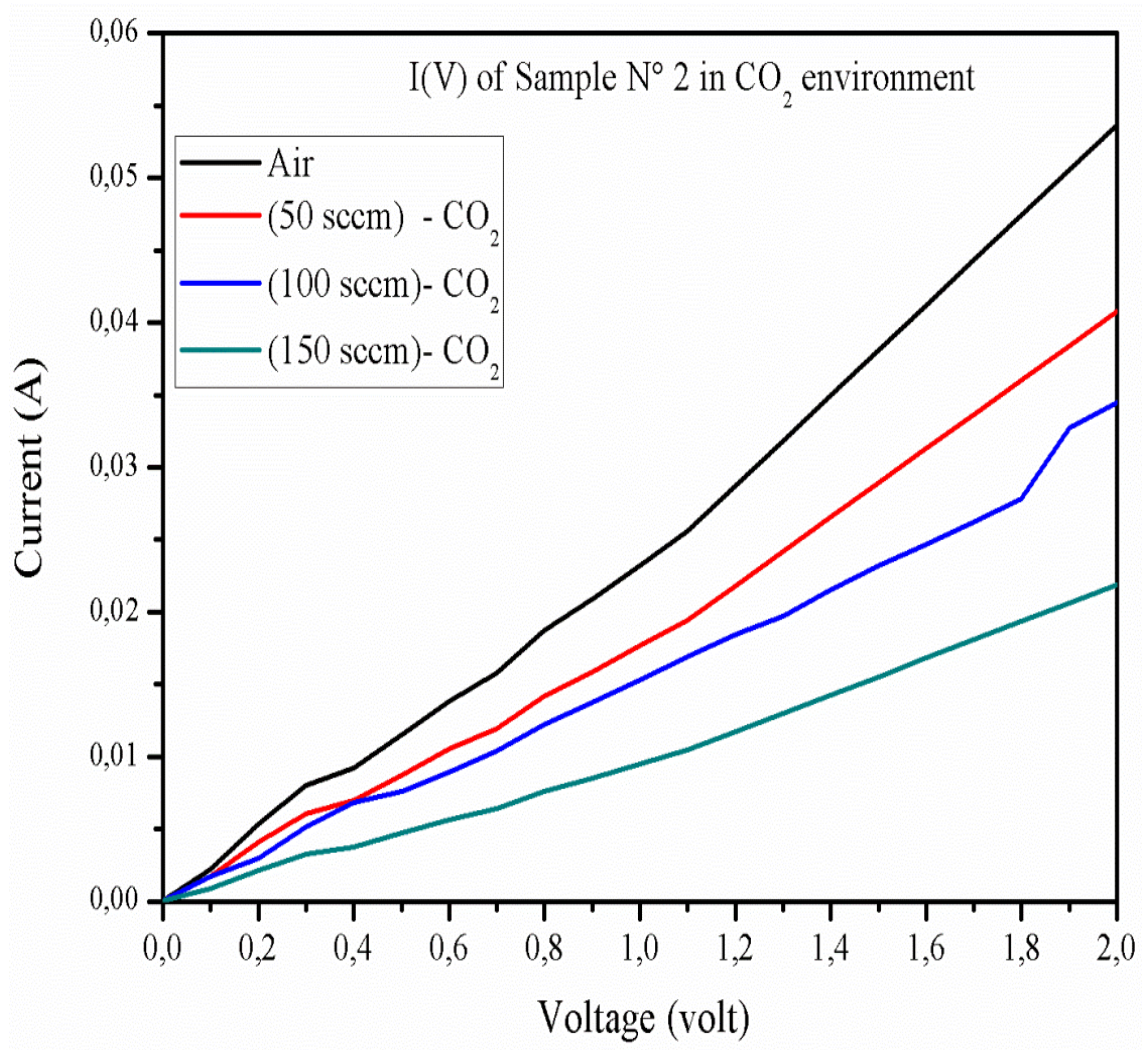
Fig. 3.10 I(V) of sample N°2 in CO_2 environment.

Table 3.3 calculation of resistance and sensitivity for sample 2.

V = 1.4 v			
I_0 (A)	I_1 (A)	I_2 (A)	I_3 (A)
0.036×10^{-3}	0.025×10^{-3}	0.02×10^{-3}	0.013×10^{-3}
R_0 (Ω)	R_1 (Ω)	R_2 (Ω)	R_3 (Ω)
39×10^3	56×10^3	70×10^3	107×10^3
S_0	S_1	S_2	S_3
0	0.43	0.79	1.74

66

In the final figure, which represents the I(V) characteristics of sample number 3 in a CO_2 environment, it is observed that the curves for 50sccm, 100sccm, and 150sccm concentrations are closely grouped together. This suggests that the response of sample 3 to different CO_2 concentrations within the specified range is similar.

Furthermore, the current values for all three curves range from 0 to 0.020A, indicating a relatively low current intensity. This suggests that sample 3 exhibits a consistent and limited current response across the different CO_2 concentrations. The close proximity of the curves and the relatively small current range indicate that sample 3 has a relatively low sensitivity to changes in CO_2 concentration within the tested range.
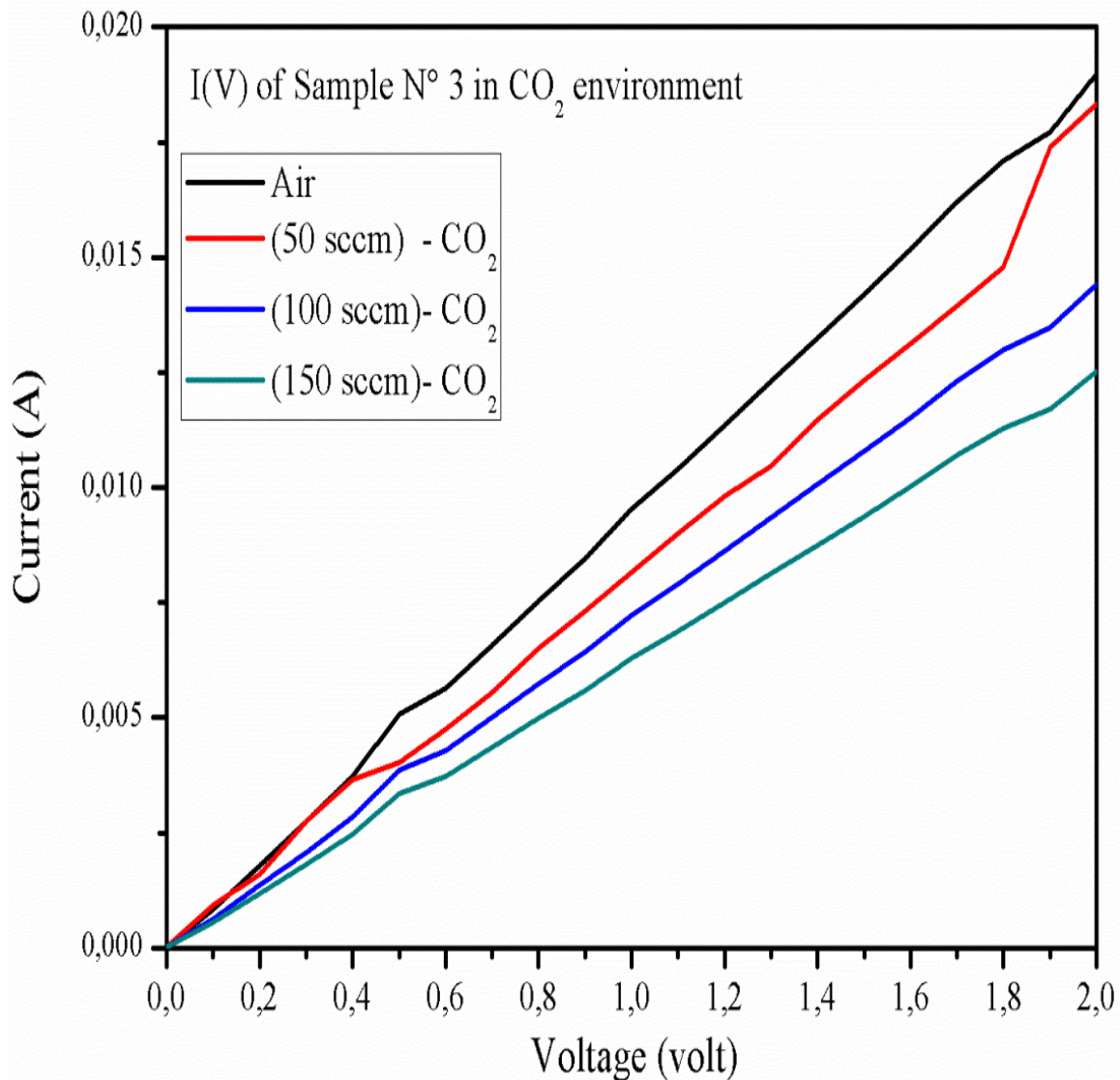
Fig. 3.11 I(V) of sample N°3 in CO_2 environment.

Table 3.4 calculation of resistance and sensitivity for sample 3.

V=1.4v			
I_0 (A)	I_1 (A)	I_2 (A)	I_3 (A)
0.014×10^{-3}	0.012×10^{-3}	0.010×10^{-3}	0.008×10^{-3}
R_0 (Ω)	R_1 (Ω)	R_2 (Ω)	R_3 (Ω)
100×10^3	116.7×10^3	140×10^3	175×10^3
S_0	S_1	S_2	S_3
0	0.167	0.4	0.75

3.4.3. Total reflectance measurement

In figure 3.12, the curve represents the total reflectance (Rf%) as a function of wavelength within the range of 350nm to 2450nm. The reflectance values (Rf%) span from 0% to 80%. The figure displays the reflectance characteristics of two samples, one annealed at 450°C and the other at 500°C.
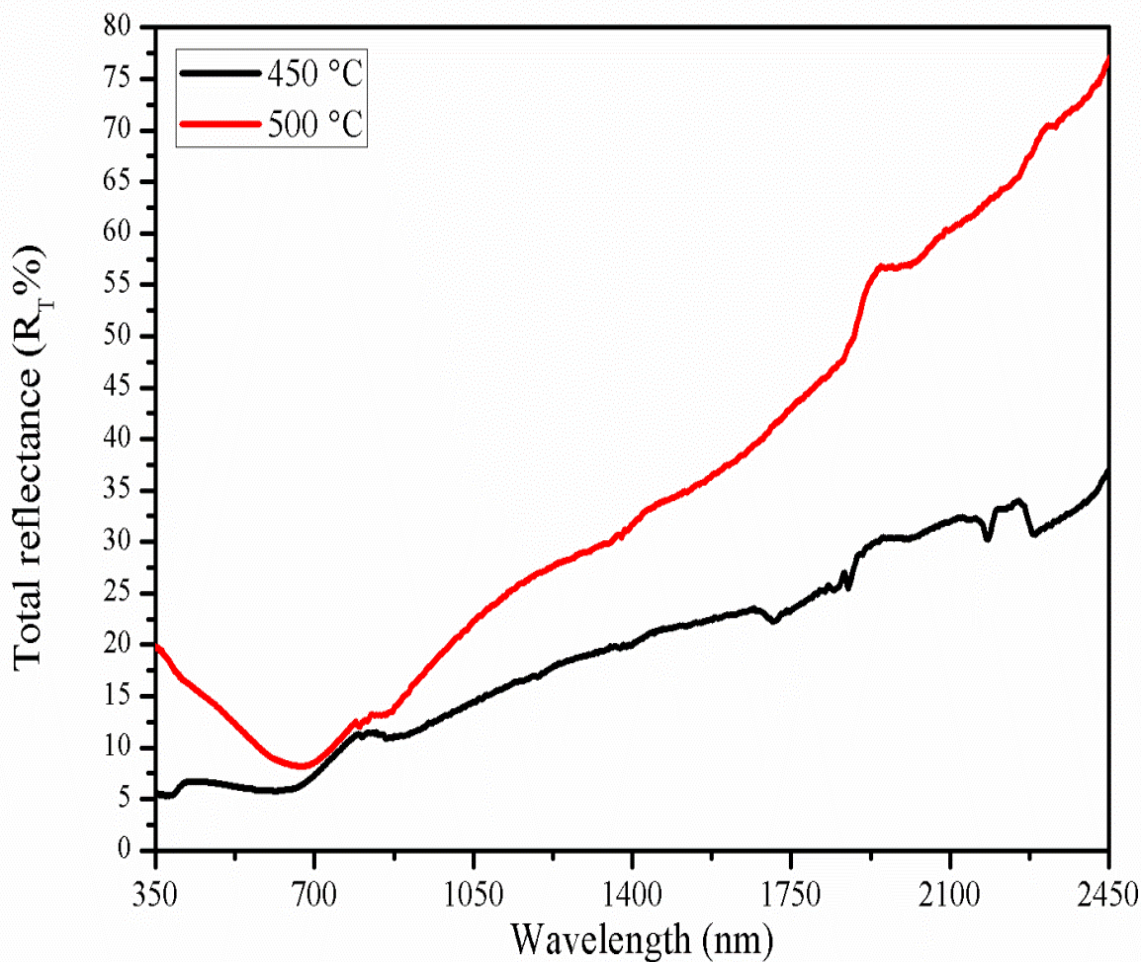
Fig. 3.12 Total reflectance measurement.

For the sample annealed at 450°C, the reflectance curve starts at 5% and gradually increases as the wavelength increases. This indicates that the material exhibits a relatively low reflectance at shorter wavelengths and becomes more reflective as the wavelength becomes longer.

In contrast, the reflectance curve for the sample annealed at 500°C starts at a higher value of 20%. As the wavelength increases, there is a noticeable decrease in reflectance, reaching a minimum of 10% at around 700nm. However, beyond 700nm, the reflectance increases rapidly, reaching a peak value of 77% at 2450nm.

3.4.4. <u>Diffuse reflectance measurement</u>

The diffuse reflectance figure who shown in figure 3.13 provides valuable information about the reflectivity of the samples in the UV-Vis range. In the plot, we observe a significant peak in the diffuse reflectance at approximately 600 nm for both samples. Sample 1 exhibits a higher peak with approximately 7.5% reflectance, while sample 2 shows a slightly lower peak with approximately 3.5% reflectance at the same wavelength. This peak can be attributed to the absorption threshold of the materials.

Additionally, the figure indicates that the diffuse reflectance gradually decreases with increasing wavelength. This behavior suggests that the samples have a higher tendency to absorb light at shorter wavelengths and scatter it in various directions, resulting in lower diffuse reflectance at longer wavelengths.

The observed behavior of decreasing diffuse reflectance with time until it becomes negligible could be attributed to various factors, including the formation of nanostructures within the samples. These nanostructures may affect the scattering and absorption properties of the materials, leading to changes in the diffuse reflectance characteristics. The absorbance never reaches zero, which is characteristic of the formation of copper sulfide [110].

Fig. 3.13 Diffuse reflectance measurement.

Conclusion

Our study focused on the development and characterization of copper disulfide (CuS_2) thin films prepared by the chemical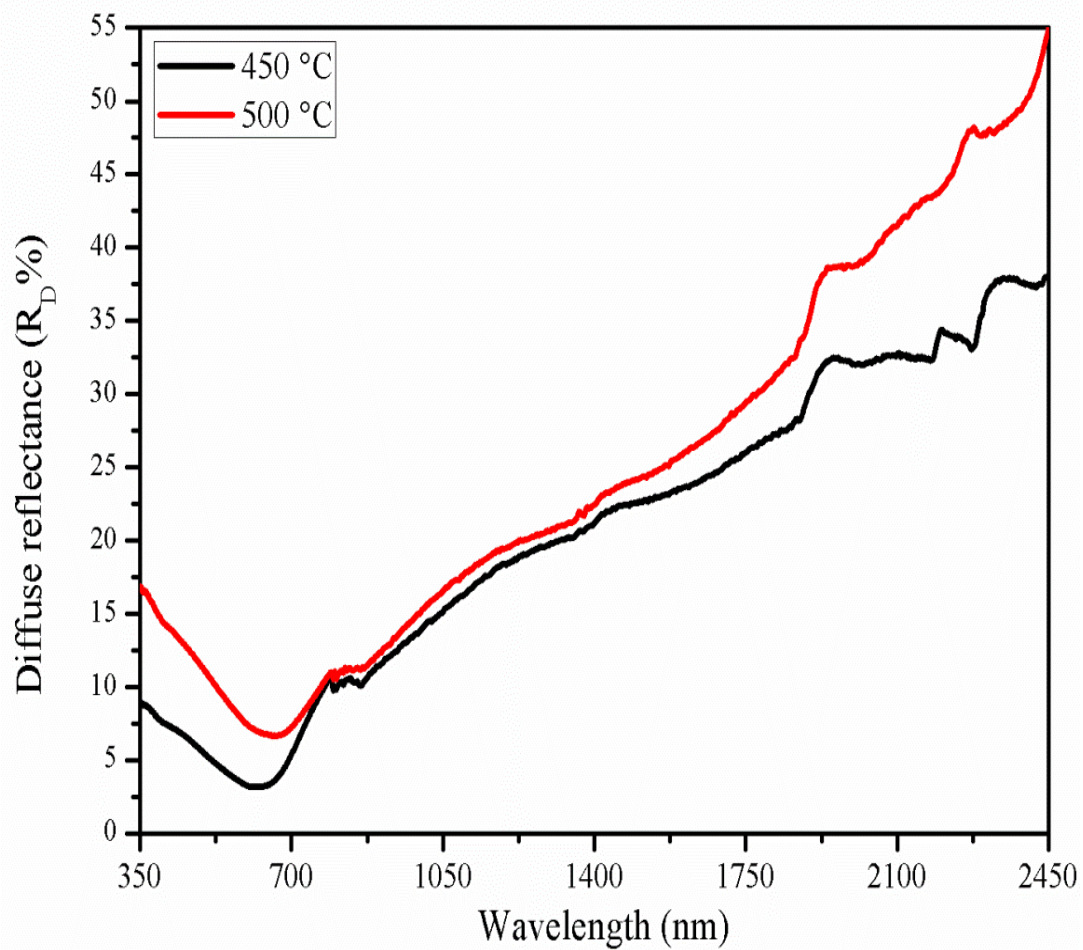 bath deposition (CBD) technique and the thermal evaporation method. Our characterization efforts employed a variety of analytical techniques to investigate the structural, morphological, compositional and optical properties of the synthesized CuS_2 samples.

XRD analysis revealed distinct crystallographic phases in the CuS and CuS_2 samples. The CuS powder showed clusters with unsaturated Cu-S bonds, indicating Cu ions in the +1 oxidation state. The CuS_2 thin film showed four different phases, with the cubic phase (space group $3P\bar{a}$) being the most prominent, as confirmed by comparison with the JCPDS reference file (01-083-1619).

With regard to morphology, SEM analysis revealed that the sample annealed at 500°C exhibited nanoparticles of regular shape and size, indicating well-controlled morphology and preferred characteristics for potential catalyst applications.

AFM analysis showed that the pure Cu sample presented a rough surface, while the Cu_xS_y samples presented smoother surfaces with reduced roughness, indicating the beneficial effect of sulfur incorporation on surface morphology. The combined analysis of FTIR and EDX techniques enabled us to better understand the composition and structure of CuS_2 synthesized at 500°C, confirming the presence of specific bonds and elements, including copper and sulfide, and validating its chemical and structural properties.

Photoluminescence studies of CuS_2 thin films showed a higher intensity of the PL peak at 500°C, indicating more efficient electron-hole recombination than at other temperatures as also for the gas treatment, which enabled that the sample 2 reacts better with CO_x gas.

Finally, our study exhibit a successful elaboration method giving better characterization results of copper disulfide (CuS_2) thin films using the CBD technique and the thermal evaporation method. The combination of various characterization techniques has enabled us to gain a comprehensive understanding of the structure, morphology, composition and structure of thin films.

References

[1] L.Rydén, P.Migula, M.Andersson ; ENVIRONMENTAL SCIENCE, http://uu.diva-portal.org/smash/get/diva2:608867/FULLTEXT01.pdf

[2] H. Ren, P. Koshy, W.-F. Chen, S. Qi, and C. C. Sorrell, Photocatalytic materials and technologies for air purification. J. Hazar. Mater. 325 (2017) 340–366, https://dx.doi.org/10.1016/j.jhazmat.2016.08.072.

[3] J. Deng, Z. Huang, B.J. Sundell, D.J. Harrigan, S.A Sharber, K. Zhang, M. Galizia. State of the art and prospects of chemically and thermally aggressive membrane gas separations: Insights from polymer science. Polymer, 229, (2021) 123988. http://dx.doi.org/10.1016/j.polymer.2021.123988

[4] ZJ. Shanan, MD. Majed, HM. Ali. Effect of the Concentration of Copper on the Properties of Copper Sulfide Nanostructure. Baghdad Sci.J [Internet]. 2022 Feb.1; 19(1):0225.   http://dx.doi.org/10.21123/bsj.2022.19.1.0225

[5] H.Ueda, M. Nohara, K. Kitazawa, H. Takagi, A. Fujimori, T. Mizokawa and T. Yagi. Copper pyrites CuS_2 and $CuSe_2$ as anion conductors. Physical Review B, (2002) 65(15). http://dx.doi.org/10.1103/physrevb.65.155104

[6] T.A. Bither, R.J. Bouchard, W.H. Cloud, P.C. Donohue and W.J. Siemons. Transition metal pyrite dichalcogenides. High-pressure synthesis and correlation of properties. Inorganic Chemistry, (1968) 7(11), 2208–2220. http://dx.doi.org/10.1021/ic50069a008

[7] G. Senanayake. A review of chloride assisted copper sulfide leaching by oxygenated sulfuric acid and mechanistic considerations. Hydrometallurgy, (2009) 98(1-2) 21–32. http://dx.doi.org/10.1016/j.hydromet.2009.02.010

[8] W.R. Schoeller and A.R.Powell. Villamaninite, a new mineral. Mineralogical Magazine and Journal of the Mineralogical Society, March 1920 v. 19; no. 88; p. 14-18; http://dx.doi.org/10.1180/minmag.1920.019.88.05

[9] H.E. KING, JR. eNo Cnenres T. PREWIT; Structure and symmetry of CuS_2, (pyrite structure)

[10] C.Liu, H.Yang, C-LSong, W. Li, K. He, X-C.Ma, X., Q.-K.Xue. Observation of Tunneling Gap in Epitaxial Ultrathin Films of Pyrite-Type Copper Disulfide. Chinese Physics Letters, 35(2), (2018) 027303. http://dx.doi.org/10.1088/0256-307x/35/2/027303

[11] João V. M. Limaa, Rafael A. Silvaa , Stevan B. O. Santosa , Carlos F. O. Graeffa,b,Luis V. A. Scalvi, Synthesis and Characterization of $Cu_{2-x}S$ structures by Different Chemical Routes for Electronic Applications, Materials Research. 2021; 24(suppl. 1): e20210018, https://doi.org/10.1590/1980-5373-MR-2021-0018./

[12] H. ter Maata, J.A. Hogendoornb, G.F. Versteeg, The removal of hydrogen sulfide from gas streams using an aqueous metal sulfate absorbent Part II. The regeneration of copper sulfide to copper oxide—an experimental study, Separation and Purification Technology 43 (2005) 199–213, http://dx.doi.org/10.1016/j.seppur.2004.10.012.

[13] Elliott, N. (1960) Interatomic distances in FeS_2, CoS_2 and NiS_2. "f.
Chem. Phys., JJ. 903-905.
[13_1] Finklea, S. L., III, Le Conte Cathey and E. L. Amma (1976) Investigation of the bonding mechanism in pyrite using the M6ssbauer effect and X-ray crystallography. Acta Crystallogr,, A32,529-537.

[14] Furuseth, S. and A. Kjekshus (1969) On the magnetic properties of $CoSe_2$, NiS_2, and $NiSe_2$. laa Chem. Scand., 23,2325-2334.Gibbons, G. S. (1967) Optical anisotropy in pyrite. Am. Mineral.,52,359-370.

[15] G. Brcistigen and A. Kjekshus, Bonding schemes for compounds with pyrite, marcasite and arsenopyrite type structures. Acta Chem. Scand., 24 (1970) 2993-3012.

[16] J.Goodenough. Energy bands in TX_2 compounds with pyrite, marcasite, and arsenopyrite structures. J. Solid State Chem., 5 (1972) IM-152.

[17] Kjekshus, A. and D. G. Nicholson, The significance of back-bonding in compounds with pyrite, marcasite, and arse- Thorn nopyrite type structures. Acta Chem. Scand., 25 (1971) 866–876.

[18] H.r.barai, p. Barai, M. roy and S.W. Joo, nano-structural design of 0d, 1d, 2d, 3d nanoparticles for energy storage devices: supercapacitor applications, renewable energy and resources energy materials and fuel cell research 2nd international conference on & august 27-28, 2018, http://dx.doi.org/10.4172/2576-1463-c2-005.

[19] A.I.Gusev. Nanomaterials, Nanostructures, and Nanotechnologies (in Russian) // Fizmatlit, Moscow (2007) - 416 pp

[20] A.I.Gusev, A.A.Rempel. Nanocrystalline Materials. Cambridge: Cambridge International Science Publishing, 2004 — 351 p.

[21] N.L.Botha and P.A.Ajibade. Optical and structural characterization of copper sulphide nanoparticles from copper (II) piperidine dithiocarbamate. Optical and Quantum Electronics, (2020) 52(7). https://doi.org/10.1007/s11082-020-02455-w

[22] Villamaninite (Cu,Ni,Co,Fe)S$_2$; MineralDataPublishing,version1;2001-2005 https://rruff.info/doclib/hom/villamaninite.pdf

[23] N. Berry, m. Cheng, c.l. Perkins, m. Limpinsel, j. C. Hemminger, and m. Law, atmospheric-pressure chemical vapor deposition of iron pyrite thin films, adv. Energy mater. 2012, https://doi.org/10.1002/aenm.201200043.

[24] Copper Sulfid, eassignment point; (2023). https://assignmentpoint.com/copper-sulfide/

[25] J. Black, E. Conwell, L. Seigle, C. Spencer, J. Phys. Chem.Sol. (1957) 2, 240.

[26] K. Nose, Y. Soma, T. Omata and S.Otsuka-Yao-Matsuo. Synthesis of Ternary CuInS2Nanocrystals; Phase Determination by Complex Ligand Species. Chemistry of Materials, 21(13) (2009) 2607–2613. https://doi.org/10.1021/cm802022p

[27] V.S. Sathyakumari, S. Sankar and K. Mahalakshmi Electronic and thermal properties of metallic CuS$_2$ Compound with pyrite structure: An ab-initio study. May-June 2014 ;Vol.6, No.3, pp 1736-1738, https://sphinxsai.com/2014/vol6pt3/6/(1736-1738)ICMCT14.pdf

[28] The Materials explorer (CuS$_2$); The Materials Project, (2023) https://materialsproject.org/materials/mp-1068

[29] J.C.W. Folmer, F. Jellinek and G.H.M. Calis. The electronic structure of pyrites, particularly CuS$_2$ and Fe$_{1-x}$Cu$_x$Se$_2$: An XPS and Mössbauer study. Journal of Solid State Chemistry, 72(1), (1988) 137–144. https://doi.org/10.1016/0022-4596(88)90017-5

[30] N. Ouarab. Electronic and optical performance of Ni-doped FeS$_2$ nanocrystals for photovoltaic applications. Physica E: Low-Dimensional Systems and Nanostructures, (2020). 115, 113688. https://doi.org/10.1016/j.physe.2019.113688

[31] G. Krill, P. Panissod, M.F. Lapierre, F. Gautier, C. Robert and M. Nassr Eddine;Magnetic properties and phase transitions of the metallic CuX$_2$

dichalcogenides (X=S, Se, Te) with pyrite structure; Journal of Physics C: Solid State Physics, Volume 9, Number 8 http://iopscience.iop.org/0022-3719/9/8/023

[32] M.Kontani, T. Tutui, T. Moriwaka, T. Mizukoshi. Specific heat and NMR studies on the pyrite-type superconductors CuS_2 and $CuSe_2$. Physica B: Condensed Matter, 284-288, (2000) 675–676.

https://doi.org/10.1016/s0921-4526(99)02353-4

[33] D. F. Pridmore; r. T. Shuey, the electrical resistivity of galena, pyrite, and chalcopyrite, american mineralogist (1976) 61 (3-4): 248–259.

Https://doi.org/10.1016/j.minpro.2003.09.002.

[34] A. Dasadia , V. Bhavsar: Growth, structure, electrical and optical properties of transition metal chalcogenide crystals synthesized by improved chemical vapor transport technique for semiconductor technologies. Volume 68, Issue 3, August 2022, 100578   https://doi.org/10.1016/j.pcrysgrow.2022.100578

[35] M. Cota-Leala,b, D. Cabrera-Germana,b, M. Sotelo-Lermaa, M. Martínez-Gila,b ,J.A. García-Valenzuela. Highly-transparent and conductive CuI films obtained by a redirected low-cost and electroless two-step route: Chemical solution deposition of CuS_2 and subsequent iodination. Materials Science in Semiconductor   Processing,   95   (2019)   59–67.
https://doi.org/10.1016/j.mssp.2019.02.016

[36] N.Bouguila , Y. Bchiri, M. Kraini, R. Souissi, N. Hafienne,C.Va´zquez-Va´zquez3, and S. Alaya;Investigation of some physical and photoconductive properties of sprayed CuS_2 filmN. March 2022Journal of Materials Science: Materials in Electronics 33 (2007):1-12 https://doi.org/10.1007/s10854-021-07572-0

[37] M. Hossein, S. Pourang, A. Mobina; Electrochemical properties of pyrite, pyrrhotite, and steel: effects on grinding and flotation processes. (2012) 883-890

[38] J.B. Mooney, S.B. Radding, Spray pyrolysis processing, annual review of materials science (1982) vol. 12:81-101,

 https://doi.org/10.1146/annurev.ms.12.080182.000501.

[39] Yin, Q., Kelsall, G.H., Vaughan, D.J., England, K.E.R., 1995. Atmospheric and electrochemical oxidation of the surface of chalcopyrite ($CuFeS_2$). Geochimica et Cosmochimica Acta 59, 1091–1100.

[40] Y.He,X. Zhang, S.Wang, J. Meng, Y. Sui, F. Wei, FD. Zhuang. (2020). Rubik's cube-like Ni_3S_4/CuS_2 nanocomposite for high-performance supercapacitors. Journal of Alloys and Compounds, 156312. doi:10.1016/j.jallcom.2020.156312

[41] S.M.Marcus, & T.A.Bither. (1970). Measurement of the de Haas-van Alphen effect in the pyrite-type copper dichalcogenides CuS_2, $CuSe_2$ and $CuTe_2$. Physics Letters A, 32(5), 363–364. doi:10.1016/0375-9601(70)90549-9

[42] M. Hasseine and Y. Ouldkhaoua, Synthese et caracterisation des couches minces de sulfure de cuivre Cu_xS_y : Etude des proprietes photoelectrochimique master's thesis, A. Alger1 University, (2021).

[43] M.Mittal, S.Sardar , A.Jana; Chapter 7 - Nanofabrication techniques for semiconductor chemical sensors; Micro and Nano Technologies; Elsevier 2021, Pages 119-137 https://doi.org/10.1016/B978-0-12-820783-3.00023-3

[44] G.Niu, G.Saint-Girons,& B.Vilquin. Epitaxial systems combining oxides and semiconductors. Molecular Beam Epitaxy, (2013) 451–475. https://doi.org/10.1016/b978-0-12-387839-7.00018-x

[45] A.Edwin Thin Films/Properties and Applications; October/2021 License; CC BY 3.0. 10.5772/intechopen.95527

[46] S.M. Jogade, P.S. Joshi, B.N. Jamadar, D.S. Sutrave; MOCVD of Cobalt Oxide Using Co-Actylacetonate As Precursor: Thin Film Deposition and Study of Physical Properties; (2011) No1, P.203-21

[47] P. Arkashis, S. Baidurya, P. Swastik , Sk. Abdul Moyez, H-S. Jung, R. Subhasis ;From 3.8% to over 23.8% Power Conversion Efficiency: Commercial Perovskite Solar Cells, Significant Manufacturing Techniques, and Future Prospects ; Volume 1, (2023) Pages 418-433 https://doi.org/10.1016/B978-0-12-819728-8.00044-9

[48] Low Pressure Chemical Vapor Deposition Systems; MKS Instruments Handbook: Semiconductor Devices & Process Technology, (2023). https://www.mks.com/n/lpcvd-systems

[49] Atmospheric Pressure Chemical Deposition; SCRIBD, Uploaded by iloveCG ,Jan-29-2013. https://www.scribd.com/document/122786480/Atmospheric-Pressure-Chemical-Deposition

[50] M. Bahri, S.H. Gebre,M. A. Elaguech, F.T. Dajan, M.G. Sendeku, C. Tlili, D. Wang; Recent advances in chemical vapour deposition techniques for

graphene-based nanoarchitectures: From synthesis to contemporary applications; Volume 475, 15 January 2023, 214910 https://doi.org/10.1016/j.ccr.2022.214910

[51] Thin film deposition techniques; by Alicat Scientific https://www.alicat.com/thin-film-deposition-techniques/

[52] V. TEIXEIRA, J. CARNEIRO, P. CARVALHO, E. Silva, S. Azevedo and C. Batista , High barrier plastics using nanoscale inorganic films. Multifunctional and Nanoreinforced Polymers for Food Packaging, (2011); 285–315. https://doi.org/10.1533/9780857092786.1.285

[53] J. Orava, T. Kohoutek, and T. Wagner. Deposition techniques for chalcogenide thin films. Chalcogenide Glasses, (2014). 265–309. https://doi.org/10.1533/9780857093561.1.265

[54] A.Sarangan. Nanofabrication. Fundamentals and Applications of Nanophotonics, (2016) 149–184. https://doi.org/10.1016/b978-1-78242-464-2.00005-1

[55] Z. Liu, Laser Applied Coatings. Shreir's Corrosion, (2016) 2622–2635. https://doi.org/10.1016/b978-044452787-5.00141-4

[56] S-I. Park, Y-J. Quan, S-H. Kim, H. Kim, S. Kim, D-M. Chun, S-H. Ahn. A review on fabrication processes for electrochromic devices. International Journal of Precision Engineering and Manufacturing-Green Technology, 3(4) (2016) 397–421. https://doi.org/10.1007/s40684-016-0049-8

[57] G.Faraji, H.S.Kim, & H.T.Kashi. Introduction. Severe Plastic Deformation, (2018).1–17. https://doi.org/10.1016/b978-0-12-813518-1.00020-5

[58] D. Depla, S. Mahieu, and J.E. Greene. Sputter Deposition Processes. Handbook of Deposition Technologies for Films and Coatings, (2010). 253–296. https://doi.org/10.1016/b978-0-8155-2031-3.00005-3

[59] T. Dhandayuthapani, M. Girish, R. Sivakumar, C. Sanjeeviraja and R. Gopalakrishnan, tuning the morphology of metastable mns films by simple chemical bath deposition technique, applied surface science volume 353, 30 october 2015, pages 449-458, https://doi.org/10.1016/j.apsusc.2015.06.154.

[60] Semiconductor and ceramic nanoparticle films deposited by chemical bath deposition https://doi.org/10.1039/B616684A

[61] I. RAHAMMIA and I. BAHI, Synthèse et caractérisation des films minces de sulfure de cuivre (Cu_xS) déposées par bain chimique, Master's thesis from Oum EL Bouaghi University

[62] A.A. Ensafi, Z. Saberi. N. Kazemifard;13 Functionalized nanomaterial-based medical sensors for point-of-care applications: An overview.(2022) Pages 277-308 https://doi.org/10.1016/B978-0-12-823788-5.00018-1

[63] M. Asyadi, M. Mupit; Chapter 2 Carbon nanomaterial-based sensor: Synthesis and characterization;2022, Pages 15-28 https://doi.org/10.1016/B978-0-323-91174-0.00015-9

[64] G.C. Chern and I. Lauks.'Spin-coated amorphous chalcogenide films', J. Appl.Phys. (1982) 53, 6979–6982.

[65] B.S.Yilbas, A. Al-Sharafi and H.Ali. Surfaces for Self-Cleaning. Self-Cleaning of Surfaces and Water Droplet Mobility, (2019) 45–98. https://doi.org/10.1016/b978-0-12-814776-4.00003-3

[66] M. Joshi and B.S. Butola. Application technologies for coating, lamination and finishing of technical textiles. Advances in the Dyeing and Finishing of Technical Textiles, (2013) 355–411. https://doi.org/10.1533/9780857097613.2.355

[67] D. Lončarević, and Z. Čupić. The perspective of using nanocatalysts in the environmental requirements and energy needs of industry. Industrial Applications of Nanomaterials, (2019) 91–122. https://doi.org/10.1016/b978-0-12-815749-7.00004-9

[68] L.A. Neacşu, A.I. Nicoară, O.R. Vasile, B.S. Vasile, chapter 9 - inorganic micro- and nanostructured implants for tissue engineering, nanobiomaterials in hard tissue engineering applications of nanobiomaterials volume 4 2016, pages 271-295, https://doi.org/10.1016/b978-0-323-42862-0.00009-2

[69] D.S. Jung, Y.N. Ko, Y.C. Kang, and S.B. Park. Recent progress in electrode materials produced by spray pyrolysis for next-generation lithium ion batteries. Advanced Powder Technology, (2014). 25(1), 18–31. https://doi.org/10.1016/j.apt.2014.01.012

[70] M.B. Tahir, M. Rafique, M.S. Rafique, T. Nawaz, M. Rizwan, and M. Tanveer. Photocatalytic nanomaterials for degradation of organic pollutants and heavy metals. Nanotechnology and Photocatalysis for Environmental Applications,(2020). 119–138. https://doi.org/10.1016/b978-0-12-821192-2.00008-5

[71] P.K. Kannan, S. Chaudhari, S.R. Dey, M. Ramadan ; Progress in Development of CZTS for Solar Photovoltaics Applications; Volume2 (2022) Pages681-698 https://doi.org/10.1016/B978-0-12-815732-9.00130-3

[72] Pr. Abdelhakim MAHJOUB, cours de techniques d'élaboration de couches minces, www.univ-oeb.dz

[73] S.E. bnesajjad. Surface and Material Characterization Techniques. Handbook of Adhesives and Surface Preparation, (2011). 31–48. https://doi.org/10.1016/b978-1-4377-4461-3.10004-5

[74] P.S.Liu and G.F.Chen.Characterization Methods. Porous Materials, (2014) 411–492. https://doi.org/10.1016/b978-0-12-407788-1.00009-5

[75] S. Sinha Ray. Structure and Morphology Characterization Techniques. Clay-Containing Polymer Nanocomposites, (2013) 39–66. https://doi.org/10.1016/b978-0-444-59437-2.00003-x

[76] S-H. Jung, D. Park, J.H. Park, Y-M. Kim and K-S.Ha. Molecular imaging of membrane proteins and microfilaments using atomic force microscopy. Experimental and Molecular Medicine, 42(9) (2010) 597. https://doi.org/10.3858/emm.2010.42.9.064

[77] T. Raghavendra, S.G. Bhat ;Chapter 2 - Enzyme immobilized nanomaterials (2022) Pages 17-65 https://doi.org/10.1016/B978-0-12-824436-4.00007-1
[77_1]AFM, AFMWorkshop; (2021). https://www.afmworkshop.com/site-map/articles/products/ls-afm/ls-afm-stage.

[78] M.Tubiana;Wilhelm Conrad Röntgen and the discovery of X-rays;1996 Jan;180(1):97-108. https://pubmed.ncbi.nlm.nih.gov/8696882/

[79] F. Sima, C. Ristoscu, L. Duta, O. Gallet, K. Anselme and I.N. Mihailescu. Laser thin films deposition and characterization for biomedical applications. Laser Surface Modification of Biomaterials, (2016) 77–125. https://doi.org/10.1016/b978-0-08-100883-6.00003-4

[80] M. Dudley, and X.R. Huang. X-ray Topography. Encyclopedia of Materials: Science and Technology, (2001). 9813–9825. https://doi.org/10.1016/b0-08-043152-6/01780-0
[80_1] Analyses minéralogiques DRX - poudres / argiles ; Institut Terre & Environnement de Strasbourg – ITES, (2021). https://ites.unistra.fr/services-plateformes/diffractometre-rx.

[81] Diffraction Basics -Chemical Instrumentation Facility; Iowa State University. (1995) 50011-3111. https://www.cif.iastate.edu/services/acide/xrd-tutorial/xrd

[82] A.A. Bunaciu, E.G. Udriştioiu, and H.Y. Aboul-Enein. X-Ray Diffraction: Instrumentation and Applications. Critical Reviews in Analytical Chemistry, 45(4) (2015) 289–299. https://doi.org/10.1080/10408347.2014.949616

[83] K.D.Bartle, &P. Myers. History of gas chromatography. TrAC Trends in Analytical Chemistry, 21(9-10) (2002) 547–557. https://doi.org/10.1016/s0165-9936(02)00806-3

[84] L.M. Blumberg. Theory of gas chromatography. Gas Chromatography, (2021). 19–97. https://doi.org/10.1016/b978-0-12-820675-1.00026-5

[85] E. Stauffer, J.A. Dolan, R.Newman, chapter 8 - gas chromatography and gas chromatography—mass spectrometry, fire debris analysis 2008, https://doi.org/10.1016/b978-012663971-1.50012-9

[86] Gas chromatography: principles and application, http://epgp.inflibnet.ac.in/epgpdata/uploads/epgp_content/S001174BS/P001204/M031003/ET/1526972909P9M15_ET.pdf

[87] J. Goldstein, D.E. Newbury, P.Echlin, C.E. Lyman, D.C. Joy, E.Lifshin, L.C. Sawyer, J.R. Michael, Scanning Electron Microscopy and X-ray Microanalysis : Third Edition, Springer Verlag, (1992) 689.https://doi.org/10.1007/978-1-4615-0215-9.

[88] T. Meghana, R.P. Oorvashi. S. M. Oros, and A. Singh. Drosophila adult eye model to teach Scanning Electron Microscopy in an undergraduate cell biology laboratory. Population Data Information Service, (2009) 92:174-180.

[88_1] A.C. Malti, S. Dembélé, N.L. Fort-Piat, P. Rougeot, & R. Salut. Magnification-continuous static calibration model of a scanning-electron microscope. Journal of Electronic Imaging, (2012) 21(3):3020- https://doi.org/10.1117/1.JEI.21.3.033020

[89] N. John and S. George. Raman Spectroscopy. Spectroscopic Methods for Nanomaterials Characterization, (2017) 95–127. https://doi.org/10.1016/b978-0-323-46140-5.00005-4

[90] I.R. M.Ramos, A. Malkin and F.M. Lyng. Current Advances in the Application of Raman Spectroscopy for Molecular Diagnosis of Cervical Cancer. BioMed Research International, (2015) 1–9. https://doi.org/10.1155/2015/561242

[90_1] Raman Spectroscopy; Eurofins SFA SN Special Analysis West, (2021). http://snlabs.com/raman-spectroscopy/.

[91] Dr. Deepak; Evolution of FT-IR Spectroscopy (May-16-2015). https://lab-training.com/evolution-of-ft-ir-spectroscopy/.

[92] A. Nandiyanto, R. Okitiani and R. Ragadhita, how to read and interpret ftir spectroscope of organic materia, urnal of science & technology,volume 4 issue March 2019 http://dx.doi.org/10.17509/ijost.v4i1.15806

[93] B. Patrizi, Siciliani de Cumis, Viciani, & F.D'Amato. Dioxin and Related Compound Detection: Perspectives for Optical Monitoring. International Journal of Molecular Sciences, (2019). 20(11), 2671. https://doi.org/10.3390/ijms20112671

[94] K.dyamenahalli, A.famili, R.shandas, 3 - characterization of shape-memory polymers for biomedical applications, shape memory polymers for biomedical applications woodhead publishing series in biomaterials 2015, pages 35-63, https://doi.org/10.1016/b978-0-85709-698-2.00003-9.

[95] J. Adrie, J. Bos, thermoluminescence as a research tool to investigate luminescence mechanisms, materials (2017), 10, 1357, https://doi.org/10.3390/ma10121357.

[96] J. A. Nieto, thermoluminescence dosimetry (tld) and its application in medical physics, aip conference proceedings (2004) 724, 20; https://doi.org/10.1063/1.1811814.

[97] Chapter3-10 : Thermoluminescence, phys178, Page2. (2009) 09-47 http://www.le.infn.it/~chiodini/allow_listing/archeometria/chap3_10.pdf

[98] P.J. Potts. X-RAY FLUORESCENCE AND EMISSION | X-Ray Fluorescence Theory. Encyclopedia of Analytical Science, (2005) 408–418. doi:10.1016/b0-12-369397-7/00673-7

[98_1] X-Ray Fluorescence (XRF); Geochemical Instrumentation and Analysis, January 21, 2020. https://serc.carleton.edu/18398

[99] T. Peter, Y. Ezgi, and C. Halil; «Concrete Pavement Mixtures Design and Analysis: The Application of Portable X-Ray Fluorescence Technique to Assess Concrete Mix Proportions». March (2012) 09-353.

[100] D.S. Koutsonikolas, G.T. Pantoleontos, and S.P. Kaldis, Ceramic Membranes, Preparation, Properties, and Investigation on CO_2 Separation. Current Trends

and Future Developments on (Bio-) Membranes, (2018). 185–207. https://doi.org/10.1016/b978-0-12-813645-4.00006-4

[101] D.L. Chandler. A better way to separate gases; MIT News Office, March 24, 2022. https://news.mit.edu/2022/membrane-separate-gases-0325

[102] S.M.H. Al-Jawad,Ali A. Taha and M. M.muhsen; Preparation and Characterization of CuS Nanoparticles Prepared byTwo-Phase Colloidal Method 2021 J. Phys.: Conf. Ser. 1795 012053. https://doi.org/10.1088/1742-6596/1795/1/012053

[103] I. Sobia , A.S.Naveed , M.S.Muhammad ,J. Yasir , M.Arslan ,A. Gulzar, A.Faisal , S.Muhammad ; Extensive evaluation of changes in structural, chemical and thermal properties of copper sulfide nanoparticles at different calcination temperature. Journal of Crystal Growth (2020) https://doi.org/10.1016/j.jcrysgro.2020.125823

[104] P. A.Ajibade, & N.M.Botha, N. L. Synthesis and structural studies of copper sulfide nanocrystals. Results in Physics, (2016) 6, 581–589. https://doi.org/10.1016/j.rinp.2016.08.001

[105] B. Xu , K. Wu , Z. Chen. Tribology properties of CuS nanoparticals In-situ synthesized in liquid paraffin. Guangzhou Chem. Ind. 38: (2010) 147-149.

[106] S. Ariponnammal, S. Chandrasekaran, and C. Sanjeeviraja. Low temperature photoluminescence studies on semiorganic tris thiourea copper (I) chloride single crystal. Crystal Research and Technology, 47(2) (2011) 145–150. https://doi.org/10.1002/crat.201100451

[107] Infrared Spectroscopy Absorption Table, https://chem.libretexts.org/Ancillary_Materials/Reference/Reference_Tables/Spectroscopic_Reference_Tables/Infrared_Spectroscopy_Absorption_Table .

[108] I. Savarimuthu and M.J. Arokia, CuS Nanoparticles Trigger Sulfite for Fast Degradation of Organic Dyes under Dark Conditions. 7, (2022) 4140−4149. https://doi.org/10.1021/acsomega.1c05697

[109] L.T. Hoang Yen, V. Thuan, N.T Hanh, N. H. T. Vy, T. T. M. Hang, H. Van Ha, N.T.T Truc. Synthesis of N and S Co-doped TiO_2 Nanotubes for Advanced Photocatalytic Degradation of Volatile Organic Compounds (VOCs) in Gas Phase. Topics in Catalysis.63, (2020) 1077–1085. https://doi.org/10.1007/s11244-020-01347-3

[110] A.Dasari, G.Veerabhadram; Preparation, Characterization, Photocatalytic, Sensing and Antimicrobial Studies of Calotropis gigantea Leaf Extract Capped CuS NPs by a Green Approach Springer November 2017Journal of Inorganic and Organometallic Polymers and Materials 27(1) https://doi.org/10.1007/s10904-017-0672-z